Department of Physics and Astronomy
Heidelberg University

Master thesis in Physics
submitted by

Pascal Becht

2021

born in Neuenbürg (Germany)

Performance and characterisation of bent monolithic active pixel sensors (MAPS) for the application in future tracking detectors using the example of the ALPIDE chip

This master thesis has been carried out by Pascal Becht at
GSI Helmholtzzentrum für Schwerionenforschung GmbH, Darmstadt (Germany) and
Physikalisches Institut Ruprecht-Karls-Universität Heidelberg, Heidelberg (Germany)
under the supervision of
Prof. Dr. Silvia Masciocchi

Abstract

During the second long shutdown period 2019–2021 (LS2) of CERN's Large Hadron Collider (LHC), the Inner Tracking System (ITS) of the ALICE experiment will be replaced by a new vertex detector featuring 7 concentric layers of silicon pixel detector, the ITS2. For this upgrade project a new monolithic active pixel sensor (MAPS) based on $180\,\mathrm{nm}$ CMOS technology has been developed and thoroughly tested in several testbeam campaigns. The ALICE Pixel Detector (ALPIDE) chip provides a position resolution of about $5\,\mu\mathrm{m}$ and a sensor efficiency above $99\,\%$. Using state of the art ALPIDE chips as a basis, the research and development phase for the future upgrade of the ITS2 has started. Within the ITS3 project the three innermost layers of the ITS2 will be replaced by truly cylindrical, wafer-scale CMOS MAPS. First feasibility studies of bent MAPS are performed by bending standard ALPIDE chips to a target radius of up to $18\,\mathrm{mm}$. After ensuring its electrical functionality, the first ever in-beam characterisation of a laterally bent silicon pixel sensor has been performed at DESY in June 2020. Moreover, a longitudinally bent ALPIDE chip was also tested in a separate testbeam campaign in August 2020.
This thesis presents the testbeam campaigns featuring bent MAPS along with the required data analysis strategy for these cases, especially the implementation of curved pixelated sensor geometries in the testbeam data analysis framework Corryvreckan. The performance of bent ALPIDE chips, including efficiency, cluster size and preliminary position resolution, is discussed and compared to the one for flat sensors. Comparable detector performances are found, thus paving the way for further research and ultimately the application of bent MAPS in future particle and nuclear physics experiments.

Zusammenfassung

Während der Long Shutdown Phase 2019–2021 (LS2) des Large Hadron Colliders (LHC) am CERN, wird das alte Inner Tracking System (ITS) des ALICE Experiments durch ein neues ersetzt, das ITS2. Dieses besteht aus Silizium Pixel Detektoren, die in 7 konzentrischen Schichten angeordnet sind. Für das ITS2 Projekt wurde deshalb ein neuer Sensor basierend auf $180\,\mathrm{nm}$ CMOS Technologie als monolithisch aktiver Pixel Sensor (MAPS) entwickelt und in Teststrahl Experimenten getestet. Hierbei wies der ALICE Pixel Detektor (ALPIDE) Chip eine Ortsauflösung von circa $5\,\mu\mathrm{m}$ und eine Detektionseffizienz von über $99\,\%$ auf.
Für eine weitere Verbesserung des ITS2 startete bereits die Forschungs- und Entwicklungsphase auf Basis des aktuellen ALPIDE Chips. Die drei innersten Detektorschichten des ITS2 werden für den ITS3 durch wirklich zylindrische, großflächige CMOS MAPS ersetzt. Erste Machbarkeitsstudien bezüglich gebogener MAPS wurden durch das Biegen von normalen ALPIDE Chips auf Radien von bis zu $18\,\mathrm{mm}$ durchgeführt. Die erste Charakterisierung eines lateral gebogenen Silizium Pixel Sensors in einem Teilchenstrahl fand im Juni 2020 am DESY statt. In einem Folgeexperiment im August 2020 wurde zudem ein längs gebogener ALPIDE Sensor getestet.
In dieser Arbeit sind beide Teststrahlexperimente mit gebogenen MAPS sowie die dadurch notwendige Datenanalyse dargestellt. Insbesondere wird dabei auf die Realisierung einer gebogenen Sensorgeometrie im Teststrahl-Datenanalyse Programm Corryvreckan eingegangen. Die Leistungsfähigkeit der gebogenen ALPIDE Chips wird in den Punkten Detektionseffizienz, Clustergröße und einer Vorstufe zur Ortsauflösung mit flachen Sensoren verglichen. Es wurden hierbei vergleichbare Werte festgestellt. Somit eröffnet sich die Möglichkeit weiterer Forschung bis hin zur Anwendung von gebogenen MAPS in zukünftigen Teilchen- und Kernphysikexperimenten.

Contents

1 Monolithic Active Pixel Sensors

In high-energy particle and nuclear physics experiments all different kinds of detectors are used in order to take data, which is then analysed to reveal the nature of the underlying physical processes in the observed particle-particle interactions. For this purpose, usually hadrons or leptons are accelerated in a particle accelerator and brought to collision with either a target or another particle beam. The most prominent and largest example of such a particle accelerator is the Large Hadron Collider (LHC) located at the European Council for Nuclear Research (CERN) in Geneva, Switzerland. It usually collides protons, but also offers the possibility to deliver heavier nuclei collisions such as lead-lead.

At sufficiently high collision energies, a multitude of different particles are produced in the collision and emerge from the interaction point. As they follow their trajectories they can be registered by particle detectors, which are usually placed around the interaction point in a layered geometry[1]. In order to identify the particles their mass needs to be determined. This is often done by measuring the *momentum* and the *energy* of the particle[2], which then allows to calculate its mass. For the momentum measurement charged particles are deflected by a magnetic field due to the Lorentz force acting on them. The momentum of the particle can then be extracted from the curvature of the trajectory. Hence, this kind of measurement essentially boils down to measuring the trajectory of the charged particle, i.e. a position measurement.

Detectors used to perform position measurements are ideally placed as close as possible to the interaction point in order to also detect short-lived and low-momenta particles[3]. These kind of detectors are called *tracking* or *vertexing* detectors. Due to their vicinity to the collision point, they have to withstand especially large particle fluxes, which could possibly damage the detectors. The degradation of the detector performance due to the impact of particle radiation is referred to as *radiation damage*.

In these harsh conditions the experimental program further introduces very demanding requirements for the tracking detectors in terms of granularity, rate capability, material thickness, readout speed and power consumption. To meet all these requirements as good as possible, a large number of experiments implement silicon pixel detectors in their inner layers. For example all of the four main experiments at the LHC, i.e. ATLAS, CMS, LHCb and ALICE feature (pixelated) silicon tracking layers in their core[4] [1]. For ALICE and its future follow-up experiment this can be seen in figure 2.2 and 2.5.

The development of silicon pixel detectors underwent a revolution during the 1980s by making use of complementary metal oxide semiconductor (CMOS) technology in the readout electronics accompanying the sensors [2]. As further described in section 1.5 and 3.2, this technology allows for compact and efficient integrated circuits (IC) for analog signal processing and logical operations.

[1] For specific examples of particle detectors see section 2.2 and 2.3

[2] Also velocity measurements, like time-of-flight or Cherenkov angle, can be used in combination with others to determine the particle mass.

[3] For low momenta the curvature of the trajectory is large, which possibly renders the particle not to reach the first detector layers

[4] Technically the current LHCb Vertex Locator is a silicon strip detector, but will be upgraded to a silicon pixel detector. Furthermore, hybrid pixels are used in the ring imaging Cherenkov detector.

They mainly consist of a network of metal-oxide-semiconductor field-effect transistors (MOSFET), which are explained in section 1.3 [3].

For the application of silicon pixel detectors in high-energy particle and nuclear physics experiments a detector architecture featuring so-called *hybrid pixels* is developed in order to best meet the aforementioned requirements of such systems. Especially, the radiation tolerance is a driving factor for this detector design. A schematic of a typical hybrid pixel detector using the example of the CMS pixel detector is shown in figure 1.1 on the left. The main feature of this hybrid architecture is the separation of readout and sensing part. Consequently, there are two different (silicon) chips which need to be electrically connected by the means of metal bump bonds, shown as red dots. A traversing charged particle generates an electrical signal only in the pixels of the sensor chip. It is then transferred to the corresponding pixel unit cell on the readout chip housing all the required electronics to further process it. Finally, the data of the full sensor is shipped off to be taken into storage.

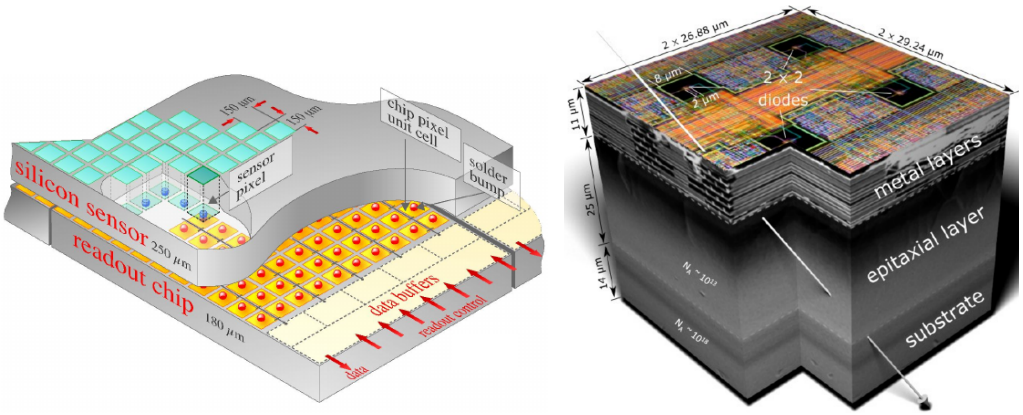

Figure 1.1 **(left)** Schematic 3D illustration of a hybrid pixel sensor using the example of the CMS pixel detector. The silicon readout chip and and the pixelated sensor are two separate entities, which are connected by means of metal bump bonds (red dots). Both readout and sensor chip are few $100\,\mu\mathrm{m}$ thick, while the pixel size is $150\,\mu\mathrm{m} \times 150\,\mu\mathrm{m}$ [4].
(right) Schematic 3D illustration of a Monolithic Active Pixel Sensor (MAPS) using the example of a 2×2 pixel matrix of an ALPIDE sensor. The readout electronics and its metal interconnections are directly implemented on top of the sensitive volume, which is realised as a thin epitaxial layer. Thus readout and sensing part are produced on the same chip. The chip is thinned down to $50\,\mu\mathrm{m}$. A traversing particle is shown as a grey arrow [5].

In order to optimise this technology both silicon sensor and readout chip are thinned down such that the particle trajectory and energy is as less disturbed by the detector material as possible. Furthermore, the pixel size can be reduced in order to decrease the position resolution. However, this also decreases the pitch of the bump bonds. Both of these optimisation options come with technical limitations. Hence, hybrid pixel detectors usually have a total thickness of several $100\,\mu\mathrm{m}$ and a pixel pitch ranging from below $100\,\mu\mathrm{m}$ to a couple of $100\,\mu\mathrm{m}$ [1]. Nowadays, these limitations are reached with state of the art hybrid silicon pixel detectors.

One approach to overcome the limitations of hybrid pixel detectors is the *monolithic active pixel sensor* (MAPS). As schematically illustrated in figure 1.1 on the right, the sensing volume and the required readout electronics are implemented on top of each other on the same substrate for these kind of detectors. This leads to a single sensor chip hosting the full pixel matrix as it can be seen in the example of the ALICE Pixel Detector (ALPIDE) architecture. As a consequence, the pixel size is now limited by the complexity of the implemented in-pixel electronics and the feature size of its single electrical components. Having only a thin epitaxial layer, the entire chip

can be thinned down to multiple $10\,\mu\mathrm{m}$ leading to an unprecedented low material budget for a solid state detector. Thus, MAPS meet most of the demanding requirements for particle detectors. However, a long research and development phase was necessary in order to bring this technology to a sufficiently radiation hard state [2]. Also further limitations, for instance relatively long readout times as compared to hybrid pixel detectors, exist and have to be overcome [1, 6]. The application of MAPS in high-energy physics experiments is described in chapter 2. Examples of full-scale MAPS-based tracking detectors are given in section 2.2 and 2.3.

In order to understand the working principle of MAPS presented in section 1.5 the following sections 1.1, 1.2 and 1.3 treat basic semiconductor electronics. A short overview on the energy loss of charged particles traversing silicon is given in section 1.4.

1.1 Intrinsic and doped silicon

Probably silicon is the most prominent example of an intrinsic semiconductor. In a semiconductor free charge carriers in the form of electron-hole ($e-h$) pairs are constantly produced by thermal excitation. Only these free charge carriers contribute to the electrical conductivity of the semiconductor. As a consequence, it acts like an insulator at absolute zero temperature $T = 0\,\mathrm{K}$, since no thermal excitation of free charge carriers is possible at this point.

This behaviour of silicon can be understood in the picture of the band model. Due to quantum mechanical principles there are discrete energy levels, so-called *bands*, in the silicon crystal. These can be occupied by electrons following Fermi-Dirac statistics. In between two bands there is a gap, i.e. electrons with these energies cannot exist in the crystal. At $T = 0\,\mathrm{K}$ the *valence band* and according to Pauli's principle every band with a lower energy is fully occupied, while no electron has enough energy to populate a state in the higher *conduction band*. As such, no electrical conduction is possible.

Considering non-zero temperatures $T > 0\,\mathrm{K}$ electrons energetically located in the valence band can be thermally excited and thus overcome the band gap in order to populate a free state in the conduction band. The *absence* of the electron in the valence band, which is referred to as hole, can be considered as an effectively positive charge. In an intrinsic semiconductor electrons and holes are always created as pairs, therefore an intrinsic charge carrier concentration n_i can be defined as

$$n_i = n = p \tag{1.1}$$

where n and p denote the (conduction) electron density and the hole density, respectively. Once created, an electron from the conduction band and a hole in the valence band can also recombine again. Under stable environmental conditions an equilibrium is established between these two counteracting processes. From Fermi-Dirac statistics it can be derived that the intrinsic electron-hole pair concentration follows a Boltzmann distribution as given in equation 1.2 [3, 7].

$$n_i \propto \exp\left(-\frac{E_\mathrm{g}}{k_\mathrm{B}T}\right) \tag{1.2}$$

Here, E_g denotes the energy gap between conduction and valence band, while k_B is the Boltzmann constant. At room temperature $T = 293\,\mathrm{K}$ and $E_\mathrm{g} = 1.12\,\mathrm{eV}$ the exact calculation yields $n_i \approx 1.5 \times 10^{10}\,\mathrm{cm}^{-3}$ in the case of silicon. For comparison purposes, metals like aluminium

feature charge carrier concentrations of the order of $10^{21}\,\mathrm{cm}^{-3}$ [3, 8]. As a consequence, the electrical conductivity σ for an intrinsic semiconductor given by

$$\begin{aligned} \sigma &= e(n\mu_n + p\mu_p) \\ \sigma_i &= e \cdot n_i(\mu_n + \mu_p) \end{aligned} \tag{1.3}$$

is relatively low as compared to the one for metals. Here, μ_n and μ_p respectively describe electron and hole mobility, while e denotes the elementary charge. Inserting $\mu_n = 1350\,\mathrm{cm}^2\,\mathrm{V}^{-1}\,\mathrm{s}^{-1}$ and $\mu_p = 476\,\mathrm{cm}^2\,\mathrm{V}^{-1}\,\mathrm{s}^{-1}$ in equation 1.3 the resistivity of intrinsic silicon can be calculated[5] according to equation 1.4. At room temperature this yields $\rho_i \approx 230\,\mathrm{k\Omega\,cm}$ [8]. Due to its high resistivity intrinsic silicon is not suitable for the majority of application in electronic devices

$$\begin{aligned} \rho &= \frac{1}{\sigma} = \frac{1}{e(n\mu_n + p\mu_p)} \\ \rho_i &= \frac{1}{\sigma_i} = \frac{1}{e \cdot n_i(\mu_n + \mu_p)} \end{aligned} \tag{1.4}$$

In order to increase the conductivity of silicon and thus overcome the limitations of intrinsic silicon its charge carrier density can be enhanced by *doping*. In this case doping refers to either adding pentavalent atoms such as boron in order to create *n-type* silicon, or trivalent atoms like antimony for *p-type* silicon. A central quantity to describe the electronic behaviour of (doped) semiconductors is the *Fermi level* E_F. By definition it is the (thermodynamic) work that needs to be performed in order to add one electron to the system. As such it can be calculated as the mean energy value of the highest occupied energy state and the lowest accessible, but not populated, energy state at $T = 0\,\mathrm{K}$ [3]. Consequently, the Fermi level lies in between conduction and valence band in the case of semiconductors. If this energy level could be hypothetically populated by an electron having the corresponding energy, the occupation probability of this level would be $50\,\%$. Hence, it is a measure of how many states are on average occupied at a certain energy.

Figure 1.2 schematically shows the effect of both types of doping on the band structure of silicon. In the case of p-doping, depicted on the left, the trivalent atoms introduce new accessible locally bound energy levels close to the valence band. Since the energy difference $E_\mathrm{A} - E_\mathrm{V}$ is only about $50\,\mathrm{meV}$, basically all of these introduced energy levels are populated by electrons from the valence band at room temperature. Thus, each *acceptor atom* effectively adds one hole to the silicon that can now contribute to its conductivity. As a consequence, the intrinsic Fermi level is shifted towards a lower value in this case [3]. Given the fact that usually the acceptor concentration N_A is chosen such that $n_i \ll N_\mathrm{A}$, the hole concentration in p-doped silicon is majorly given by

$$p \approx N_\mathrm{A} \tag{1.5}$$

From the law of mass action (equation 1.7) and the overall electrical neutrality of the doped silicon crystal (equation 1.8) the electron density can be calculated as

$$n = \frac{n_i^2}{N_\mathrm{A}} \tag{1.6}$$

$$n \cdot p = n_i^2 \tag{1.7}$$

[5] Mobility values for room temperature. It is clear that the hole mobility is significantly lower as compared to the one of electrons, since the movement of a hole can be understood as a collective movement of the remaining electrons in the valence band in the opposite direction.

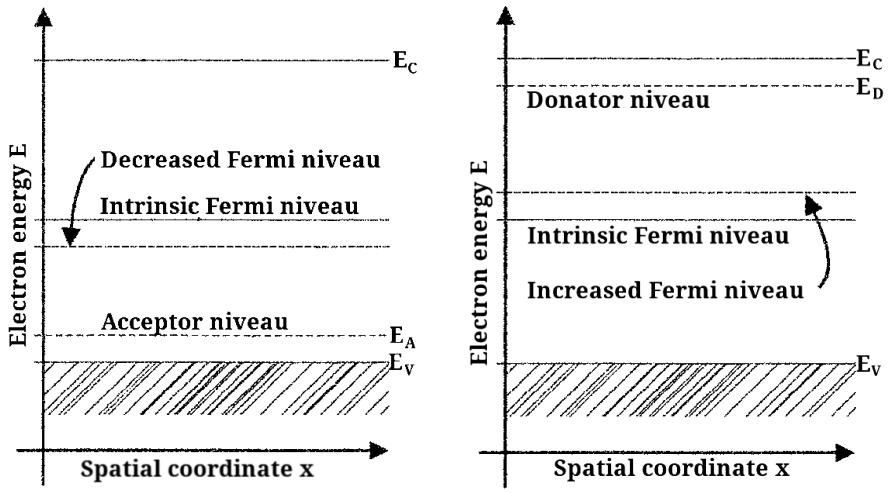

Figure 1.2 **(left)** Sketch of the band structure and energy levels in p-type silicon. The introduced concentration of acceptor atoms lead to an additional accessible energy level (E_A) slightly above the valence band (E_V). This small energy difference corresponds to a potential difference of about $50\,\mathrm{mV}$. The Fermi level (E_F) is shifted to a lower value as a consequence of the p-doping. Adapted from [3]
(right) Sketch of the band structure and energy levels in n-type silicon. The introduced concentration of donor atoms lead to an additional energy level (E_D) slightly below the conduction band (E_C). The Fermi level (E_F) is shifted to a higher value as a consequence of the n-doping. Adapted from [3]

$$n = p + N_\mathrm{A} \tag{1.8}$$

For this reason, electrons are referred to as *minority* charge carriers, while holes are the *majority* charge carriers in p-type silicon. Analog consideration can be done for n-doped silicon. As illustrated on the right side of figure 1.2 introducing pentavalent atoms to the silicon crystal spatially bound energy levels are created close to the conduction band for each dopant. Again due to the small energy difference $E_\mathrm{C} - E_\mathrm{D}$ outer shell electrons from these so-called *donor atoms* are exited to the conduction band. At room temperature basically each donor contributes one electron to the conduction band, thus enhancing the conductivity of the n-type silicon with respect to intrinsic silicon. Consequently, the Fermi level shifts towards higher energies. Given that the donor concentration N_D is chosen such that $N_\mathrm{D} \gg n_i$, it follows that the electron concentration is mainly given by the dopant concentration while the hole concentration can be calculated analog to equation 1.6 as follows.

$$n \approx N_\mathrm{D} \tag{1.9}$$

$$p = \frac{n_i^2}{N_\mathrm{D}} \tag{1.10}$$

Hence, electrons are the majority charge carriers in n-type silicon, while holes are the minority charge carriers. For further considerations of the conductivity and resistivity of doped silicon according to equations 1.3 and 1.4 it has to be taken into account that the introduced dopants act as impurities within the silicon crystal lattice. As such they impact the mobility of the free charge carriers [7]. In general, the conductivity of silicon can be improved by orders of magnitude and tuned by controlling the dopant concentration and type.

1.2 Anisotype (p-n) junction

Bringing together p-type and n-type silicon, a junction forms which is the basis for a multitude of electronic devices such as diodes and transistors. In order to understand the functionality of these devices it is therefore crucial to understand the physics of such an anisotype junction. A sketch of a p-n junction[6] with special focus on the interface of p- to n-type silicon is shown in figure 1.3 at the top left.

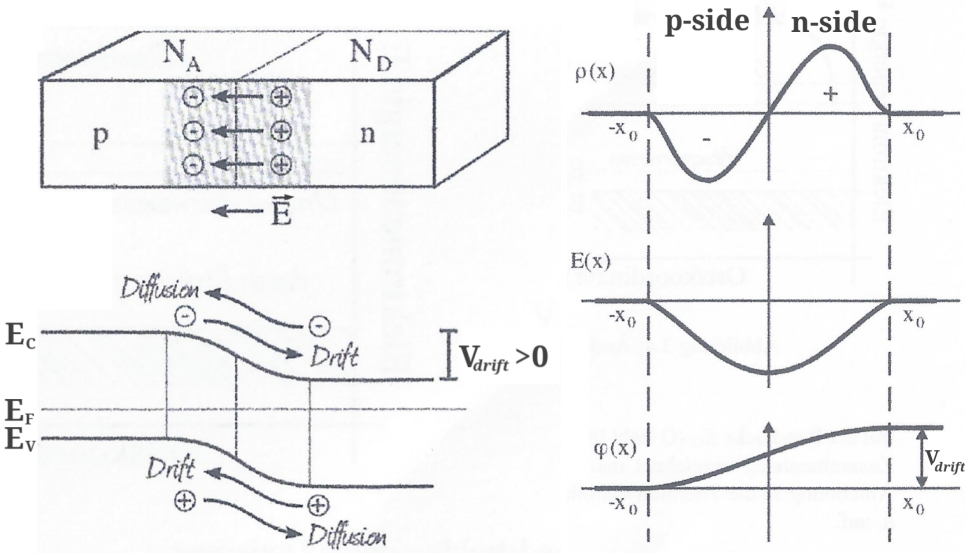

Figure 1.3 **(left)** (top) 3D sketch of a p-n junction with the *depletion* or *space charge* region which develops at the interface of the involved p- and n-type semiconductor. The space charges lead to an electrical field denoted by $\vec{E}$. Acceptor and donor concentrations are labelled as N_A and N_D, respectively. (bottom) Energy levels across a p-n junction in equilibrium. The energies of conduction E_C and valence band E_V as well as the Fermi energy E_F are shown. Drift and diffusion currents of electrons and holes are depicted by arrows. Adapted from [3]. **(right)** Charge carrier concentration $\rho(x)$, electrical field strength $E(x)$ and electrostatic potential $\varphi(x)$ across a p-n junction in equilibrium. The depletion region ranges from spatial coordinate $-x_0$ to x_0. The potential difference driving the charge carrier drift is labelled as V_drift. Adapted from [3].

It is clear that after joining p- and n-type silicon there is large concentration gradient across the junction considering the majority charge carriers on each side. As a consequence, holes start diffusing from the p-side to the n-side, where they eventually recombine with electrons. On the other hand, electrons diffuse from n- to p-side and recombine with holes. Since both parts are overall electrically neutral, the *missing* electrons in the n-side and holes in the p-side lead to positive and negative stationary *space charges*[7], respectively. As such an electrical field $\vec{E}$ develops in the junction region as illustrated in figure 1.3 at the top left. Since this region is devoid of free charge carriers it is referred to as *depletion region*. The electrical field now leads to a drift of minority charge carriers to the opposite side, hence counteracting the diffusion of majority charge carriers. This means holes from the n-side start drifting back to the p-side and vice versa for electrons. Eventually, the effect of drift and diffusion become equally large and an equilibrium is established [3, 7].

As this process affects the occupation of the energy bands in the respective parts, they shift as illustrated in figure 1.3 at the bottom left. Drift and diffusion directions for the free charge carriers

[6] Not to be confused with the similar sounding PiNapple junction illustrated in figure A.1 in the appendix.
[7] Ionised donor atoms (+) and electron receiving aceptor atoms (-), which have fixed locations in the crystal lattice.

are also depicted there. The potential difference, which drives the drift of the minority charge carriers, is referred to as V_{drift} and can be calculated from the space charge concentration across $\rho(x)$ the depletion region. Assuming equal dopant concentrations for p- and n-side, the space charge distribution across the junction is symmetric as depicted in the upper plot of figure 1.3 on the right. The run of the resulting electrical field curve $E(x)$ can be calculated by integration according to

$$E(x) = \int_{-x_0}^{x} \frac{\rho(x')}{\epsilon_0 \epsilon_r} dx' \tag{1.11}$$

Here, ϵ_0 and ϵ_r represent the dielectric constants. Integrating the electrical field strength according to equation 1.12 illustrated in the middle plot finally yields the electrostatic potential $\varphi(x)$ across the junction, which is shown in the lower plot.

$$\varphi(x) = -\int_{-x_0}^{x} E(x')dx' \tag{1.12}$$

The potential difference V_{drift} can then be influenced by separately contacting the p- and n-side and applying a *bias voltage* across the junction. Depending on the polarity and magnitude of the voltage applied, the electrical properties of the p-n junction can be tuned. For the application as an electronic device such an anisotype junction is a simple *diode*.

As further described in section 1.5 especially the *reverse-bias mode* of a diode is crucial for the functionality of a particle detector such as a MAPS. In the reverse-bias scenario the polarity of voltage applied across the diode is such that it enhances the in-built electrical field in the space charge region and thus increases V_{drift}. Consequently, the depletion region can be further enlarged with an increasing absolute bias voltage until eventually the full device is depleted [8].

1.3 Working principle of transistors

In addition to the diode, the transistor is another electronic device, which relies on p-n junctions. Nowadays, transistors are one of the most frequently produced electronic devices as billions of them are integrated on each computer chip. There are different types of transistors, which can be realised as an electronic device in different ways. For this work only the so-called metal-oxide semiconductor field-effect transistor (MOSFET) is of special interest in order to understand the working principle of MAPS.

In general MOSFETs come in two flavours depending on how they are realised. Basically build from two p-n junctions, they can either be implemented as n-p-n or p-n-p transistors. Here, the first type is referred to as n-type or n-channel MOS transistor, while the latter analogously is called PMOS transistor. As their general idea and their working principle basically is the same, the following explanations and considerations are only made for the NMOS case. However, taking into account the opposite doping profile of PMOS transistors, analog conclusions can be reached for this case as well.

On the left side of figure 1.4 a possible realisation of an NMOS transistor is schematically shown. In this cross section it is clearly visible that a MOS transistor features four different connections, namely *source*, *drain*, *gate* and the *substrate*, which is sometimes referred to as bulk. As it is an NMOS transistor, the substrate has to be of p-type. Source and drain are connected to separate n-type implants, thus leading to two p-n junctions. In between these two connections, there is a metal oxide electrical insulation layer on top of the p-substrate. Usually, silicon dioxide is used for

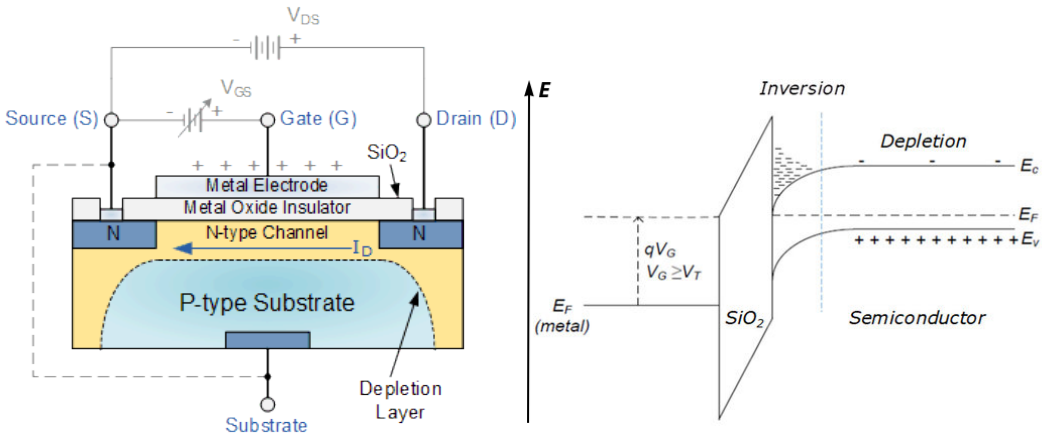

Figure 1.4 **(left)** Schematic cross section through a possible implementation of an n-channel metal-oxide semiconductor (NMOS) field-effect transistor (FET). There are two n-type implants, which make up the *source* (S) and *drain* (D) connection of the transistor. Together with the p-type substrate they both basically act like a diode. Between source and drain there is a MOS capacitor consisting of a insulation layer and a metal *gate* electrode (G). Depending on the bias denoted by the wiring diagram the drain current I_D can be controlled [9]. **(right)** Schematic illustration of the effect of a MOS capacitor on the energy levels in a semiconductor. It is visible that for a sufficiently high gate voltage V_G a conducting inversion layer builds up on the semiconductor side [10].

this purpose. Together with a metal electrode[8] connected to the gate. A so called MOS capacitor is realised in between drain and source [11, 3].

As described in section 1.2 the p-n junctions at source and drain behave according to first principles. As such a depletion region develops at the interfaces of the n-type implants and the p-type substrate. If biased accordingly the dimension and shape of this depletion layer can be controlled. Furthermore, if the gate is biased as shown in the figure, a configuration of drain-source voltage V_DS and gate-source voltage V_GS can be reached, where the entire volume in between the n-type implants is depleted. Consequently, no electrical current can flow between source and drain as there are no free charge carriers available[9].

The behaviour of the illustrated NMOS transistor regarding its electrical conductivity is mainly given by the impact of the MOS capacitance at the gate on the semiconductor region between source and drain. For this purpose the energy levels across a MOS capacitance are schematically illustrated on the right side of figure 1.4. It can be seen that both band energies, i.e. E_C and E_V, are decreased in the proximity of the semiconductor-insulator interface. Consequently, these lower energy states in the conduction band are more likely to be populated by electrons.

If the gate electrode is set to a potential V_G such that positive charge accumulates there, holes in their role as majority charge carriers in p-type silicon are driven away from the semiconductor-insulator interface. Effectively, the semiconductor is depleted of free charge carriers starting in the vicinity of the insulation layer. The larger the gate potential is, the larger the extension of the depletion region is. As a consequence, a negative charge originating from the stationary acceptor atoms builds up in this depletion region. If the gate potential exceeds a threshold value $V_\mathrm{G} > V_\mathrm{T}$ electrons as minority charge carriers are attracted and accumulate at the semiconductor-insulator interface. They effectively make up a so called *inversion layer*. In the case of the NMOS transistor

[8] Due to the manufacturing process usually highly doped polysilicon, which features metallic behaviour, is used as a gate electrode [10].
[9] In fact a very small *leakage current* is always present.

a conducting n-type channel builds up in between source and drain thus allowing the flow of a drain current I_{D} [11, 3].

As such the width of the of the n-channel and hence the conductivity in between source and drain increases with increasing gate potential. Consequently, the current through the transistor can be regulated via the gate potential. Furthermore, for $V_{\mathrm{DS}} < V_{\mathrm{GS}} - V_{\mathrm{T}}$ the transistor is in *ohmic mode*, i.e. $I_{\mathrm{D}} \propto V_{\mathrm{DS}}$ [3].

Utilising NMOS and PMOS transistors with their respective electrical behaviour, circuits can be built that allow to perform logic operations on a set of input signals. Moreover, registers that can be set to either an *on* or an *off* state, i.e. the representation of a bit, can be realised with these complementary metal-oxide semiconductor (CMOS) circuits. In its application for MAPS, CMOS technology provides the means of realising compact and efficient in-pixel circuitry in order to readout, shape and further process a measured electrical signal originating from a traversing charged particle.

1.4 Energy loss of charged particles in silicon

In order to be detected, particles need to interact with the detector material in some way. When particles traverse a detector, they deposit a fraction of their energy in its sensitive volume. As such, they generate a measurable signal. Often this initial signal is of electrical nature and can therefore be picked up and further processed by dedicated readout electronics. If this is not directly the case it has to be translated to an electrical signal via further processes. As the scope of this work are pixelated solid state tracking detectors the focus lies on the detection of charged particles. Since most of these detectors and especially MAPS are predominately made out of silicon, the energy loss properties of charged particles are discussed given this context in the following.

Despite other possible energy loss mechanisms only *ionisation* plays a crucial role for the key functionality of silicon tracking detectors. The mean energy loss rate of charged particles is given by the Bethe-Bloch formula[10] as shown in equation 1.13 [13].

$$-\left\langle \frac{dE}{dx} \right\rangle = K z^2 \frac{Z}{A} \frac{1}{\beta^2} \left[\frac{1}{2} \ln \left(\frac{2 m_e c^2 \beta^2 \gamma^2 T_{\max}}{I^2} \right) - \beta^2 - \frac{\delta(\beta\gamma)}{2} \right] \tag{1.13}$$

$\mathbf{K}$: constant, $\mathbf{z}$: electrical charge of the passing particle, $\mathbf{Z}$: charge number of the passed medium, $\mathbf{A}$: atomic mass of the medium, $\mathbf{m_e}$: electron mass, $\mathbf{c}$: speed of light, β: velocity of the incident particle, γ: Lorentz factor, $\mathbf{T}_{\max}$: maximal energy transfer in a single collision with a shell electron of the medium, $\mathbf{I}$: mean excitation energy of the medium, δ: density correction

This formula is valid for moderately relativistic charged particles, i.e. $0.05 < \beta\gamma < 500$, with a significantly higher mass m as compared to the electron mass m_e. In order to make the mean energy loss rate material independent, it is often normalised to the density of the traversed medium. As such, a general energy regime of about $3 < \beta\gamma < 4$ can be identified, where the energy loss rate of the considered particle is minimal. Particles with this energy are therefore referred to as minimum ionising particles (MIP). As a rule of thumb a MIP looses about $1.5\,\mathrm{MeV\,g^{-1}\,cm^2}$ [14]. Due to their properties they play a major role as reference for detector calibration and especially for performance studies on detector prototypes in the development phase.

Since the Bethe-Bloch formula only makes a statement about the *mean* energy loss rate of a charged particle, also fluctuations of the total energy loss rates can be considered. In general, the distribution of absolute energy loss rates can be described by probability density functions (PDF). Which kind of PDF is applicable depends on the material thickness that is traversed by the charged particle. Considering very thick silicon sensors, the traversing charged particle

[10] Original publication by Bethe in 1930 [12].

deposits a significant fraction of its original energy in the detector material. Hence, the number of interactions of the traversing particle with atoms of the detector material is sufficiently large so that the central limit theorem can be applied. Consequently, the energy loss rate distribution is increasingly well described as a Gaussian with increasing sensor thickness. As a rule of thumb, a Gaussian distribution can be assumed if the particle looses about half of its initial energy when penetrating through the detector [15].

In the case of thin silicon sensors featuring thicknesses of about $300\,\mu\mathrm{m}$ and moderately larger values the energy loss rate distribution is well described by the Landau model. As described in the first part of this chapter, this especially applies to hybrid pixel sensors in their application as tracking detectors, since they typically feature chip thicknesses of several $100\,\mu\mathrm{m}$. The most striking characteristic of the asymmetric Landau distribution is its pronounced *tail* towards high energy losses. These are attributed to the generation of so-called $\delta - electrons$ [16, 14]. A δ-electron is an electron emerging from the ionisation of a detector material atom. It has enough energy to further ionise the detector material, which is referred to as *secondary ionisation*.

The Landau model has its limits in describing the straggling of the energy loss rate for ultra-thin silicon sensors featuring material thicknesses below $160\,\mu\mathrm{m}$. This usually is the case for MAPS, which can be thinned down to only several $10\,\mu\mathrm{m}$. In this case the most probable value (MPV) of the energy loss rate is underestimated, while its width is overestimated. Taking this into account, the distribution of the energy loss rate for ultra-thin silicon detectors can be described with the *Bichsel model*. In the case of MAPS with a sensitive layer thickness of about $20\,\mu\mathrm{m}$ to $30\,\mu\mathrm{m}$ the MPV of the energy loss rate is determined to a value of about $60\,\mathrm{eV}\,\mu\mathrm{m}^{-1}$ [5, 17].

As mentioned above, the energy loss of electrons in silicon is not covered by the Bethe-Bloch formula for various reasons. As such, electrons are a special case and thus need further considerations. For one, electrons are more prone to be scattered to larger angles as compared to heavier charged particles. Due to their low mass, they can loose a large fraction of their energy in a collision with a shell electron of a detector material atom. Furthermore, the participating electrons in such a collision are indistinguishable, such that quantum mechanical effects need to be considered. Taking into account all these effects the Bethe-Bloch formula can be modified in order to describe the energy loss of electrons by ionisation [13, 18].

Furthermore, electrons at moderate energies are already subject to Bremsstrahlung due to their low mass. This describes the emission of a high energy photon, if an incident electron is deflected in the electrical field of a nucleus within the detector material. As such ionisation describes only a fraction of the energy loss for electrons traversing a detector. For instance the critical energy of silicon is $E_\mathrm{C} = 40.19\,\mathrm{MeV}$. Electrons of this energy loose as much energy by ionisation as by Bremsstrahlung [19, 14].

1.5 Working principle of a MAPS

For the application in particle and nuclear physics experiments MAPS share a common general structure. A schematic cross section of a MAPS using the example of the ALICE Pixel Detector (ALPIDE) design and featuring all the main components is shown in figure 1.5. Starting from the bottom there is a highly p-doped silicon *substrate* (P++), which mainly acts as mechanical support for the chip. On top of the substrate a lesser p-doped *epitaxial layer* (P-) is implemented, which is usually a few tens of micrometers thin as it can be seen in figure 1.1 on the right. The epitaxial layer is the sensitive part of a MAPS, i.e. the initial signal due to the impact of a traversing charged particle is created there.

Furthermore, each pixel of a MAPS features a *collection diode*, which is realised as a highly doped n-type implant (green) at the top of the epitaxial layer. As the name already suggests, free negative charge carriers like electrons can be collected there. The induced electrical signal can then be further processed by the integrated *CMOS transistor* network. As schematically shown in figure 1.4 on the right source and drain connection of MOSFETS are realised as oppositely doped implants within a doped base material. Both types of MOS transistors, namely NMOS and PMOS, are therefore realised inside of so-called *wells*, which act as the doped *transistor substrate*. Consequently, NMOS transistors are located inside p-wells (light red) and PMOS transistors need n-wells (light green) for proper functioning. As such, a full CMOS circuitry can be manufactured on top of the chip's sensitive layer.

However, the implementation of PMOS transistors on top of the epitaxial layer comes with the problem that their n-well would also act like a diode. Hence, charge from the signal could in principle also be collected at these transistor n-wells. In order not to disturb the charge collection at the dedicated collection diode, the n-wells introduced to host the in-pixel electronic components need to be *shielded* from the epitaxial layer. For this purpose, a deeper lying p-well is introduced. To extend this deep p-well also beyond the transistor n-wells, as it is shown in figure 1.5, is beneficial for the depletion of the epitaxial layer when the collection diode is biased according to the shown biasing scheme. The extended deep p-well is specific to the ALPIDE design and is thus not generally present in other MAPS [20].

Lastly, several metallised layers are produced on the very top of the chip in order to interconnect the electronic devices making up the in-pixel and chip circuitry. Only with all components and the correct electrical connections between them in place the intended functionality of the chip can be ensured. Manufacturing defects can therefore lead to malfunctioning or even inoperable pixels. Depending on the chip design these defects can even affect entire chip regions as for instance an entire column of pixels.

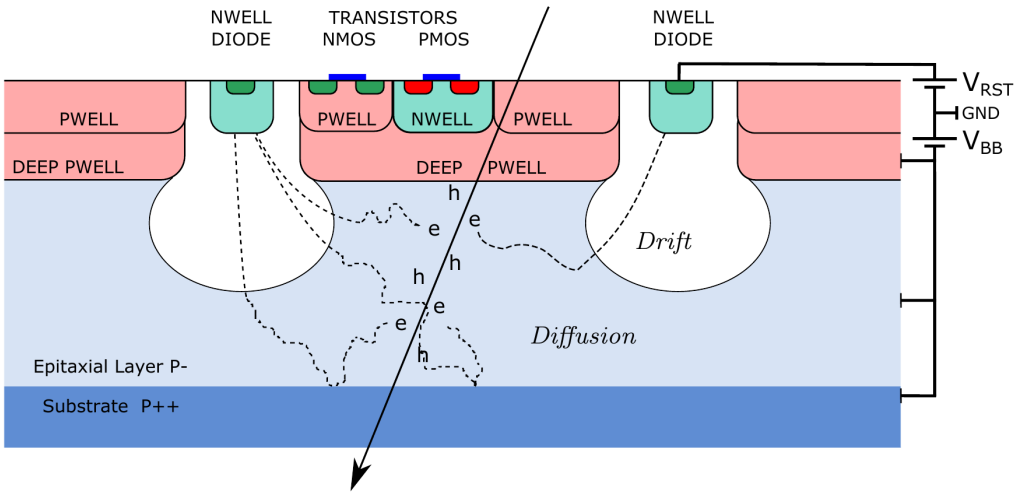

Figure 1.5 Schematic cross section through a MAPS (not to scale). The p-type substrate and epitaxial layer are denoted in blue. On top of the active volume, there is the integrated electrical circuitry, which is repeated for each pixel. It consists of a n-type collection diode and a transistor network utilising NMOS and PMOS transistors. To shield the electronics from the active volume there is a deep p-type implant (ALPIDE specific). The biasing scheme is depicted on the right side. Additionally, a traversing ionising particle is indicated as the black arrow [20].

For the use of MAPS as a particle detector usually a back-bias voltage V_{BB} is applied to the chip in order to enlarge the depletion region at the collection diode within each pixel. In the

case of the ALPIDE chip up to $V_{\mathrm{BB}} = -6\,\mathrm{V}$ can be applied, whereas $V_{\mathrm{BB}} = -3\,\mathrm{V}$ is the nominal value [21]. As depicted in the schematic cross section of the MAPS, the depletion regions shown in white do not necessarily extend throughout the entire epitaxial layer. An ALPIDE chip can even be operated without applying any back-bias voltage.

If a charged particle passes through a MAPS, electron-hole pairs are generated along its trajectory as thoroughly described in the previous section 1.4 and depicted in figure 1.5 around the black arrow. Since only the more mobile and thus faster electrons are exploited for the signal creation in a MAPS. Their paths are exemplarily illustrated as dotted lines. Once created in the epitaxial layer, the electrons start to diffuse until they enter a depletion region or recombine. For a well behaved sensor, i.e. no or only little defects are present, the recombination plays a negligible role. Since isotype P^{-}-P^{++} junctions (also P^{-}-p-well) behave like a reflective barrier, the diffusing electrons do not escape the epitaxial layer. However, electrons created in the substrate can diffuse into the epitaxial layer and thus contribute to the signal. Entering or already being created in a depletion region, electrons start drifting in the in-built electrical field towards the n-implant of the collection diode. There, they are collected and hence form the electrical signal. Considering a vertically traversing MIP and an epitaxial layer of $25\,\mu\mathrm{m}$[11] roughly $1500e$ in the form of electron-hole pairs are created [5]. Additionally, figure 1.5 shows that the charge created by one traversing particle does not necessarily only end up and gets collected inside of one pixel. It is intuitively understandable that this charge sharing effect amongst adjacent pixels is suppressed for larger depletion regions, i.e. a higher absolute back-bias voltage.

In order to create a signal from the collected electron charge Q_{e}, which is then further shaped and processed by the in-pixel electronics, the *input capacitance* C_{pixel} of the pixel plays a major role. According to

$$\Delta V_{\mathrm{signal}} = \frac{Q_{\mathrm{e}}}{C_{\mathrm{pixel}}} \tag{1.14}$$

the charge collection causes a voltage drop $\Delta V_{\mathrm{signal}}$ at the input capacitance. Consequently, it has to be recharged to the initial level after a signal is registered. This is done by applying the reset potential V_{RST}.

The performance of a MAPS can be optimised by tuning several design parameters. In this case performance refers to an as high as possible signal to noise ratio (SNR). As the name already suggests this can be achieved by a higher signal amplitude, i.e. a larger $\Delta V_{\mathrm{signal}}$. According to equation 1.14 the amount of collected charge could be increased by increasing the thickness of the epitaxial layer or the input capacitance of the pixel can be reduced for this purpose. The first option is not beneficial, since a particle detector should feature as less material budget as reasonably possible in order not to disturb the measured particle in the sense of impacting its momentum and energy. For the latter option there are two contributions to C_{pixel} that need to be considered. One is the reduction of the *parasitic capacitance* of the in-pixel circuitry. This can be realised by an efficient and optimised circuit design. The other contribution is the capacitance at the junction of the collection diode itself. For reducing this one, the size of the n-type implant as well as its geometry and distance to the surrounding p-wells can be optimised in this sense [20, 5].

A general approach to increase the sensor performance in the sense of position resolution is to reduce the pixel pitch as much as possible. However, this option is limited by the size and therefore complexity of the integrated in-pixel circuitry. It is obvious that a smaller feature size, i.e. size of a transistor or other electrical components, is beneficial regarding this limit. The feature size is given by the manufacturing process. With state of the art technology pixel sizes of several $10\,\mu\mathrm{m} \times 10\,\mu\mathrm{m}$ are possible.

[11] As it is the case for the ALPIDE sensor.

2 Application of MAPS in high-energy heavy-ion physics experiments

For the application of MAPS in high-energy particle and nuclear physics experiments two key parameters need to be especially considered and improved. By design and thus working principle of MAPS, these are *radiation tolerance* and *timing* in the sense of timing resolution and readout speed. They are manifested in the manufacturing processes of commercial CMOS sensors, which naturally are not optimised for this field of application.

As briefly indicated in the first part of this chapter, MAPS are more affected by the effects of radiation damage as compared to hybrid pixel detectors. One reason for this is that they are usually operated at low or moderate back-bias voltages as compared to hybrid pixels, where the sensor can be fully depleted applying a high-voltage to it. On the contrary, the epitaxial layer material of a MAPS features a limited resistivity. Therefore, the active volume of the sensor is usually not fully depleted when a moderate back-bias voltage is applied. Thus the signal charge collection strongly depends on the slower diffusion process rather than the fast drift of the charge in an electrical field. As such, the signal charge is more prone to be trapped by defects introduced by radiation. In addition, the overall thin active volume leads to less primary signal charge as compared to the significantly thicker hybrid pixel sensors. If now the same amount of signal charge is trapped in both sensors due to radiation induced effects, it is lost to the signal generation process. This trapped charge might be only a very small fraction of the overall charge generated in a hybrid pixel sensor, while it is a sizeable fraction in the case of MAPS. Consequently, the signal-to-noise ratio decreases and therefore also the overall sensor performance starts degrading already at lower irradiation levels as compared to hybrid pixel sensors [22].

In general, two different mechanisms of radiation damage can be identified, while the sum of the two are responsible for the resulting overall degradation of the sensor performance. On the one hand, there is the damage caused by ionisation, which is hence described by the total ionising dose (TID). The ionisation of the bulk material of the sensor, i.e. substrate and epitaxial layer, is intended in order to ensure a proper functionality of the sensor. As such ionisation effects in these regions are usually reversible. On the contrary, in the insulation layers (often SiO_2) of the in-pixel circuitry, ionisation can cause permanent damage. There, trapped charge from ionisation can accumulate and lead to parasitic electrical fields. Consequently, they impact the functionality of the corresponding MOS transistors and thus alter the working point of the affected pixel or lead to an increased noise level by triggering leakage currents [22, 6]. In the digital part of the in-pixel circuitry ionising particles can lead to a temporary or even permanent change of the state of a register.

On the other hand non-ionising energy loss (NIEL) can have a negative influence on the sensor performance. Following the impact of an incident particle, silicon atoms are displaced with respect to their original positions in the crystal lattice. It is clear that this leads to altered electrical properties of the crystal. More precisely, additional energy levels are created within the band gap. These defects promote the creation and recombination of free charge carriers in the active region of the sensor. Hence, the thermal leakage current through the collection diode and thus the overall noise level in the affected pixel increases [22].

The second constraint is the limited timing resolution, which at least can be partly attributed to the diffusion component in the charge collection process. Both, timing resolution and radiation tolerance of MAPS have significantly developed over the last couple of years. A detailed overview of the improvements in radiation tolerance is given in [22]. Considering the already achieved optimisation of MAPS and establishing dedicated research and development programs targeting the previously discussed properties, the field of MAPS development quickly advances. As such, the possibility for their application in (future) high-energy particle and nuclear physics experiments opens. In this scope, they have to meet the demanding requirements and need to maintain their performance in the harsh conditions of the environment.

Especially particle physics experiments, as for instance ATLAS and CMS located at CERN's LHC, which are dedicated to perform precision measurements on specific particle physics processes, have very stringent requirements in terms of radiation tolerance and readout times. As compared to them, heavy-ion experiments such as the ALICE experiment feature less stringent conditions on the radiation hardness even of the innermost tracking detector layers, as well as their readout rate. Therefore, state of the art MAPS are a viable and promising option for these kind of experiments.

In order to further motivate the application of MAPS in tracking detectors for high-energy heavy-ion experiments, their physics program and motivation must be understood. For this purpose a brief introduction to strongly interacting matter, especially in a state called quark-gluon plasma (QGP), is given in the following section. The sections 2.2 and 2.3 give concrete examples of actual and intended applications of MAPS in full-scale detectors. Even their application as truly cylindrical, i.e. bent, sensors is presented.

2.1 Strongly interacting matter at extreme energy densities

In general, particle physics processes are well described by the standard model of particle physics. It is a very successful theory classifying a set of elementary particles such as quarks, leptons and gauge bosons. Furthermore, it describes the interactions amongst them and their composite particles. Three of the four fundamental forces, are represented as locally gauge invariant quantum field theories (QFT). Excluding gravity, this applies to the electromagnetic as well as the weak and strong nuclear force.

Focussing on strongly interacting matter, this case fundamentally covers the interplay of *quarks* through the exchange of *gluons*. The corresponding QFT is called *quantum chromo-dynamics* (QCD), a Yang-Mills gauge theory based on the special unitary group SU(3). According to Noether's theorem this SU(3) symmetry leads to a conserved quantity, which in this case is the *colour charge*. There are three possible colours, that can be carried by the quarks and three corresponding anti-colours for anti-quarks. Due to its non-abelian nature QCD features gluon-gluon self-interactions, since they are not colour neutral [23, 24].

Furthermore, the relative strength of the strong force is characterised by the coupling constant α_s. This coupling constant is running, i.e. it does change its value depending on the momentum transfer q^2 in the interaction. The distinct feature of gluon self-interaction, the number of different colour charges and the number of *active* quarks[1] are the decisive factors for the trend of $\alpha_\mathrm{s}(q^2)$. In the case of strongly interacting matter described by QCD the coupling is strong, i.e. α_s has a large value relative to the coupling constants of the other forces, for small momentum transfers q^2. This corresponds to a large distance between bare colour charges and explains why quarks cannot exist as free particles in nature. In standard conditions they are always bound into colour-neutral composite particles like protons, pions or nuclear matter in general. This effect is referred to as *colour confinement*. Moreover, *chiral symmetry* is broken in this regime. Here, chiral symmetry

[1] Depending on the energy of the particles interacting, not all quark flavours might be contributing.

describes the invariance of QCD processes with respect to a certain symmetry group as presented in [23, 24].

On the other side the coupling strength decreases logarithmically with increasing momentum transfer. As a consequence, the quarks are less strongly bound for smaller distances of their bare colour charge. Thus quarks are quasi-free at a sufficiently large momentum transfer q^2 or energy density in general. This unique feature of QCD is known as *asymptotic freedom* [23, 25].

2.1.1 The quark-gluon plasma

As a consequence of the running strong coupling constant $\alpha_s(q^2)$, QCD calculations predict a phase transition from confined to deconfined nuclear matter above a critical temperature T_c. Apart from ultra-high temperatures, deconfined nuclear matter is also anticipated to exist at extreme matter densities. While ordinary nuclear matter can be described as a hadron gas, where quarks are bound in colour-neutral states, quarks and gluons become unbound at a sufficiently high energy density. This new state of matter is known as quark-gluon plasma (QGP). According to cosmological models it is the state of the universe which lasted for a few microseconds after the Big Bang [26, 27].

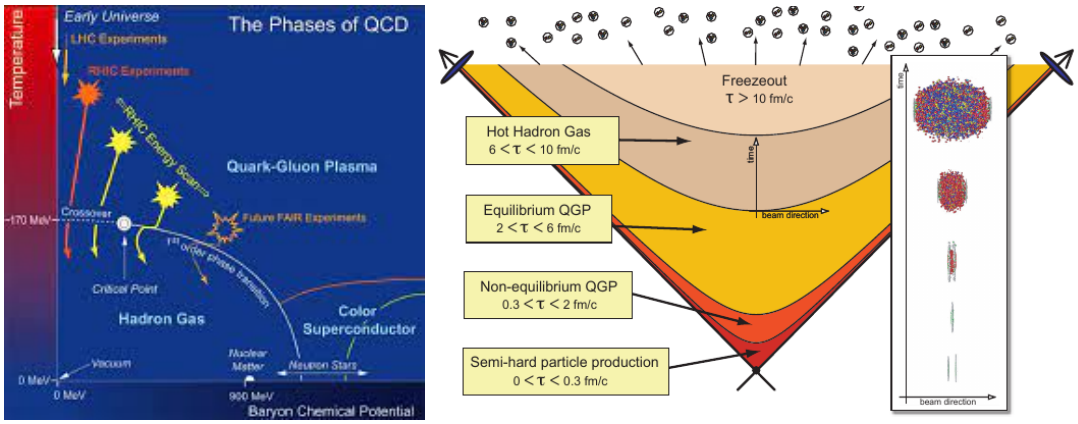

Figure 2.1 **(left)** Semi-qualitative illustration of the phase diagram of QCD matter. The two experimental control parameters, namely temperature (T) and baryochemical potential (μ_B), are represented by the vertical and horizontal coordinate axis, respectively. Furthermore, the phase transition from a hadron gas to a quark-gluon plasma is depicted by the white line. At vanishing μ_B a *smooth crossover* between these two phases is indicated. Experimentally accessible regimes are denoted in yellow and orange [28].
(right) Sketch depicting the space-time evolution of the quark-gluon plasma generated in high-energy heavy-ion collisions. The time τ passed after the collision and one spatial coordinate are represented by the vertical and horizontal coordinate axis, respectively. The overlay shows the corresponding evolution of two Lorentz contracted colliding nuclei in the laboratory frame [29].

Experimentally, a QGP can be produced by means of ultra-relativistic heavy-ion collisions, since it requires a certain system size to be generated. According to QCD calculations on a discrete lattice[2], the QGP formation happens at energy densities of at least[3] $1\,\mathrm{GeV\,fm^{-3}}$ [27]. In order to probe different phases of strongly interacting matter, i.e. exploring its phase diagram, the experimental control parameters *temperature* and *density* can be varied. A semi-qualitative representation of the QCD phase diagram is shown in figure 2.1 on the left. While the temperature is linked to the collision energy, the *baryochemical potential* μ_B reflects the density of the system.

[2] In this temperature regime perturbative solving methods for the QCD equations cannot be applied anymore.
[3] The energy density of ordinary nuclear matter in the ground state is $0.15\,\mathrm{GeV\,fm^{-3}}$ [27]

It is the thermodynamic work needed in order to hypothetically add one more baryon to the particle ensemble. It can be seen that in the case of the LHC at CERN very high temperatures at almost vanishing μ_{B} are achieved. In this regime, lattice QCD predictions, which are performed for $\mu_{\mathrm{B}} = 0$, can be compared with the measurements [23, 28, 27].

After being generated in a heavy-ion collision, the QGP evolves in space-time as depicted in figure 2.1 on the right. Its expansion is driven by a pressure gradient and causes the matter to cool down. It can be seen that before a QGP is formed, so-called *hard particle production* dominates. Within the passing time of the colliding nuclei parton-parton scattering occurs at sufficiently high energies such that heavy (charm c and bottom b) quark-antiquark pairs can be directly produced. For this reason, they can serve as a probe in order to investigate the properties of the QGP as described in section 2.1.2. After a short thermalisation time, a QGP in a local thermal equilibrium has developed. As such it can be described by linearised viscous hydrodynamics. Going below the critical temperature hadronisation of the medium sets in. The nature of the transition from a deconfined medium back to colour-neutral hadrons for vanishing μ_{B} is still subject of research. A *smooth* crossover phase, which is attributed to the chiral symmetry breaking and restoration when transitioning from QGP to hadron gas and vice versa, is indicated as shown on the left side of figure 2.1 [20, 29, 23].

After this so-called *chemical freezeout* the produced hadrons are still subject to scattering and are thus described as a *hot hadron gas*. After the scattering ceases due to further expansion and cooling, the momentum spectra of the generated particles is fixed and the hadrons freely stream to the detectors. This final step is referred to as *kinetic freezeout* [29].

2.1.2 Measurable signatures of the quark-gluon plasma

In order to identify and characterise the properties of the QGP, some experimental limits need to be considered. However, there are several legitimate proposals and strategies on how to measure the signatures of the QGP. Since the size of the QGP is only a few femtometres in diameter, is cannot be directly resolved by any detector. As such, only emerging particles after its transition to a *(hot) hadron gas* can be detected. Here, another difficulty is its short lifetime of only $5\,\mathrm{fm\,c^{-1}}$ to $10\,\mathrm{fm\,c^{-1}}$. For this reason, QGP probes have to be disentangled from hadronic background, which originates from processes after the hadronisation of the QGP. Furthermore, the signals of interest can be disturbed by final state interactions at later times [26].

Nowadays, a multitude of experimental observables to investigate the QGP have been identified and are used in present-day data analysis. Since this work is especially aimed at detector development, only a selection of these observables is presented. The following observables are considered to be of fundamental importance for the field of research or are especially relevant for the detector design choices and motivation presented in the following sections. For an extensive overview of experimentally measurable QGP signatures [27, 26] can be consulted.

Strangeness enhancement The energy threshold that needs to be surpassed in order to create a pair of strange quarks s-$\bar{s}$ is lower inside the QGP as compared to their production within the hadron gas [30]. Consequently, an enhancement of the overall stangeness content is observed in the presence of a QGP. Once produced, the strangeness content could be decreased by the weak interaction only. However, the time scale for these processes is much longer than the lifetime of the QGP. As a consequence, the produced strange quarks outlast the QGP and hence become constituents of strange mesons and baryons. In fact, an enhancement of these particles, especially of multi-strange baryons like Ξ^{+} and Ξ^{-}, is observed in experimental data when comparing Pb-Pb and p-p collisions [31, 26].

Quarkonium suppression The production yields of heavy quarks, i.e. charm c and bottom b quarks, play a major role in characterising the properties of the QGP. When they are generated as quark-antiquark pairs in initial parton-parton interactions, such as gluon fusion, they cannot exist as bound states $c\bar{c}$ and $b\bar{b}$ in the QGP as they *melt*. Here, the underlying process causing this is the colour equivalent to Debye screening[4] [27]. This effect depends on the binding energy of the considered system. Therefore, $J/\Psi(c\bar{c})$ disintegrate at temperatures slightly above the critical temperature T_{c}, while excited $c\bar{c}$ states basically immediately dissociate as soon as T_{c} is reached. Similar considerations apply to $b\bar{b}$ states. The yields of these particles thus are probes for the deconfinement within the QGP [27, 26]. Via models describing for example the (re)formation of the J/Ψ meson at the hadronisation phase, the freezeout temperature is accessible using these probes. Furthermore, these particles become probes of the nature of the phase boundary between deconfined and confined matter [27, 32].

Parton energy loss As already proposed by Bjorken in 1982, partons can lose energy by interacting with the QGP medium [33]. This energy loss can either be realised by exciting the medium itself or by emission of radiation. Consequently, final state particles in heavy-ion collisions are affected by this *medium effect*, while this is not the case for p-p collisions. The fundamental experimental observable describing this effect is the *nuclear modification factor* R_{AA}.

$$R_{\mathrm{AA}}(p_{\mathrm{T}}) = \frac{1}{N_{\mathrm{coll}}^{\mathrm{AA}}} \frac{\frac{d^2N^{\mathrm{AA}}}{dydp_{\mathrm{T}}}}{\frac{d^2N^{\mathrm{pp}}}{dydp_{\mathrm{T}}}} \tag{2.1}$$

As described by equation 2.1, the nuclear modification factor is the transverse momentum (p_{T}) spectrum of a charged particle in nucleus-nucleus (AA) collision normalised to the same quantity for proton-proton (pp) collisions at a comparable collision energy. As such N describes the particle yield, while y is the rapidity and p_{T} the particle's momentum projected to the transverse plane. N_{coll} describes the number of parton-parton collisions for the colliding nuclei. If the medium would have no effect, heavy-ion collisions could be described as a superposition of N_{coll} parton-parton interactions. This would yield $R_{\mathrm{AA}} = 1$. Given the existence of QGP, the experimental data shows that the nuclear modification factor is smaller than unity. In fact, it can be seen that the medium effect is less pronounced at high transverse momenta, while the low-p_{T} region is the more interesting case [27, 5].

Collective flow In non-central collisions of two Lorentz contracted heavy ions, the overlap region can be approximated as an elliptic shape in the transverse plane perpendicular to the beam pipe. As a consequence, initial gradients of the energy density and pressure of the medium arise. These lead to an anisotropic angular distribution of the produced hadrons, which can be observed in their corresponding momentum spectra with respect to the reaction plane. This observable is referred to as (anisotropic) *collective flow*. Since flow is generally described by a Fourier expansion, *elliptic flow* is characterised by the second Fourier coefficient v_2. Due to their nature, the Fourier coefficients are momentum p_{T} and rapidity y dependent. Since the particle momentum anisotropy originates from the initial collision geometry, flow measurements are sensitive to the early phase of QGP formation [27, 34].

Direct photons Photons produced by the QGP as thermal radiation are called *direct photons*. As such, they provide experimental access to the initial QGP temperature and its space-time

[4] Dampening of electrical fields due to surrounding mobile charge carriers.

evolution. A difficulty of the measurement of direct photons is the large background due to photons being generated in decay processes of the generally produced hadrons. Since photons are detected via the pair production process, this measurement requires a very efficient identification of the resulting electron-positron pairs. Due to the energy range of the direct photons, this measurement is referred to as *low-momentum di-electron* measurement [26, 20].

2.2 The ALICE experiment

With the upgrade of its Inner Tracking System (ITS), the ALICE experiment, one of the four main experiments located at CERN's Large Hadron Collider (LHC), is one of the first experiments to install a large-scale tracking detector based on MAPS technology [35, 6]. The motivation and physics requirements of this upgrade as well as the resulting design of the new tracking detector ITS2 are described in the dedicated section 2.2.1.

ALICE, standing for A Large Ion Collider Experiment, is especially dedicated to investigating heavy-ion collisions at high centre of mass energies. As such, the ALICE physics program is mainly targeted at investigating and understanding the properties of strongly interacting matter at extreme energy densities when a QGP is formed. Since the formation of the QGP requires a sufficiently large interaction volume, ALICE records collisions of lead ions (Pb-Pb) being delivered at centre of mass energies per nucleon pair of up to $\sqrt{s_{\mathrm{NN}}} = 5.5\,\mathrm{TeV}$ by the LHC. Additionally, proton-lead (Pb-p) and proton-proton (pp) collisions are taken to complement the physics program of ALICE [36].

As described in section 2.1.2, investigating the nature of the QGP involves the measurement of collective particle properties. As such, the ALICE detector is designed and optimised in order to provide outstanding particle identification (PID) capabilities at large particle multiplicities. Furthermore, as less as possible preselection of events is done on a hardware level during data taking. Therefore, only a *minimum-bias* trigger is applied. Since especially low-momentum particles are of major importance for the characterisation of the QGP, the ALICE main detectors are installed within a large solenoid magnet nominally providing a homogeneous and moderate magnetic field of $0.5\,\mathrm{T}$ [36]. The characteristic red yoke of the magnet and the full ALICE detectors are schematically illustrated in figure 2.2.

Starting from the core, there is the Inner Tracking System ITS (blue), which is currently replaced by the new ITS2. The ITS is made of 6 concentrical layers of silicon detectors, which feature different detector technologies. While the innermost two layers are made from hybrid silicon pixel detectors (SPD), the middle two layers consist of silicon micro-strip detectors (SSD). For the outermost two layers, where the requirements on granularity are the least, silicon drift detectors (SDD) are installed. This old design of the ITS has reached some limitations in terms of performance and rate capability, which is why it is entirely replaced and not only parts of it are upgraded.

Another tracking detector is the large time projection chamber (TPC), which plays a major role for the ALICE experiment. This huge gas detector (blue-grey) provides the means to, in principle, perform a standalone PID. Further detectors such as the transition radiation detector (TRD) shown in green and the time of flight (TOF) detector provide additional or even redundant information used for PID. Hence, they help to resolve ambiguities in the TPC. In the outermost detector layers different types of calorimeters (orange, purple) are installed in order to measure particle or photon energies. Besides all these so-called *central barrel* detectors, there is also the ALICE Muon Spectrometer arm featuring its own dipole magnet and several tracking chambers.

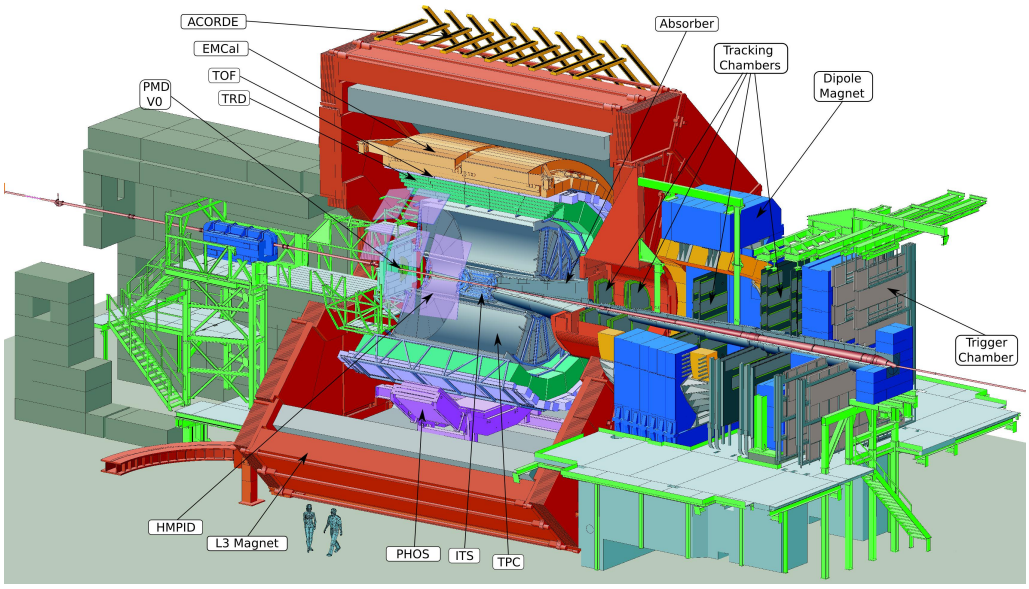

Figure 2.2 Schematic of the ALICE detector system. The main detectors are labelled with their corresponding names. Their acronyms can be also found in the list of abbreviations in section A.1. The most important detector for this work is the Inner Tracking System (ITS) illustrated in blue and located closest to the beam pipe around interaction point. All central detectors are installed inside the large L3 solenoid magnet shown in red [37].

With upgrades and the resulting increase in the performance of the LHC, also some of the ALICE detectors have to be improved or even completely replaced. After the currently ongoing Long Shutdown 2 (LS2), the LHC luminosity is increased, thus leading to Pb-Pb interaction rates of up to $50\,\mathrm{kHz}$ [6]. In order to exploit the higher available statistics, the readout rate of all the detectors must match the higher interaction rate. Besides the ITS, also the readout detectors of the TPC are replaced for this purpose. A brief overview of these upgrades can be found in [38]. Additionally, several other upgrades were envisaged and are currently performed on different parts of the ALICE detector.

2.2.1 Upgrade of the Inner Tracking System (ITS2)

The upgrade plans for the ALICE detector during the second long shutdown period (LS2) include the replacement of the old ITS by a new one, which is referred to as ITS2. This upgrade is mainly driven by the upgrade of the LHC in the same period. After the LS2 the LHC delivers Pb-Pb collisions with a higher instantaneous luminosity of up to $\mathscr{L} \approx 6 \times 10^{27}\,\mathrm{cm}^{-2}\,\mathrm{s}^{-1}$. This leads to an increased heavy-ion interaction rate of up to $50\,\mathrm{kHz}$, corresponding to an augmentation of the available minimum-bias dataset by a factor of 100. With the upgraded detectors, especially including the ITS2, the readout rate is significantly improved and ALICE will be able to record $10\,\mathrm{nb}^{-1}$ of Pb-Pb collisions[5]. Thus, the statistical precision for a multitude of physics observables is significantly improved as compared to the previous case before LS2 [38, 6].

As already discussed in section 2.1.2, heavy flavour measurements play a major role as probes of the QGP. Especially the nuclear modification factor $R_{\mathrm{AA}}(p_{\mathrm{T}})$ for charmed D mesons and B mesons containing a bottom quark benefit from optimised tracking capabilities and readout rate. Furthermore, an extended measurable momentum range towards lower particle momenta not only improves these measurements, but also the previously discussed elliptic flow measurements.

[5] This corresponds to 10^{11} events.

In addition to that, a better low-momentum resolution provides access to a precise measurement of low-mass di-leptons. For example direct photons from thermal radiation of the QGP can be detected via the conversion method, i.e. as electron-positron pairs resulting from pair production processes in a (conversion) target [6].

The aforementioned improvements of the physics observables are the driving factor and the motivation of the ITS2 upgrade plans and detector design. Featuring a total active area of $10\,\mathrm{m}^2$, the ITS2 is based on MAPS technology [38]. Specifically for the purpose of this upgrade a new MAPS called ALICE Pixel Detector (ALPIDE) has been developed. The ALPIDE chip features more than 500k pixel, which are roughly $30\,\mu\mathrm{m} \times 30\,\mu\mathrm{m}$ large. Featuring a position resolution of about $5\,\mu\mathrm{m}$, the application of the ALPIDE chip significantly improves the tracking resolution. Its design, working principle and performance studies are extensively described in the following chapter 3.

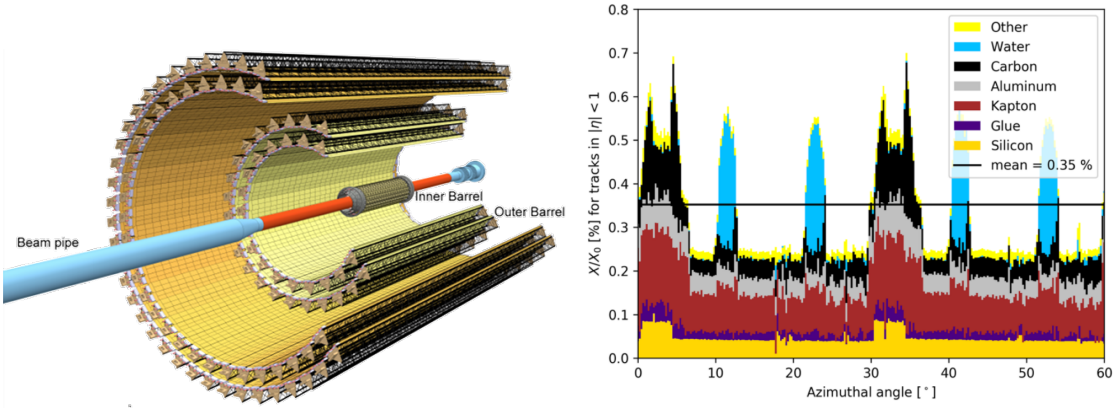

Figure 2.3 **(left)** Schematic of the upgraded ALICE Inner Tracking system ITS2. Staves holding the ALPIDE sensors are mounted in 7 concentric, cylindrical layers around the beam pipe. The four outer layers are referred to as *Outer Barrel* (OB), while the three inner layers are labelled as *Inner Barrel* (IB) [6].
(right) Material budget distribution of one IB layer of the ITS2. The material budget is given as a fraction of the radiation length X_0 for a selected range of track angles. Position information is represented by the horizontal axis, which describes the azimuthal angle. The contributions of different materials and thus detector parts are represented by different colours. The mean material budget of one ITS2 IB layer is $0.35\,\% \frac{\mathrm{X}}{\mathrm{X}_0}$ [38].

The final detector design of the ITS2 is shown in figure 2.3 on the left side. It can be seen that this new vertex detector for ALICE consists of 7 concentrical barrel-like tracking layers. They are divided into an Outer Barrel (OB) comprising the 4 outer layers and an Inner Barrel (IB) featuring the remaining most inner ones . Since the ALICE upgrade plan also involves a new thinner beam pipe, it is possible to install the first IB layer closer to the interaction point as compared to the old ITS[6]. In fact, the radial distances between the ITS2 layers and the collision point range from $2.3\,\mathrm{cm}$ to $40\,\mathrm{cm}$ [38, 6]. This already improves the (low-)momentum resolution and the tracking performance especially regarding the identification of the *impact parameter*, which is basically the position of the initial collision point.

The cylindrical layers are build from flat *staves* including several ALPIDE chips (yellow). In addition, they provide a mechanical support structure (black), a water cooling infrastructure and electronics to power, readout and interconnect the single ALPIDE chips. Not only the number of ALPIDE sensors per stave differs for OB and IB, but also the sensor thickness. As such an IB stave

[6] Innermost layer of the old ITS is installed at $3.9\,\mathrm{cm}$ radial distance to the interaction point [6].

is equipped with 9 ALPIDE chips each of which is thinned down to $50\,\mu\mathrm{m}$ thickness, while the larger OB staves comprise 14 sensors of thickness $100\,\mu\mathrm{m}$ [38].

Besides basing the entire new vertex detector on pixelated CMOS MAPS instead of implementing three different silicon detector technologies as it used to be the case for the predecessor of ITS2, also the material budget is tremendously reduced. Since more material along its trajectory significantly increases the probability that a particle scatters, a reduction of the material leads to an improved momentum resolution especially in the low-momentum regime. The material budget distribution of an IB inner layer is shown in figure 2.3 on the right. Over a range of azimuth angles φ, where $\varphi = 0$ corresponds to the horizontal plane, the material budget of two staves is given as a fraction of the corresponding radiation length X_0[7]. This applies only considering tracks of a certain angle with respect to the beam pipe direction, which can be expressed as *pseudorapidity* η.

Different materials contribute differently to the overall material budget and are therefore encoded by different colours. The impact of the water cooling pipes are immediately visible. The other two regions around $\varphi = 0$ and $\varphi = 30$ showing an increased material budget are an effect of slightly overlapping neighbouring staves due to their installation in a cylindrical detection layer. Overall, an average value of $0.35\,\% \frac{\mathrm{X}}{\mathrm{X}_0}$ is achieved for one IB layer of the ITS2, while an OB layer features a material budget of $1\,\% \frac{\mathrm{X}}{\mathrm{X}_0}$ [38].

In summary, the limited readout rate of $1\,\mathrm{kHz}$ for the old ITS is improved to match the increased interaction rate after LS2. In fact, the target value of $50\,\mathrm{kHz}$ is even outmatched by a factor of two, given that the ITS2 can be operated at a readout rate of up to $100\,\mathrm{kHz}$. Furthermore, the enhanced tracking and momentum resolution of the ITS2 with respect to its predecessor have an important beneficial impact on the physics measurements of the ALICE experiment as described in the sections 2.2 and 2.1.2. A detailed overview of the ITS2 upgrade with all of its aspects is given in [6].

2.2.2 Future upgrade of the ITS featuring curved silicon pixel sensors (ITS3)

Until their application in the ITS2, MAPS have undergone a long research and development phase, resulting in fundamental improvements of their performance. Especially their radiation tolerance, which is a key requirement for their application in a high-energy particle or nuclear physics experiment, has significantly increased over the last decades. Providing a very good signal-to-noise ratio and position resolution, together with an ultra-low material budget, they will probably be the key technology for future tracking detector upgrades or even new detector concepts as presented in the following section 2.3.

A very recent innovation in the production of silicon imaging sensors called *stitching* paves the way for a new generation of MAPS. Usually the chip size is limited by the reticle[8] size used in the photo-lithographic production process. With stitching, wafer-scale[9] sensors can be produced, by positioning the reticle with such precision that the same repetitive pattern can be produced on the wafer (silicon substrate) next to each other. Retaining the electrical functionality at the interface of two of these patterns, a functional macro-chip can be realised [40].

Linked to the stitching and the comercially available wafer sizes, the so-called $65\,\mathrm{nm}$ production node is explored, which describes the minimum possible feature size, i.e. usually a transistor. By having smaller feature sizes, the pixel size of such a sensor could be further decreased leading to

[7] Average distance after which a (highly energetic) electron traversing the material has reduced its initial energy E_0 to $1/e \cdot E_0$ by Bremsstrahlung.
[8] Mask to project the circuit layout on the silicon substrate (wafer), where this structure is then produced by etching.
[9] $300\,\mathrm{mm}$ in diameter for the Tower Semiconductor $65\,\mathrm{nm}$ CMOS Image Sensor process [39].

an improved position resolution. Furthermore, more transistors per area are realisable such that the complexity of the integrated in-pixel circuitry could potentially be increased.

With these perspectives a further upgrade of the ALICE ITS2 is foreseen during the future third long shutdown period (LS3) of the LHC. This upgrade is mainly aimed at further reducing the material budget and thus improving the tracking precision and efficiency. As such, especially the measurement of low-momentum hadrons containing a heavy-flavour quark (c,b) benefits significantly from the planned upgrade. Furthermore, the precision and momentum range of the low-mass di-electrons measurement in heavy-ion collisions is significantly improved. In order to achieve these goals, a new vertex detector iteration called ITS3 is proposed. It basically is the ITS2 with the three innermost tracking layers (IB) being replaced by three new ones made of truly cylindrical, large-area and ultra-thin MAPS. By *truly cylindrical* it is meant that the MAPS chip is thinned down to a target thickness of below $50\,\mu\mathrm{m}$ and is then bent to resemble the barrel-shaped detector layers [38, 40].

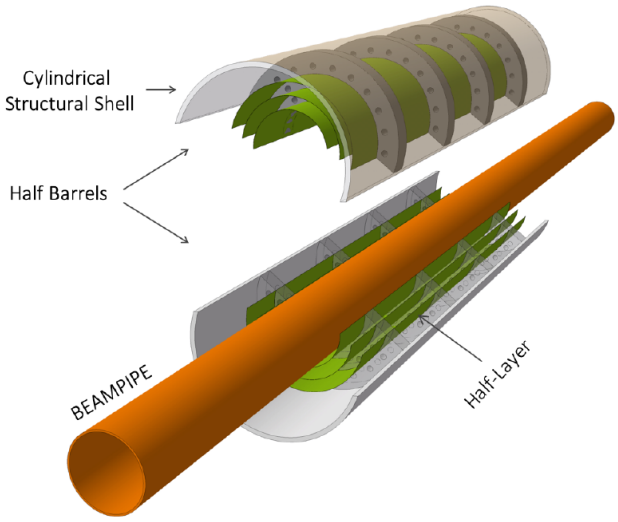

Figure 2.4 Schematic illustration of both half-barrels planned to be installed around the beam pipe within the ITS3 upgrade project. Each sensitive layer (green) consists of a single large-area MAPS that is bent to a truly (half-) cylindrical shape. As only the inner barrel of the ITS2 gets replaced in the ITS3 upgrade, this results in 3 concentrical, truly cylindrical detection layers. To mechanically hold these bent sensors in place, they are mounted within a cylindrical structural shell and open-cell carbon foam spacers ensure the constant distance in between the layers [40].

The envisaged detector layout of the ITS3 is schematically shown in figure 2.4. The three cylindrical tracking (green) layers are realised in two *Half Barrels*, which are then joined when they are mounted around the beam pipe (orange). Exploiting the mechanical sturdiness of bent silicon sensors, almost no support structure is needed. As such, the sensors, each making up one Half Barrel layer, are installed within a cylindrical structural shell made of carbon fibre reinforced plastic (CFRP). Open cell carbon foam structures act as spacers (grey) in between the layers, which feature radial distances to the interaction point of $18\,\mathrm{mm}$, $24\,\mathrm{mm}$ and $30\,\mathrm{mm}$, respectively. With the even closer distance to the interaction point, the resolution of the impact parameter improves by a factor of 1.4 with respect to ITS2 regarding particles featuring a transverse momentum $1\,\mathrm{GeV\,c^{-1}}$ [40].

In figure 2.3 on the right it can be seen that the material budget of an ITS2 layer is highly irregular. It is also visible that the contribution of the bare silicon from the actual sensors is only a small fraction of the overall material budget. Featuring curved silicon sensors, the material budget

for an ITS3 inner layer is reduced to only about $0.05\,\%\,\frac{\mathrm{X}}{\mathrm{X}_0}$. This corresponds to a reduction of the material budget by a factor 3 within the first $4\,\mathrm{cm}$ radial distance to the interaction point [38]. Additionally, the material budget is more homogeneously distributed as compared to ITS2.

This is achieved by removing the water cooling. Instead, the sensor is optimised with respect to power consumption such that the active area can be cooled by an air flow. The readout, which consumes the most power and thus generates the most heat, is located in the periphery at both ends of the barrel (not shown in figure 2.4). There, traditional cooling methods can be applied.

With this novel curved vertex detector the ITS3 upgrade is supposed to improve the pointing resolution of the ALICE Inner Tracking System by a factor of 2 with respect to the ITS2. Furthermore, systematic uncertainties are reduced due to the almost homogeneous distribution of the detector material. As a future upgrade project, the plans for ITS3 are summarised in the corresponding letter of intent [40].

2.3 A future all-silicon heavy-ion experiment

There are already plans for a follow-up experiment after the runtime of the ALICE experiment ends and its detector might be fully disassembled. As such, a next-generation heavy-ion experiment is proposed to be installed at LHC's interaction point 2, i.e. the current location of the ALICE detector. This future experiment aims at continuing the journey of exploring the nature of strongly interacting nuclear matter at extreme energy densities. This is achieved by further studying and probing the properties of the QGP. For this reason, especially high-statistics measurements on heavy flavour hadrons are envisaged as one focus of the proposed new experiment, which is currently referred to as ALICE3. Additionally, it is foreseen to measure direct photons and low-momentum hadrons with an unprecedented precision. Here, ALICE3 aims at accessing a particle momentum region down to a few tens of $\mathrm{MeV\,c^{-1}}$ [41].

In order to achieve these physics goals by recording proton-proton and nuclei collisions, a tracking detector is proposed, which is entirely based on silicon detectors. More precisely, several types of CMOS MAPS are supposed to be applied, leading to a compact ultra-low material budget for this detector. A schematic view of a possible detector layout is shown in figure 2.5. In general, the detector is planned as a central barrel around the beam pipe with two end-caps, i.e. one on each side. The full detector setup will be placed inside a solenoid magnet (not visible in the figure) providing a moderate magnetic field of the order of $0.5\,\mathrm{T}$ [41]. As such a high tracking efficiency for particles featuring a very low transverse momentum p_T can be achieved, while maintaining a good performance for high-p_T particles.

Starting from the inside detector layers to the outer ones, first there is the Inner Tracker (IT) shown in blue. Being inspired by the development of the ALPIDE chip and regarding the research efforts already on the way for the ITS3 upgrade project, the IT will be based on three layers of truly cylindrical, ultra-thin and large-area CMOS MAPS. For the highest possible position resolution, pixels of the size of $10\,\mu\mathrm{m} \times 10\,\mu\mathrm{m}$ are considered. Four end-discs provide forward tracking capabilities within the IT.

The Outer Tracker (OT) illustrated as green and yellow layers features the same basic technology as the IT. It consists of 7 concentric barrel layers and 6 end-cap discs. Since there is a lower requirement on granularity and in order to reduce power consumption and thus heat generation, the OT pixels are supposed to have a larger size of $30\,\mu\mathrm{m} \times 30\,\mu\mathrm{m}$. Also the material budget per detector layer is increased from $0.05\,\%\,\frac{\mathrm{X}}{\mathrm{X}_0}$ for the IT to $0.5\,\%\,\frac{\mathrm{X}}{\mathrm{X}_0}$.

For providing additional information for particle identification, a Time Of Flight detector layer shown in orange is introduced. One possibility is to base it on Low-Gain Avalanche Diodes (LGAD),

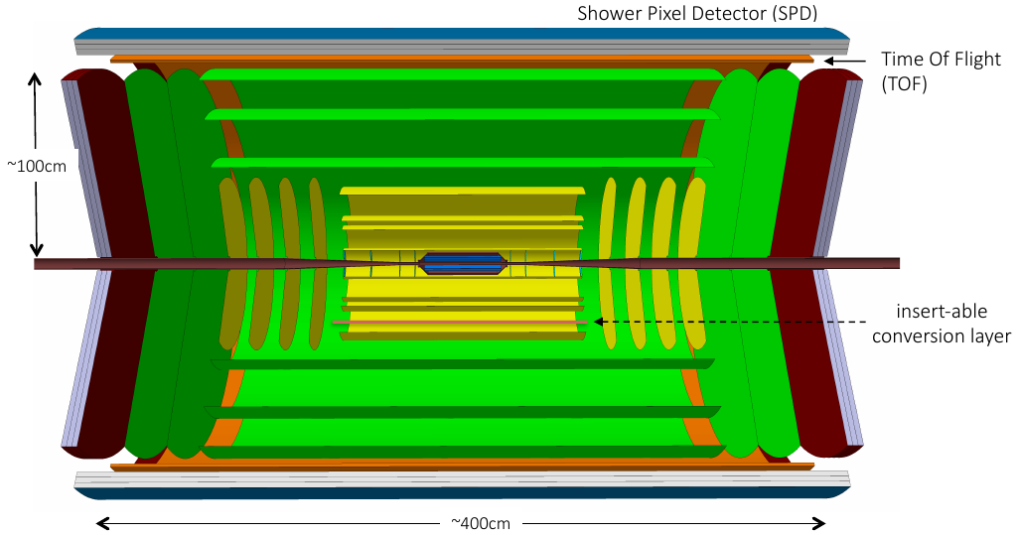

Figure 2.5 Schematic of a possible new-generation multipurpose detector at the LHC for a follow-up heavy-ion experiment after the end of the current ALICE experiment. This ALICE 3 detector is entirely based on silicon CMOS technology and features an Inner Tracker (inner blue) possibly placed inside the beam pipe and an Outer Tracker (yellow, green) both based on wafer-scale ultra-thin MAPS. Additionally, there is a Time Of Flight detector (orange), a Shower Pixel Detector (outer blue) and end-cap discs for tracking (yellow, green) as well as one SPD disc (red) [41].

since it is supposed to provide a timing resolution of around 20 ps. However, other technologies are also discussed. In order to provide redundant information and especially complement the TOF measurement for particles with higher momentum, there is the Shower Pixel Detector (SPD). It is realised as alternating layers of high-density passive material and high-granularity pixel sensors as active part. As such electrons, positrons and photons can be identified, since they will trigger an electromagnetic shower.

With this proposed multi-purpose detector, significant contributions to the field of QCD matter and its phases are expected. Due to the extremely light-weight detector design new experimental regions and measurements will become possible, while the precision of known measurements can be tremendously improved. One of the possible objectives is to find experimental evidence for the restoration of chiral symmetry when transitioning from the QGP to a hadron gas. Furthermore, a precision measurement concerning the QGP temperature is proposed. For a more detailed overview of the plans, possibilities and motivation for the ALICE3 experiment [41] can be consulted.

3 The ALPIDE chip

The development of a silicon pixel detector based on MAPS technology for the ALICE ITS2, which is described in section 2.2.1, started in 2012 with studies on basic charge collection properties of different collection diode geometries. For this purpose several small-scale prototypes were tested. This first approach featured chip architectures implementing a row-by-row readout and explored the possibility to have an analog pixel output. In parallel to them, a different approach for a MAPS was followed with the *ALPIDE design*, where ALPIDE stands for *ALICE Pixel Detector*. This design especially features a *binary readout*, which means that there is only the information if a pixel is hit or not available. In particular, analog information like time over threshold or amount of collected charge are not accessible during readout.

As opposed to other investigated chip architectures, which rely on a so-called *rolling shutter*, the ALPIDE architecture allows for a readout in a *global shutter* fashion. Here, the name shutter, refers to the *shutter signal*, which in general stops the in-pixel signal integration and initiates the readout when it is deployed. For a rolling shutter architecture, the shutter signal is propagated from row to row. During the readout of one row, the hit information is read subsequently for each pixel. Consequently, the readout time for the full pixel matrix scales with the number of pixels per row and the frequency of the shutter signal, i.e. the time required for cycling through all rows. As the name global shutter already suggests, all rows from the matrix can be read out simultaneously in such an architecture. In the case of ALPIDE, but also in general, the shutter signal can be controlled by an external trigger signal[1] [20].

A second key component of the ALPIDE architecture is the *in-pixel circuitry*. It allows for signal amplification, shaping and discrimination already on the pixel level. For this reason, an already zero-suppressed digital signal, namely the address of the hit pixel, needs to be sent to the chip periphery for further processing and readout. As a consequence, this approach is very power efficient as compared to other chip architectures, where the in-pixel circuitry only features amplifiers. For them, the analog signal needs to be driven to the chip periphery for discrimination and zero-suppression. Furthermore, no analog clock signal needs to be distributed over the entire pixel matrix in the case of a binary readout, since no time over threshold or other analog information is accessible. As such, ALPIDE is fully optimised in terms of power consumption. However, this is only possible at the expense of timing resolution [20].

Besides other advantages, the shorter readout time [2] and lower power consumption, as compared to prototypes featuring the traditional rolling shutter approach, qualified the ALPIDE architecture to be the basis of the chip development for the ITS2 project. With the so-called pALPIDE-1, standing for prototype-ALPIDE, a first full scale sensor was ready for testing in 2014. Based on a multitude of performance tests, particularly including testbeam campaigns, several optimisations of the in-pixel circuitry and thus new or improved functionalities were implemented in the subsequent chip design iterations pALPIDE-2 and pALIPDE-3. All this research effort lead to the

[1] In principle ALPIDE also allows for a continuous readout, where the shutter is only closed when moving to the next hit buffers

[2] Due to the charge diffusion component in the signal collection, still MAPS and especially ALPIDE have much worse timing resolution as compared to other detectors.

final ALPIDE chip in 2016. A detailed overview over the tested prototypes and some results of the performed tests are presented in [20, 5].

In the following sections the ALPIDE architecture, working principle and the functionality of the in-pixel and chip circuitry are described and illustrated. Furthermore, the performance of the final ALPIDE chip is presented serving as reference for comparison with bent versions of the chip.

3.1 Chip architecture and principle of operation

As shown in figure 3.1 on the left, the ALPIDE chip measures $30\,\mathrm{mm}$ in width (column direction) and $15\,\mathrm{mm}$ in height (row direction). Furthermore, the chip is thinned down to $50\,\mu\mathrm{m}$ thickness. It features 1024×512 pixels each with dimensions of $29.24\,\mu\mathrm{m} \times 26.88\,\mu\mathrm{m}$. The entire pixel matrix is organised in *double columns* as it can be seen in figure 3.1 on the right. Consequently, each double column consists of 1024 pixels. The readout of these pixels is done with a *priority encoder* located in the central part of each double column. For each pixel an Address-Encoder Reset-Decoder (AERD) circuit propagates the address of a hit pixel to the chip periphery, where this information is joined with signals from other double columns. Here, 16 neighbouring double columns form one readout region for a total of 32 regions on the entire chip. The data of each region is joined via a data multiplexer to provide one common data stream as chip output. In addition, the chip periphery also hosts the analog digital-to-analog converters (DACs) used to set and control the working point of each pixel as addressed in section 3.2 [42].

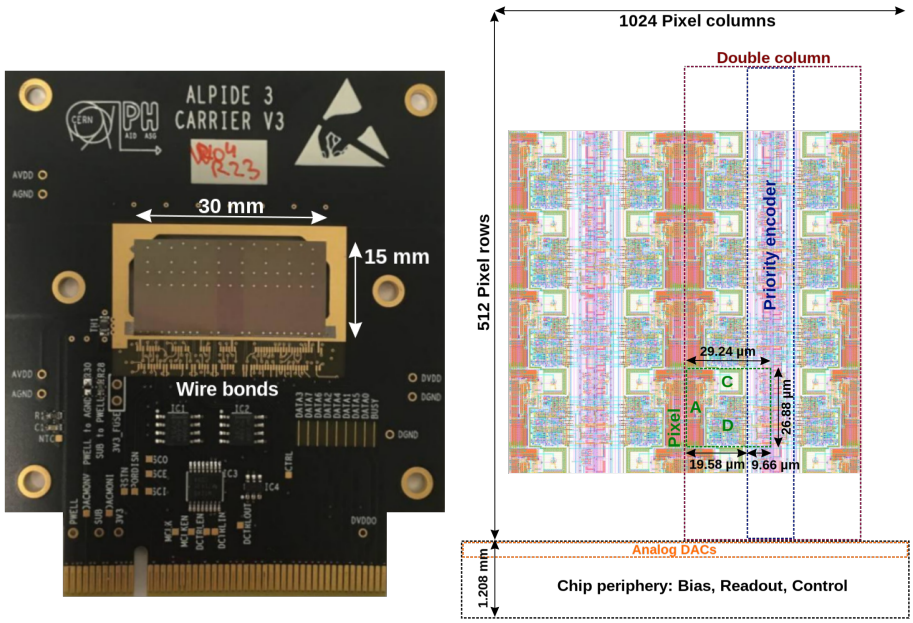

Figure 3.1 **(left)** Image of a state-of-the-art ALPIDE chip glued and wire bonded to a carrier board. The visible spots on the sensor surface are bonding pads of which some are not connected and only serve monitoring purposes.
(right) Schematic illustration of the ALPIDE chip architecture on top of a closeup showing the pixel matrix circuitry. Pixels are organised in double columns with a priority encoder for readout in the middle. The single pixel layout is highlighted in green with the locations of the collection diode (C), the analog front-end (A) and the digital pixel section (D). At the bottom there is the chip periphery containing the analog DACs and a mostly digital section. Adapted from [5] and [42].

The major goal and motivation of the ALPIDE architecture is to put as much functionality in a pixel as needed in order to optimise the power consumption of the chip. As a consequence, each ALPIDE pixel features rather complex electrical circuits to allow for signal amplification, shaping and discrimination. Furthermore, *zero-suppression* is already achieved on the pixel level, meaning that not-hit pixels do not trigger any activity in the readout circuits. This leads to a very low power consumption of the entire chip. As an example a single pixel uses about $40\,\mathrm{nW}$, while the entire matrix power density is generally below $40\,\mathrm{mW\,cm^{-2}}$ [35]. In addition to the signal processing, the ALPIDE architecture also allows to store up to three hits in a multi event buffer (MEB) on the pixel until the buffer is read out and flushed.

To achieve all mentioned requirements and functionalities, the ALPIDE chip is produced using the commercially established $180\,\mathrm{nm}$ CMOS Image Sensor process by *Tower Semiconductor*, formerly known as *TowerJazz*. As the name suggests this process allows for a high-density of electrical components, such as transistors, due to the small feature size of $180\,\mathrm{nm}$. A thickness of $3\,\mathrm{nm}$ metal oxide for the gate insulation layer provides sufficient radiation hardness[3] [20]. Additionally, there is the possibility of having up to six metal layers to interconnect the semiconducting components in order to build electrical circuits [39]. As illustrated in figure 1.5 the production process implements a deep p-well, such that all transistor n-wells are shielded from the active volume, i.e. the epitaxial layer. Hence, a full CMOS circuitry can be built on the chip not interfering with the charge collection of the collection diode. As previously mentioned, the chip can be read out in a global shutter mode reducing the readout time as compared to rolling shutter approaches [43].

The ALPIDE chip is manufactured on a p-type silicon wafer (substrate) and features a high resistivity epitaxial layer of $25\,\mathrm{\mu m}$ thickness as it can be seen in figure 1.1 on the right. The resistivity ρ being generally larger than $1\,\mathrm{k\Omega\,cm}$ is beneficial for the depletion of the epitaxial layer at the collection diode interface. Furthermore, the collection diode can be reverse-biased, which further increases the depletion region. This significantly increases the charge collection time due to an extended drift region [43]. Also the effective pixel capacitance C is decreased, which in turn leads to an improved signal-to-noise ratio according to $U_{\mathrm{signal}} = Q_{\mathrm{collected}}/C$. Considering this relation, an as low as possible pixel capacitance needs to be achieved in order to optimise the signal-to-noise ratio for the sensor. For this purpose, ALPIDE features a uniquely small collection diode of about $2\,\mathrm{\mu m}$ in diameter leading to an extremely low pixel capacitance in the order of several femtofarad. In turn, the signal-to-noise ratio is increased tremendously.

When a charged particle traverses the sensor in the active area, free charge carriers are produced in the epitaxial layer in the form of electron-hole pairs as described in the section 1.4. After this charge is collected by the collection diode, the resulting electrical signal is processed inside the pixel and therefore passes several instances. In the case of ALPIDE three main pixel regions can be identified. As denoted in figure 3.1 on the right, there is the collection diode (C) from which the signal is propagated to the analog in-pixel electronics (A) and then is finally passed on to the digital pixel area, where the *hit* is stored until readout. These three parts are schematically illustrated in figure 3.2 in the middle. A detailed explanation of the analog and digital *front-end electronics* is given in the following sections.

3.2 Analog in-pixel front-end circuitry

The general signal flow through an ALPIDE pixel is depicted in figure 3.2 at the bottom. It starts on the left with the charge collection at the collection diode D1. As a consequence the nominal

[3] Total ionising dose (TID)

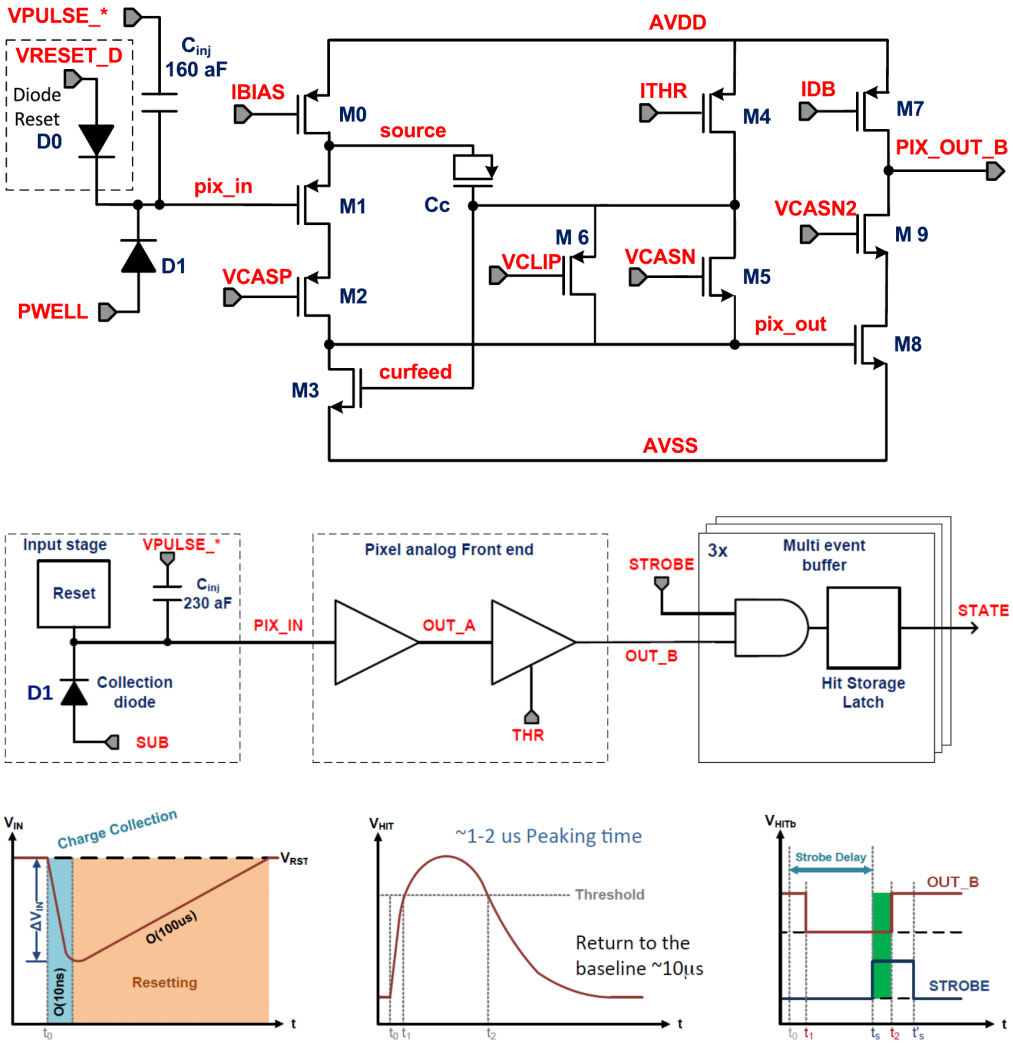

Figure 3.2 **(top)** Simplified ALPIDE in-pixel circuitry for shaping and discrimination of the signal. The input stage with the reset circuit is also shown. Transistors are labelled with M, while their external gate input signal is denoted by a grey arrow. All input and output nodes show the name of the corresponding DAC or analog signal [5].
(middle) Sketch of the electrical circuitry implemented in each pixel of the ALPIDE chip. There are three main stages: input (left), analog signal processing, such as shaping and discrimination (middle) and digital signal processing and storage (right) [35].
(bottom) Schematic illustration of the signal after several in-pixel instances. First the signal is shown at the input node to the shaper and discriminator circuit (left). The analog signal after shaping and before discrimination is shown in the middle. Finally, there is the discriminated signal in coincidence with a STROBE signal (right) [35].

voltage at the input node drops by ΔV_{IN}. The time of charge collection is of the order of 10 ns. While the signal is propagated to the pixel analog front-end via `PIX_IN` as schematically shown in figure 3.2 in the middle, the input node is constantly reset to its nominal voltage by a *reset circuit*. Figure 3.2 at the top shows a detailed view of the pixel input stage including the reset circuit with diode D0 and the input for VRESET_D, which defines the nominal voltage at the input node. While the charge collection is very fast, the resetting process takes around 100 µs.

Furthermore, the transistor network performing signal shaping and discrimination is shown in the same figure. The voltage drop at `pix_in`, which is connected to the gate of transistor M1, causes an increased current through M1. Being implemented as a so-called *source follower* the

source signal therefore follows the pixel input. In addition the source signal is also coupled to curfeed, which decreases the current through transistor M3. As a net effect the voltage at pix_out increases by a couple of $100\,\mathrm{mV}$ especially depending on the settings of ITHR and VCASN at M4 and M5 respectively.

For signal shaping depending on the bias voltage applied to the pixel VCLIP is set. The lower VCLIP, the sooner clipping of the signal sets in. This means that the tail of the signal is cut, by forcing it to $0\,\mathrm{V}$. The nominal values are 0 DAC for no back-bias and 60 DAC for a nominal back-bias voltage of $V_{\mathrm{BB}} = -3\,\mathrm{V}$. The resulting signal at pix_out can be seen in the middle panel at the bottom of figure 3.2. The circuit is tuned such that the peaking time of the shaped signal is of the order of a few microseconds, while the restoration of the baseline takes about $10\,\mu\mathrm{s}$ [5, 20].

Having now a voltage increase at pix_out the current through transistor M8 increases. If the input signal is sufficiently large to overcome the current setting of transistor M7, which is regulated by IDB, M8 drives the analog output node PIX_OUT_B to zero. Hence, an *active-low* discriminated signal has been generated from the analog input of the pixel at pix_in. It is illustrated in figure 3.2 at the bottom right as OUT_B. This signal can now be fed to the digital in-pixel electronics for storage and readout as depicted in figure 3.2 in the middle right.

As it is visible now the in-pixel threshold of an ALPIDE pixel can be set via the main parameters IDB, ITHR and VCASN, which in turn are controlled by the according DAC values with the same name. For a nominal operation of the chip VCASN2 is always set to a value corresponding to VCASN + 12. Augmenting IDB or ITHR will increase the threshold value, while an increased VCASN leads to a decreased threshold. The optimal working point of the pixel is found to be at a threshold of 100 electrons.

The threshold value and the response of the analog pixel front-end electronics can be tested by injecting a charge via the pulsing capacitor C_{inj}. The amount of charge injected depends on the input voltage VPULSE_* and is controlled by the digital part of the chip electronics as it is described in the following section.

3.3 Digital in-pixel front-end circuitry

Taking the discriminated output signal PIX_OUT_B as input the digital pixel part mainly serves the purpose of storing the detected signal until it is read out by the *priority encoder*. The implemented logic that allows for this task is shown in figure 3.3.

Since the ALPIDE pixel offers three buffers to store a hit for readout, the according register can be selected via the MEMSEL_B (memory selection) signal. These buffers are needed in order to account for event pileup caused by large particle rates in combination with the slow timing for the ALPIDE chip. Each buffer is made of a set-reset latch representing the binary hit-no-hit readout of the ALPIDE chip. If selected, the according *hit register* is set by the PIX_OUT_B signal only in the case a trigger in the form of the STROBE_B signal is present at the same time. This behaviour is clearly visible at the bottom left panel of figure 3.2. In order to test the digital circuitry a hit register can also be set by asserting a digital pulse DPULSE in coincidence with a strobe signal. There are different ways to reset a hit register. When a register is read out, a PIX_RESET signal is generated by the priority encoder to clear the memory after the readout is done. Here, readout refers to sending the encoded *address* of the hit pixel to the chip periphery

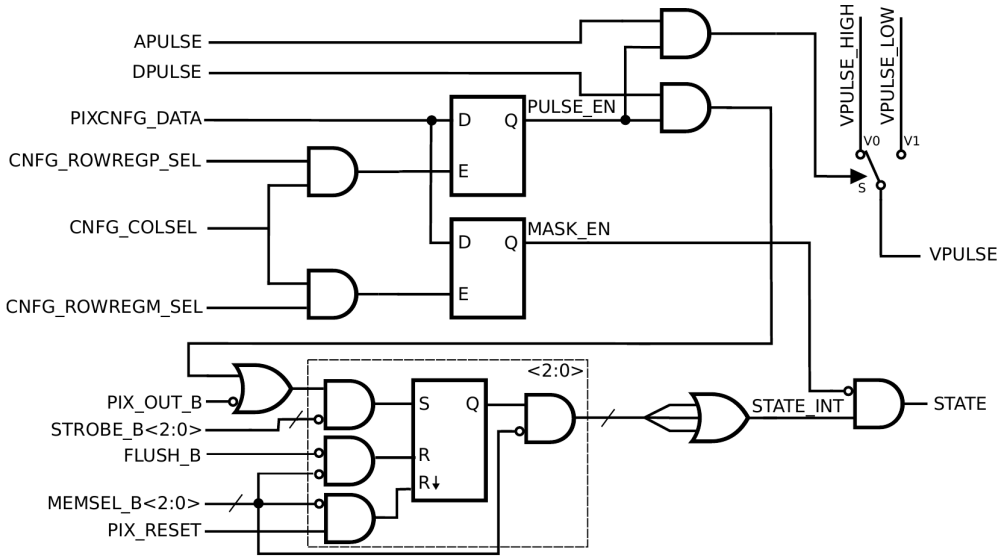

Figure 3.3 Schematics of the implemented digital in-pixel logic of the ALPIDE chip. There are the common logic gates AND (rounded symbols) and OR (triangle-like symbols). Negation of the logic signal is denoted by an *o* at the input. Furthermore, two registers to set pulsing and masking are shown (D: data, E: enable, Q: output). The essential part are three equivalent event buffers (grey, dashed box) each consisting of one set-reset latch (S: set, R: reset, Q: output). For better visibility only one buffer is explicitly shown [5].

only if the STATE of the pixel is asserted, i.e. the selected hit register is set[4] (and not masked). The second method to reset a hit register is via a global FLUSH_B signal sent from the periphery.

In addition to the *multi event buffer*, there are two more registers that can be set according to a set of input variables, thus making the pixel programmable. One of them is the MASK_EN (enable masking), which effectively masks the pixel to the readout if it is set. Independent of the internal state STATE_INT, i.e. the hit register information, the output STATE of the pixel is forced to be zero. As such this provides a possibility to ignore misbehaving or broken pixels in the readout. The second register can be set to enable digital or analog pulsing by asserting the PULSE_EN signal. These pulses can be used to either test the digital circuitry as mentioned before or the analog one by sending APULSE. This will either set VPULSE_HIGH or VPULSE_LOW which then serves as input to the injection capacitor C_{inj} as it can be seen in figure 3.2 at the top left.

A very detailed overview of all (control) registers from the ALPIDE chip as well as their role and functionality is given in [21]. Additionally, the readout process and the specific output data format of the ALPIDE chip is explained there.

3.4 Sensor performance of non-bent ALPIDE chips

To finally characterise and evaluate the performance of the ALPIDE chip, extensive testing campaigns were performed not only for the final chip design, but also for the full-scale prototypes. These tests involved laboratory measurements to simply test the chip electronics and response by using analog and digital pulsing as described in the previous section, as well as testbeam experiments similar to the ones presented in chapter 4. The performance studies on the full-scale prototype ALPIDE chips pALPIDE-1, -2 and -3, are presented to full extend in [43, 44, 35]. Here,

[4]The full address/location of the pixel is built in the periphery and consists of three ID numbers: readout region, double column, pixel

each result obtained with one prototype served as an input for the next optimised iteration of the ALPIDE chip.

In the end, the final chip design was tested in order to ensure that all requirements of the ITS2 upgrade project, which are summarised in section 2.2.1, are indeed fulfilled. The main parameters of interest for such a performance study are *sensor efficiency* and *position resolution*. In the scope of this work, the performance of a standard (flat) ALPIDE chip is compared to two different kinds of bent ALPIDE sensors, which are presented in section 4.2. Since the studies on the bent sensors were only performed without the application of a back-bias voltage $V_{\mathrm{BB}} = 0\,\mathrm{V}$, only the corresponding results for flat ALPIDE chips are presented in the following. For a full performance study of standard ALPIDE sensors [5] can be consulted. Performance and results for the bent ALPIDE chips are presented in chapter 6.

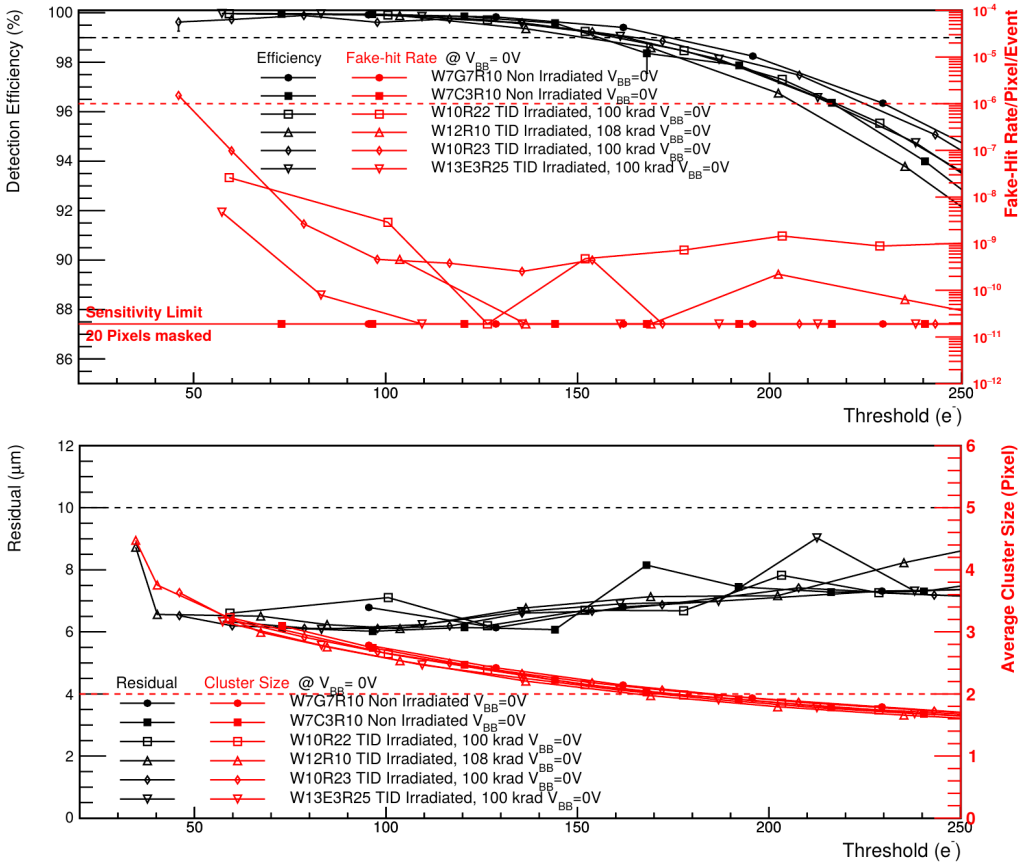

Figure 3.4 **(top)** Detection efficiency (black) and fake-hit rate (red) of several flat ALPIDE chip as a function of in-pixel threshold without back-bias $V_{\mathrm{BB}} = 0$. There are several curves shown, which are attributed to different sensors (different symbols). Moreover, some of the presented sensors have been tested before (full symbols) and after (open symbols) irradiation to test for radiation hardness. Irradiated sensors have been subject to a TID of $100\,\mathrm{krad}$ and NIEL of $10^{12}\ 1\,\mathrm{MeV}\ n_{\mathrm{eq}}\,\mathrm{cm}^{-2}$ [5].
(bottom) Residual (black) as measure for position resolution and average cluster size (red) of several flat ALPIDE chip as a function of in-pixel threshold without back-bias $V_{\mathrm{BB}} = 0$. There are several curves shown, which are attributed to different sensors (different symbols). Moreover, some of the presented sensors have been tested before (full symbols) and after (open symbols) irradiation to test for radiation hardness. Irradiated sensors have been subject to a TID of $100\,\mathrm{krad}$ and NIEL of $10^{12}\ 1\,\mathrm{MeV}\ n_{\mathrm{eq}}\,\mathrm{cm}^{-2}$ [5].

The main performance plots for several flat ALPIDE chips, which are tested in different testbeam campaigns, are summarised in figure 3.4. In the upper panel, the sensor efficiency is plotted versus

the respective average in-pixel threshold set for the chip. Here, the efficiency is calculated as the number ratio of reconstructed particle trajectories (tracks), which feature an associated hit or cluster on the device under investigation (DUT), over total reconstructed tracks. The efficiency calculation is described in more detail in section 5.9. The upper dashed line indicates a value of $99\,\%$ efficiency, i.e. for one in 100 reference tracks no hit could be associated on the DUT.

It is clearly visible that all tested chips, which are represented by different symbols, show an *efficiency* larger than $99\,\%$ for a large range of threshold settings. This is especially true around the nominal working point of the ALPIDE chip at $100e$. A decrease in sensor efficiency towards larger threshold values, as it can be seen in the top plot, is expected. With an increasing threshold the probability that a possible signal of a particle is not registered, because it is to small to overcome the threshold, is increased as well. This ultimately leads to a decrease in efficiency by definition. In addition, some of the presented chips (open symbols) have been subject to ionising and non-ionising radiation before their measurement, in order to study the effect of radiation damage. Here the used total ionising dose (TID) of $100\,\mathrm{krad}$ and the non-ionising energy loss (NIEL) of $10^{12}\ 1\,\mathrm{MeV}\ n_{\mathrm{eq}}\,\mathrm{cm}^{-2}$ were chosen such that they represent the expected dose received by the sensors during their lifetime in the ITS2 including a *safety factor* of ten [5]. It is shown that the irradiation has no significant effect on the efficiency.

As a measure of the sensor noise, the *fake-hit rate* is shown on the right vertical axis in figure 3.4 at the top alongside with the efficiency. It is the probability of a pixel registering a hit when receiving an external trigger, but there was no external stimulus that could have generated the measured signal. For the fake-hit rate measurement, which is described in section 4.4, the 20 most noisy pixels where masked, thus introducing a sensitivity limit of the test. It is shown that the fake-hit rate is below the sensitivity limit for the non-irradiated sensors and is increased after irradiation. Nevertheless, the fake-hit rate after irradiation is still complying with the ITS2 requirements, which are indicated by the lower dashed line. The lower the threshold value is, the more probable it is for a pixel to show a hit induced by (electronic) noise. Therefore, the increase of the fake-hit rate towards lower threshold values is expected.

The lower panel in figure 3.4 shows (track) *residuals* as a measure of the position resolution in their dependency on the measured chip thresholds for the same ALPIDE chips for which the efficiency is also evaluated. Here, residual refers to the distance between an associated cluster on the DUT and the respective track intersection point with the sensor surface as described to full extent in section 5.9. Thus, residuals are a convolution of the actual *position resolution* of the sensor and the uncertainty of the tracking. Consequently, the position resolution is always smaller than the corresponding residual value. For a wide range of threshold settings the residual values for irradiated and non-irradiated chips are well below $10\,\mu\mathrm{m}$ and almost constant. Again, there is no visible degradation of the sensor performance with irradiation.

A slight increase of the residuals, corresponding to a slightly worse position resolution, is visible towards larger threshold values. This trend can be linked to the cluster size, which is shown in the same plot on the right vertical axis. It is understandable that the cluster size decreases with increasing threshold, since shared charge with adjacent pixels is less likely to pass the threshold criterion and render the respective pixel to detect a hit. Effectively, the number of involved pixels in a cluster gets smaller. On the other hand, with decreasing threshold and larger clusters the position of the particle gets more precise, since it is calculated as the mean of the pixel positions in the cluster. As a result, the overall position resolutions improves with lower threshold, i.e. larger clusters. For particles close to the minimum-ionising regime (MIP) the cluster size is expected to be between two and three. This can be nicely seen at the nominal working point of about $100e$. In summary, both non-irradiated and irradiated ALPIDE chips have been proven to fulfil

requirements and expectations of the ITS2 upgrades. As such, the obtained results can be used as a legitimate reference for the performance evaluation of bent ALPIDE chips.

4 Testbeam campaigns for curved sensor characterisation

In order to investigate the performance of a detector, a so-called *testbeam experiment* or *beam test* is performed. During such experiments, the detector that is to be investigated, usually referred to as device under test (DUT), is subject to a particle beam with well-known properties. The accelerator facility, providing and monitoring the beam, hereby has the main control over the beam parameters such as particle species, particle rate, beam energy and momentum and their respective spread. Another important parameter of a testbeam is the focus of the particle beam, i.e. how large the *beam spot* at the point where the detectors are located is. A specific set of parameters can be requested at the testbeam facilities. Some of them even provide the means for a direct user intervention to tune some of the beam parameters.

The general idea of a testbeam experiment is to use well-known, already characterised detectors as a reference and compare their performance to the one of the DUT. These reference detectors are therefore placed in the beam line, before and after the DUT. A multitude of aligned reference detectors is referred to as *beam telescope* or just *telescope*. Being made of pixelated detectors, the position of a traversing beam particle can be measured for each reference detector plane. During the analysis of the testbeam data, which is described in detail in chapter 5, this information will be used to eventually reconstruct the particle's trajectory called *track*. A major part of further analysis goals, especially the ones addressing the performance of the DUT, rely on such tracks. Depending on the type of telescope and DUT, additional detectors with a sufficient time resolution might be required for providing an external trigger signal. Plastic scintillators are a commonly used example of such trigger detectors.

In the following sections the testbeam campaigns that are relevant for this work are presented. This especially includes the detailed description of the setups that have been used to gather the data, which lead to the results presented in chapter 6. Additionally, other tests of the DUT, which have to be performed prior or after a testbeam campaign are described.

4.1 The DESY II testbeam facility

There are numerous accelerator facilities around the world offering the possibility to perform beam tests for external users. For this work, all test beam campaigns have been carried out at the test beam facility of the German Electron Synchrotron (DESY) located in Hamburg, Germany. There, the *DESY II* synchrotron, which usually accelerates electrons, provides beams to three independent beam lines 21, 22 and 24. A sketch of the DESY II test beam area can be seen in figure 4.1 at the top. For the testbeam experiments performed for this work only beam line 24, providing an electron beam was used.

After the injection by a linear preaccelerator at an energy of $E_{\min} = 0.45\,\mathrm{GeV}$, a bunch of about 10^{10} electrons is accelerated to an energy of $E_{\max} = 6.3\,\mathrm{GeV}$ inside DESY II. The beam is then stored with an oscillating beam energy ranging between $E_{\min}$ and $E_{\max}$ as it is illustrated in figure 4.1 at the bottom. During acceleration and deceleration of the particles, the electrical current through the accelerator bending magnets needs to be continuously adjusted, which marks one *magnet cycle*. After two magnet cycles the beam is dumped. This entire period from beam

injection to extraction lasts 160 ms and is referred to as one *DESY II cycle*. It is understandable that the deceleration to minimal energy comes with beam losses, which are clearly visible as decreased beam intensity during the second magnet cycle. Besides providing the experimental ares with a particle beam, DESY II also serves as an injector for the larger synchrotron PETRA III. During nominal accelerator operation the DESY II beam is extracted to *top up* the PETRA III beam every few minutes rendering the testbeam availability to be almost 99 % in this case [45].

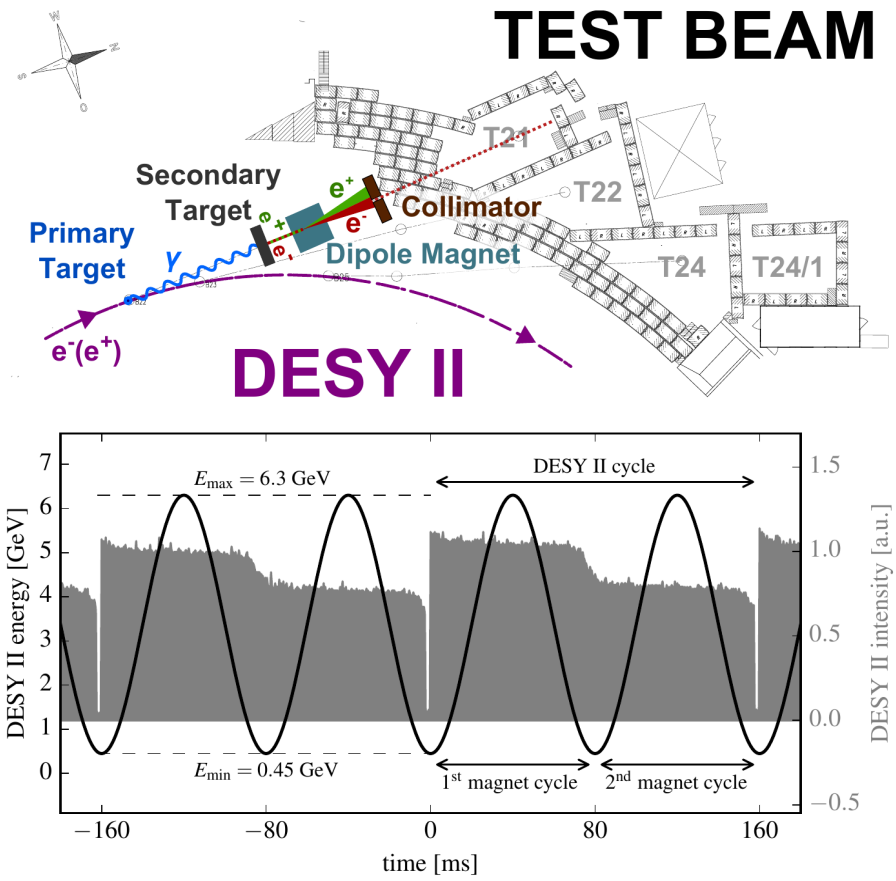

Figure 4.1 **(top)** Sketch of the DESY II testbeam area. The beam path of the DESY II synchrotron is shown in purple, while the three experimental areas with beam access are depicted in grey and labelled T21, T22 and T24, respectively. Additionally, the parasitic beam generation is schematically visualised for T21. This especially involves two targets, a dipole magnet and a primary collimator [45].
(bottom) Oscillating beam energy of the DESY II synchrotron versus time. The maximum and minimum beam energies, as well as the time period of one full machine cycle are highlighted. In the background the corresponding beam intensity is plotted in grey. Over the time period of two machine cycles the beam injection and ejection pattern is visible [45].

The testbeams provided at the DESY II testbeam facility are produced by so-called *parasitic beam generation* in contrast to extracting and using the primary beam directly. The principle of this kind of beam generation is illustrated in figure 4.1 at the top. For this process, a several micrometer thick target wire is placed in the primary beam orbit, such that Bremstrahlung photons are generated at all available beam energies. These high-energy photons tangentially escape the beam pipe of the synchrotron. When they hit a secondary conversion target electron-positron pairs are generated by the *pair production* process. The converted electron-positron pairs show a certain energy and momentum spread, for example due to the energy dependence of the Bremstrahlung

generation or multiple scattering of the particles in the secondary target, when they enter another evacuated beam pipe.

On their way to the experimental area, the beam particles pass through the magnetic field of a *dipole magnet*, which forces them to fan out according to their momentum and particle species. An adjustable collimator then *cuts out* and focuses the final beam that is delivered to the experimental area. There, the incident particle beam exits the beam pipe and is monitored by a simple *beam counter* comprising two scintillators for a particle rate measurement. Finally, a static lead collimator determines the shape of the beam used for the experiment.

By controlling the collimator settings, but more importantly the field of the dipole magnet, the user can select between electrons and positrons and a certain momentum or energy range of the respective particles. Due to the oscillating energy pattern of the primary beam inside the DESY II synchrotron, the rate of the parasitically generated testbeam scales with the selected testbeam energy. A higher selected energy leads to a lower particle rate. For this reason an electron beam energy of $5.4\,\mathrm{GeV}$ was chosen as a tradeoff between high energy and particle rate for each performed beam test leading to the presented results of this work. A sufficiently high energy is needed in order to reduce the effect of multiple scattering in the detector layers of the beam telescope or the DUT. Secondly, a higher particle rate helps gathering the required amount of data in a reasonable time period to perform the subsequent statistical analysis.

4.2 Beam telescopes and devices under test

Within the scope of this work, the first ever in-beam characterisation of a bent MAPS was performed in a testbeam campaign at the DESY II testbeam facility in June 2020 [46]. A second beam test with a differently bent ALPIDE as DUT followed in August of the same year. In both of the testbeam experiments, a beam telescope featuring six flat ALPIDE chips as reference detectors was used to measure the performance of the bent DUTs.

Each of the reference ALPIDE chips is mounted in a separate metal case with a window cut out at the active area of the sensor. The reference planes are then screwed onto a breadboard featuring a fixed minimal distance of $2.5\,\mathrm{cm}$. This flexible mounting of the reference planes allows to accommodate the bent DUTs in the middle, which require more space. Pictures of the mounted reference planes with the differently bent DUTs for the June and August testbeam campaign can be seen at the right of figure 4.2 and figure 4.4, respectively.

It is also visible that each of the detectors is connected to, and readout by, a dedicated data acquisition (DAQ) board. First of all, power is usually delivered to the ALPIDE chip via these DAQ boards. For readout purposes they all feature a field-programmable gate array (FPGA), which needs to be programmed with the project-specific firmware, in order to communicate with the attached ALPIDE chip. Furthermore, a clock of $80\,\mathrm{MHz}$ is provided to assign timestamps to registered events.

If an external trigger signal is provided, all DAQ boards of the beam telescope and the DUT can be daisy-chained in order to distribute this signal to each detector. The same is true for the BUSY-signal that is sent by the ALPIDE chip during readout. While the chip is BUSY no trigger is accepted until the readout process has finished and the BUSY-state is lifted. Daisy-chaining all involved DAQ boards leads to a combined BUSY-signal for the entire experimental setup, thus ensuring that all chips have finished the readout before registering new events again.

Before performing the testbeam experiment, the reference planes are tuned and set to their optimal working points using the procedure and scans described in section 4.4. In contrast to the DUTs, the reference planes are always operated with a back-bias voltage of $V_{\mathrm{BB}} = -3\,\mathrm{V}$, in

order to reduce the noise level and increase the depletion region in each of the pixels. For the most efficient operation the chip parameters are set such that they result in an average in-pixel threshold value of $100e$. In the following sections, more details on the experimental setups and especially the DUTs utilised in the June and August testbeam campaigns are given.

4.2.1 Testbeam DESY June 2020

The first feasibility test of bending an ALPIDE chip was performed using a roll of sticky tape and a non-functional chip. Since the rigidity of a $50\,\mu m$ thick silicon sensor can be compared to the one of photobase paper, it is easily imaginable that an ALPIDE chip can be bent and held in place on a role of sticky tape. To produce an electrically functional bent ALPIDE chip, which can be tested in a particle beam, requires a more elaborate and controlled bending procedure and mechanics.

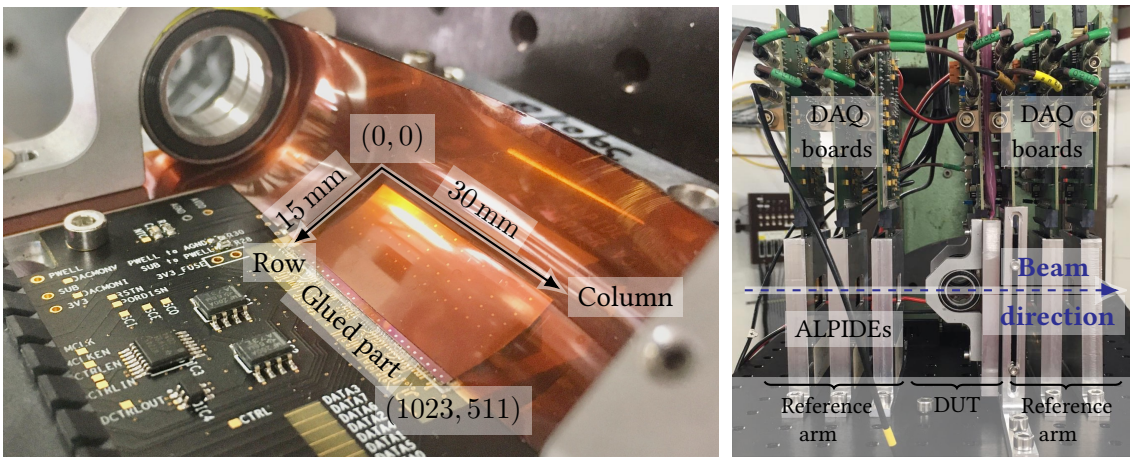

Figure 4.2 **(left)** Image of the bent DUT used in the DESY testbeam campaign in June 2020. The ALPIDE chip is sandwiched between two sheets of Kapton foil (orange). It is then bent and fixed in position using wheels and metal support structures at both sides of the carrier card (black circuit board).
(right) Bent DUT from the left image mounted within the ALPIDE beam telescope. There are three reference detector planes upstream and downstream of the DUT building one reference arm each. All detector planes are read out by DAQ boards, which also distribute power and back-bias voltage to the ALPIDE chips. At the top of the DAQ boards two daisy chains for trigger and busy signals are visible.

A picture of the resulting DUT, which was prepared by collaborators at INFN[1] in Trieste, can be seen in figure 4.2 on the left. At first an ALPIDE chip is glued to the usual black carrier card with a $2\,mm$-wide area on the long side of the chip that accommodates the bonding pads, digital periphery and the very beginning of the pixel matrix. The carrier card mainly serves the purpose of conveniently interfacing the ALPIDE chip and the DAQ board. As such, it contains rudimentary electronics for signal and power distribution, as well as decoupling elements to filter electronic noise. After gluing, the chip is wire-bonded to the carrier card for electrical connection.

For the actual bending, the sensor is sandwiched between two $120\,\mu m$-thick polyimide foils, which are held together by double-sided sticky tape. The foils are then wrapped around two metal wheels as they are moved in parallel along the direction of the short chip edge with a micrometre-precision positioning system. As a result, the chip in between the foils is bent to a

[1]Istituto Nazionale di Fisica Nucleare (National Institute for Nuclear Physics), Department: Trieste, Italy

cylindrical shape in a manner that the integrated electrical circuitry on top is *compressed*. Finally, the metal wheels are fixed in position by U-shaped aluminium braces.

In order to quantify the bending radius after this mechanical procedure, a coordinate measurement machine (CMM) with an optical head is used to map the surface of the bent chip. Hereby, the measured coordinate points on the sensor surface have an uncertainty of $5\,\mu\mathrm{m}$ in the plane of the carrier card and $80\,\mu\mathrm{m}$ in height. From these measurements the average bending radius is determined before and after the testbeam campaign by fitting a subset of data points in row direction with a circle while allowing for a flat part in the region, where the chip is glued to the carrier card. Before the beam test a bending radius of $r_{\mathrm{before}} = 16.9\,\mathrm{mm}$ is found, while after the testbeam campaign a value of $r_{\mathrm{after}} = 24.4\,\mathrm{mm}$ is obtained[2]. The difference between these radii is explained by a relaxation of the polyimide foils with time, leading to a larger radius for the second measurement. The bending radius of the chip during the beam test is therefore expected to be within the range of the CMM measurement radii [46].

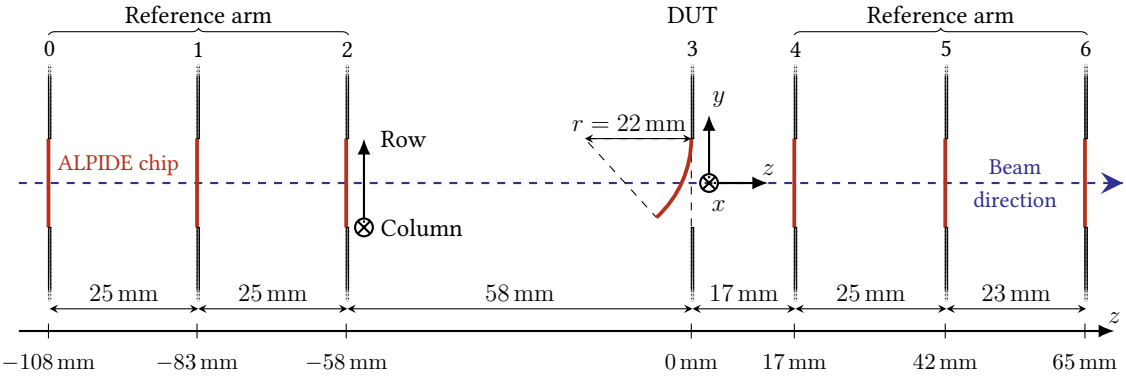

Figure 4.3 Schematic side view of the beam telescope with the bent DUT for the DESY testbeam campaign in June 2020. ALPIDE chips are denoted in red, while the carrier cards are illustrated in grey (not to scale). The shown coordinate axes represent the local sensor coordinates, i.e. column and row numbers, and the global coordinate frame (x,y,z) used by Corryvreckan, which is described in section 5.2.

After the bending procedure, also the electrical functionality of the DUT required verification. The results of the laboratory tests performed for this purpose are presented in section 4.4. During the testing procedure it turned out that double column number 13 in chip region 11 is inoperable. Consequently, it had to be masked, as described in section 3.3, for data taking. The tested and otherwise functional DUT is then inserted in the beam telescope as it is shown in figure 4.2 on the right. The kind of mounting structure for the DUT especially allows to vary its height with respect to the reference planes. Consequently, the beam can be focussed on different regions of the chip, i.e. larger or smaller beam incident angle with respect to the bent sensor surface normal. To prevent light-induced noise, the entire telescope setup is put in a light tight box before starting the (in-beam) measurement.

The final experimental setup is sketched in figure 4.3. All distances between the planes, which are relevant for the data analysis, are measured using a sliding calliper. The shown coordinate systems serve as a reference to the ones used by the data analysis framework Corryvreckan and are described in more detail in section 5.2. The relatively large space between the second plane and the DUT is mainly dictated by the mechanics and mounting procedure of the DUT.

[2]The corresponding plot, showing the results of the CMM measurement, can be seen in figure A.2 in section A.3 in the appendix.

4.2.2 Testbeam DESY August 2020

For the second testbeam campaign featuring in-beam performance test of a bent ALPIDE chip, a different approach is followed at INFN in Trieste for the manufacturing the bent DUT. A picture of the bent ALPIDE chip, which was investigated during the beam test in August 2020 can be seen in figure 4.4 on the left. The major visible difference is that the bent axis is parallel to the long side of the chip, while it used to be parallel to the short chip edge for the testbeam campaign in June 2020 (cf. figure 4.2). As a consequence, the integrated (in-pixel) electrical circuitry is now in a *decompressed* state, potentially leading to differences in the electrical properties of the DUTs used in June and August beam tests as further discussed in section 4.4.

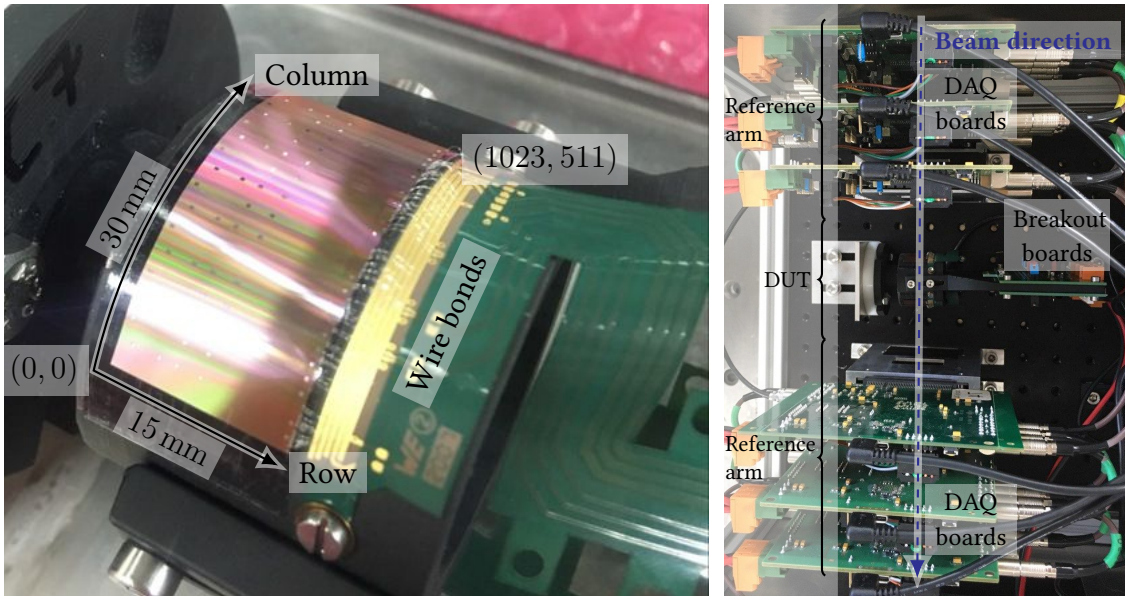

Figure 4.4 **(left)** Image of the bent DUT used in the DESY testbeam campaign in August 2020. The ALPIDE chip is bent and bonded to an FPC on a 3D-printed cylindrical jig, which features a cutout underneath the chip. The sensor is held in position by a sticky tape. The FPC is connected to a breakout board shown in the right picture, which then connects to a DAQ board.
(right) Top view of the same bent DUT mounted within the ALPIDE beam telescope. There are three reference detector planes upstream and downstream of the DUT, building one reference arm each. All detector planes are read out by DAQ boards, which also distribute power and back-bias voltage to the ALPIDE chips. The bent DUT is an exception, since it is connected to a breakout board, which then connects to a DAQ board (not in the picture). On the right the trigger and busy daisy chain can be seen, while on the left the power chain of the DAQ boards is visible (orange connectors). At the top of the DAQ boards there are the USB cables for data transfer.

The difference in bending direction naturally lead to the development of suitable bending techniques and mechanics to hold the bent ALPIDE chip in place. In contrast to the DUT used in June, the sensor for August is first bent and then electrically connected by wire bonds. For the bending a *cylindrical jig* is 3D-printed, which allows for a very good manufacturing precision and control of the shape. The radius of the cylindrical jig is $r = 18\,\mathrm{mm}$ just as the target radius for the bent chip. This corresponds to the intended radius for the innermost layer of the ITS3. Furthermore, a window with a width of $5\,\mathrm{mm}$ and a length exceeding the sensor length of $30\,\mathrm{mm}$ is cut out of the plastic cylinder at the position where the chip is supposed to be located. In order to hold the sensor in place on the jig, a double-sided adhesive tape is used. For the actual bending procedure of the ALPIDE chip, it is positioned on top of the cylindrical jig with the cutout by

hand. The chip is then bent carefully forcing it to follow the shape of the cylinder by using a piece of polyimide foil. Starting at one of the short sides and then moving on towards the other one in a *rolling fashion*, the chip bends gradually until it is fully bent and fixed in the final position by the adhesive tape underneath. The polyimide foil ensures the equal distribution of the forces acting on the chip during the bending procedure. It is obvious that too much stress at one specific point can cause the chip to break apart. After the bending procedure has been successful, the polyimide foil is removed.

For the first bent ALPIDE chips of this type, the full bending procedure is performed by hand and therefore is very much dependent on the sense and expertise of the executing person. In the meanwhile, this kind of bending process has been automatised using stepping motors and rotational stages to allow for better stress control and reproducibility. Additionally, for later iterations of bent ALPIDE chips the sensor is held in place by a polyimide foil with a window cutout instead of the adhesive tape.

The electrical connection of such a bent ALPIDE chip poses a special challenge, since the area hosting the bonding pads is now bent. To be able to connect the chip to a DAQ board for the readout, it is first wire bonded to a *flexprint* cable (FPC), which acts as the interface to a flat printed circuit board (PCB) such as the DAQ board. For the DUT shown in figure 4.4, the connected electrical lines on the FPC are fanned out on a so-called breakout board for spatial reasons. From there, the data lines are finally connected to a modified carrier card, which can be plugged into a DAQ board. Since there is no standard carrier card anymore, the chip has to be powered directly from a low-voltage power supply (LVPS). Furthermore, the usually used serial data link is not connected, which is why the *slow control* interface needs to be used for readout. As these names already suggest, the readout procedure requires more time for this DUT as compared to the reference ALPIDE chips in the beam telescope. This needs to be accounted for in the trigger logic described in section 4.3.

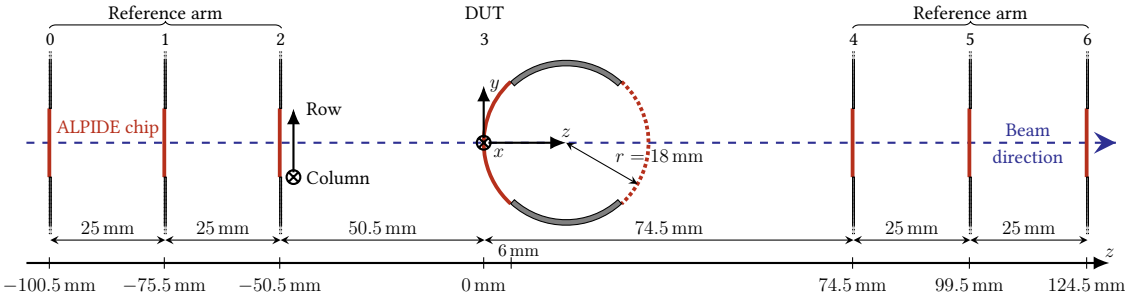

Figure 4.5 Schematic side view of the beam telescope with the bent DUT for the DESY testbeam campaign in August 2020. ALPIDE chips are denoted in red, while the carrier cards and the cylindrical jig carrying the DUT are illustrated in grey (not to scale). The second bent ALPIDE (dotted) was present during the testbeam, but not functional. The coordinate axes represent the local sensor coordinates, i.e. column and row numbers, and the global coordinate frame (x,y,z) used by the Corryvreckan analysis framework, which is described in section 5.2.

As similar to June testbeam, the DUT is inserted in the middle of the beam telescope and mounted on the same breadboard using an L-shaped aluminium piece. A top view of the full beam telescope, including the bent DUT for the August testbeam, can be seen in figure 4.4 on the right. The mounting of the cylindrical DUT allows for alignment adjustments and for the possibility to rotate the bent ALPIDE chip such that the beam can intersect it twice due to the sensor curvature. This is referred to as *double crossing* position, while the nominal position only allows for *single crossing* of the beam. The relevant distances and coordinates needed for the

data analysis of the single crossing configuration are sketched in figure 4.5. It is visible that by design of the cylindrical jig, in principle two bent ALPIDE chips can be mounted opposite of each other allowing to simultaneously test both of them in the beam. However, during the electrical functionality test one of the two DUT chips turned out to be not functional. This chip is shown as a dotted red line.

4.3 Trigger system

As described in chapter 3 and particularly in sections 3.2 and 3.3, the ALPIDE chip is designed to be used in a triggered fashion as opposed to providing a continuous output. Therefore, an external trigger signal has to be generated, processed and fed to the ALPIDE beam telescope during testbeam experiments. Here, the trigger serves the purpose that data is only readout and written to disk, if a particle has traversed the beam telescope and the DUT. Since it basically is a binary signal, standard logical operations can be performed to combine the output from several trigger detectors to introduce a trigger veto if necessary. Usually, this logic signal processing is done using Transistor-Transistor Logic (TTL) modules or Nuclear Instrumentation Modules (NIM). Since these two different types of modules also implement different voltage standards, e.g. active-high as compared to active-low, *level adaptor modules* can be used to convert from one system to another. There is also the possibility to feed the output of the trigger detectors into a dedicated *trigger board* or trigger logic unit (TLU), which both make use of an FPGA to process the signals.

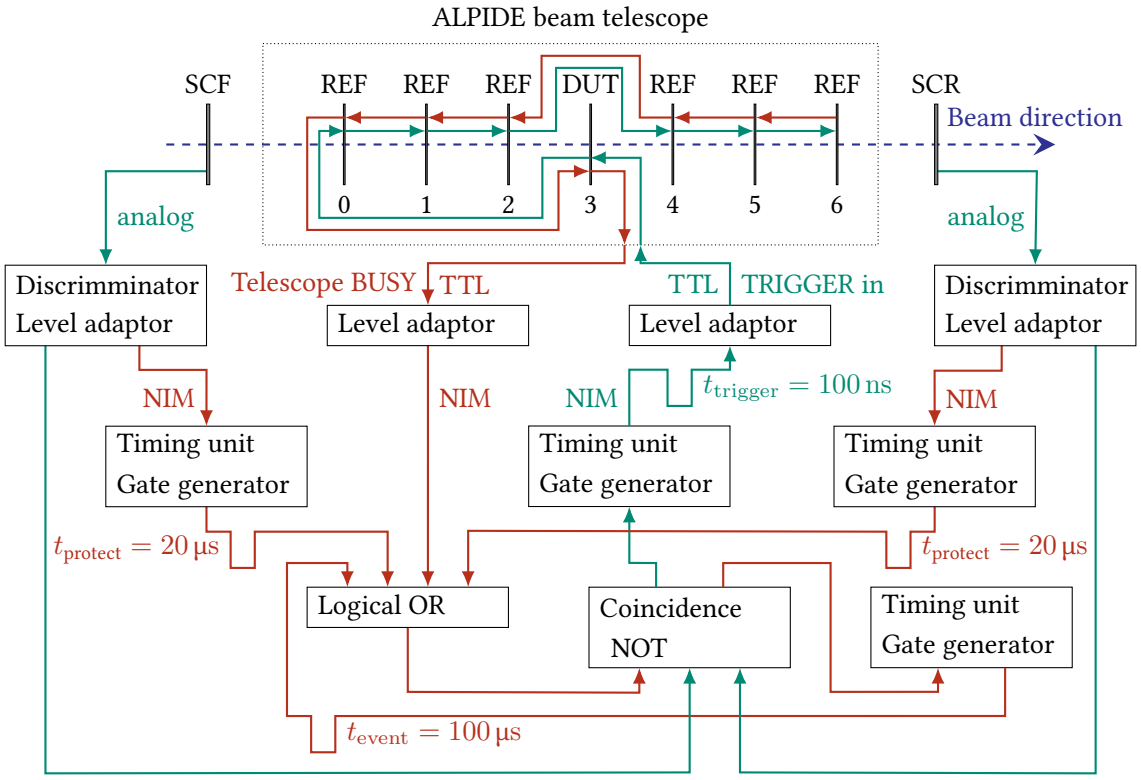

Figure 4.6 Schematic illustrating the trigger logic used for both, June and August 2020, testbeam campaigns at DESY. Signals of type BUSY are denoted in red, while signals of type TRIGGER are sketched in green. There are two different voltage standards TTL and NIM for different modules. The main trigger input comes from two scintillators in front (SCF) and after the beam telescope (SCR). The important signal lengths are denoted by t.

For the testbeams performed for this work the first option, i.e. using TLL-modules and NIM, is implemented. A schematic illustration of the full trigger logic can be seen in figure 4.6. In general there are two types of signals, namely TRIGGER drawn with green lines and BUSY denoted in red. As their name suggests, TRIGGER signals are processed and send to each plane of the beam telescope including the DUT in order to trigger the registering and thus later readout of an event. A trigger input leads to a STROBE pulse as described and illustrated in section 3.3 and figure 3.3. In contrast, signals of type BUSY are used to prevent a trigger to reach the beam telescope planes and thus act as a *trigger veto*.

The raw signals for the trigger input are generated by a pair of plastic scintillators. Each covering a slightly larger area as compared to an ALPIDE chip of approximately $5\,\mathrm{cm} \times 4\,\mathrm{cm}$, one of them is placed in front (SCF) and one behind (SCR) the beam telescope with respect to the beam direction. A TRIGGER `in` signal is generated or *accepted* if the discriminated signal of both scintillators are coincident and no `combined` BUSY is present. This geometry ensures that a beam particle has traversed the full beam telescope with a high probability.

There are two kinds of BUSY signals, which are combined by simply adding them in a *logical or* fashion. First, each discriminated scintillator output generates a pulse of $t_{\mathrm{protect}} = 20\,\mu\mathrm{s}$. This so-called *past protection* is introduced to prevent event pile-up by beam particles very close in time, since the amplifier pulse inside an ALPIDE pixel can reach up to several tens of microseconds for settings leading to a very low in-pixel threshold (see figure 3.2). This means in particular no trigger is accepted for a duration of t_{protect} after any of the scintillators shows a particle hit. Furthermore, an *event separation* time of $t_{\mathrm{event}} = 100\,\mu\mathrm{s}$ is introduced after each accepted trigger, thus limiting and giving control over the maximum measurable rate of this testbeam setup. The last contribution to the `combined` BUSY is the BUSY sent by the ALPIDE chips in the beam telescope. The busy of each detector plane in the beam telescope is combined by a *logical or*. Hence, it is active during the readout of any of the chips introducing a dead time for this purpose.

When a trigger is accepted it is forwarded to the first detector in the *trigger chain*, which is called *trigger primary*. The length and amplitude of this signal is dictated by the ALPIDE chip electronics in this case. The trigger is then subsequently distributed to the other detectors. For a proper functionality of the trigger system and the readout, it is crucial that the trigger primary is the detector with the slowest readout. Otherwise, the data acquisition (DAQ) system might stop the readout after finishing with the trigger primary plane. This especially applies to the testbeam campaign in August, where the DUT was read out using the slow control interface of the ALPIDE chip. Additionally, with the update to the DAQ framework EUDAQ2, which is described in section 4.5, and the related update in the firmware of the DAQ boards parts of the BUSY signal processing was handled on software level for the August testbeam campaign.

4.4 Laboratory tests and threshold scans

In preparation of a testbeam campaign several laboratory tests are to be performed for the reference detectors and the DUT. As described in section 4.2 all planes of the beam telescope are flat ALPIDE chips for every beam test performed in the scope of this work. Furthermore, the DUTs are bent ALPIDE chips. For this reason, the tests described in the following are specific to the ALPIDE sensor. However, the idea and motivation of the tests presented might also apply to a more general case with different (pixel) detectors.

There are several reasons why laboratory tests are needed before a testbeam campaign. The most simple one is to ensure proper electrical behaviour and functioning of all involved detectors. In order to test a single ALPIDE chip, it is connected to a DAQ board, which is powered by a

low-voltage power supply. This DAQ board needs to be programmed, in particular referring to its FPGA and FX3 components, in order to enable proper communication via a USB connection and install the *proprietary firmware* for reading out the connected ALPIDE chip. After programming, a first check that can be done is to observe the currents being drawn by the ALPIDE chip and the DAQ board depending on the set back-bias voltage V_{BB}. In case of problems with the chip currents higher than three times the expected value might be observed. To protect the chip from the resulting increased power dissipation, which could permanently damage it, it is advisable to set a current limit on the used power supply, i.e. *fuse-protection*.

Digital scans As already mentioned in section 3.3 the digital part of the pixel can be tested for proper functioning. Furthermore, there are also tests available[3] to investigate the digital periphery of the ALPIDE chip. In order to ensure an error-free communication with the electronics at the end of each double-column, a so-called *FIFO test* can be performed. Here, predefined bit patterns are written in the First In First Out (FIFO) organised registers and written back. The read back value is then compared to the corresponding input value and checked for correctness.

Secondly, the chips working point is steered using DAC values, which are then converted to their analog equivalent on the chip. In order to measure the correspondence of DAC and analog values, the DAQ board is equipped with analog-to-digital converters ADCs. During a *DAC scan* the ALPIDE chip needs to be connected with monitoring pins (the pads can be seen in figure 3.1 on the left). For each DAC every possible value ranging from 0 to 255 is set and encoded again with the ADCs on the DAQ board.

The digital output of single pixels can be tested using *digital pulsing* which is implemented in the in-pixel electronics as it can be seen in figure 3.3. Running this scan, such a digital pulse can be injected in a specified number of pixels all over the chip pixel matrix. The chip is then read out and the registered hits can be visualised by plotting a two-dimensional *hitmap*. As such, the addresses of the targeted pixels and pixels showing a hit can be compared [47].

Noise occupancy scan Another test for the ALPIDE chip, which also requires the readout of the pixels, is the *noise occupancy scan*. As the name suggests, it serves the purpose to determine the noise level of the chip to be tested. The noise is hereby expressed as *fake-hit rate* R_{FH}, which is defined as the average number of hits per pixel and per event without actively providing an external stimulus to generate hits in the pixel matrix of the chip. In particular no radioactive source, particle beam or similar is present during the time period of this scan. Furthermore, the sensor is shielded from light. Performing this scan, the chip is first configured with a set of parameters since the outcome of this test is dependent on its working point and especially the set in-pixel threshold. Then, a predefined number of external triggers N_{trig}, usually about $100\,000$, are subsequently provided to the chip, which is then read out each time. Having no external stimulus a registered hit of a pixel is therefore attributed to noise [47].

There are two main contributions for noise, namely *thermal noise* or so-called Random Telegraph Noise (RTN), which most likely is an attribute of the MOS-transistors in the ALPIDE chip [48]. Another inevitable contribution to the noise level is cosmic radiation, however it is tried to mitigate its effect in the analysis of the scan data. Having the total number of registered pixel hits

[3] The required software is distributed via a protected git repository:
`https://gitlab.cern.ch/alice-its3-wp3`

during the scan N_{hits} and the number of pixels on the chip N_{pix}, the according fake-hit rate can be calculated as described by equation 4.1 [5].

$$R_{\text{FH}} = \frac{N_{\text{hits}}}{N_{\text{pix}} \cdot N_{\text{trig}}} \tag{4.1}$$

To get a representative value for the full chip and to account for other sources of possible noise, usually the 20 most noisy pixels are ignored for the analysis. Moreover, it can be seen that the test naturally features a lower sensitivity limit due to the limited number of triggers. This limit represents less than one detected hit during the full test and is calculated in the following for the nominal test numbers according to equation 4.1.

$$R_{\text{FHlim}} = \frac{1}{(512 \cdot 1024) \cdot 100000} \approx 1.9 \times 10^{-11} \frac{\text{hits}}{\text{pixel} \cdot \text{event}} \tag{4.2}$$

To identify regions on the chip, which are more noisy than others, the hit information of the noise occupancy scan can be visualised as a two-dimensional hitmap. Where the chip is more noisy the hitmap shows a higher count of hits for a specific pixel or chip area. To fully characterise an ALPIDE chip in terms of noise a multitude of working points need to be set and tested. Since a working point always corresponds to a certain threshold value, the measured fake-hit rate can be plotted versus this threshold value. Usually this is even done alongside the sensor efficiency as it is done in figure 3.4 at the top. Plotting efficiency and noise level both against the chip setting in terms of average in-pixel threshold, it can be tested whether a high efficiency could also be achieved by chance due to very high noise levels. For flat ALPIDE chips it is shown that the noise level is extremely low over a wide range of threshold settings. Thus, the measured high sensor efficiency is very unlikely to be caused by noise [5, 47].

Threshold scan Due to the digital nature of the ALPIDE chip the charge threshold setting on the in-pixel discriminator is the determining factor of the chip performance during an experiment. In section 3.2 and figure 3.2 it is described that this threshold and hence also the working point of the entire chip can be set using a set of DAC values. The ones having a direct impact on the threshold are ITHR, VCASN and IDB. Since the nominal ALPIDE chip has already been extensively characterised and optimised, only ITHR and VCASN are varied in order to change the threshold setting. IDB is kept at a default value and VCASN2 is set depending on VCASN for all practical purposes like beam tests and other experiments.

For the sensor characterisation it is therefore crucial to link the chip settings, i.e. the set DAC values, to the corresponding physical charge threshold inside a pixel. This is done during a *threshold scan* using analog pulsing as described at the end of section 3.2. With the help of a pulsing capacitance C_{inj} a known amount of charge Q_{inj} can be injected in a pixel according to equation 4.3.

$$Q_{\text{inj}} = C_{\text{inj}}(\text{VPULSE\_HIGH} - \text{VPULSE\_LOW}) \tag{4.3}$$

Here, VPULSE_HIGH and VPULSE_LOW are illustrated in figure 3.3 and are each limited at $1.8\,\text{V}$. Since these voltages are controlled by DACs, there is a minimal voltage step of $7\,\text{mV}$ per DAC count by chip design. Taking into account the injection capacitance to be $C_{\text{inj}} = 230\,\text{aF}$, this leads to a possible charge injection in steps of $10e$. For the threshold measurement the basic principle is to subsequently inject increasing amounts of test charge Q^i_{inj} and detect when the pixel of interest starts registering a hit.

To be more precise, for each test charge step Q^i_{inj} a number of N_{inj} injections are performed out of which N^i_{hit} lead to a registered hit in the pixel. Therefore, $N^i_{\text{hit}}/N_{\text{inj}}$ gives the hit probability

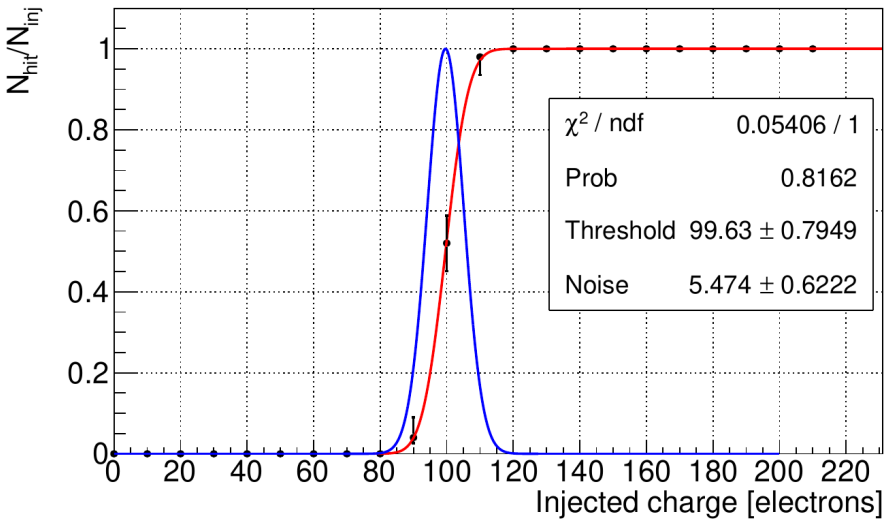

Figure 4.7 Hit probability of a single ALPIDE pixel $N_{\text{hit}}/N_{\text{inj}}$ with respect to the amount of injected test charge Q^i_{inj}. The black data points are fitted with an Gaussian error function (red line) in order to determine the threshold value for the pixel. The electronic noise is assumed to be Gaussian and is plotted as the derivative of the hit probability (blue line). In this particular example the threshold of the pixel of interest is close to $100e$ [5].

of a pixel at charge step Q^i_{inj}. Since a hit is only registered when the charge threshold of the pixel is overcome, a step function is expected when plotting this hit probability versus the amount of injected charge. However, the contribution of electronic noise in the pixel, which is represented by the derivative of the hit probability, causes the edges of the step function to be smoothened out. As the electronic noise can be assumed to be Gaussian, the hit probability P_{hit} can be fitted by a Gaussian error function as in equation 4.4.

$$P_{\text{hit}}(Q) = \frac{N_{\text{hit}}}{N_{\text{inj}}} = \frac{1}{2}\left(1 + \text{erf}\left(\frac{Q-\mu}{\sqrt{2}\sigma}\right)\right) \tag{4.4}$$

Here, μ denotes the found threshold value for the tested pixel as it is defined as the charge at which the pixel *fires* in $50\,\%$ of the injections. Additionally, σ represents the *temporal noise* of the pixel, since it is related to the width of the electronic noise distribution. An example of such a threshold determination for a single pixel is shown in figure 4.7. In this case the found threshold for this specific pixel would be $(99.63 \pm 0.79)e$. The threshold measurement can either be repeated subsequently or even be performed in parallel for a larger number of pixels in order to find a representative threshold value to characterise a full ALPIDE chip. Performing the threshold measurement for all pixels yields a threshold distribution, which can be seen on the left in figure 4.8. For all practical purposes, especially for plotting sensor results, the average of all measured single pixel threshold values is used to describe a chip.

On the right of the same figure the corresponding distribution of the temporal noise of the single pixels is shown. According to equation 4.4 and figure 4.7 it can be understood as the distribution of the single pixel threshold uncertainties. In this example, but also in general, it is observed that the mean value of the noise is significantly lower than the root mean square (RMS) value for the threshold distribution. In particular this means that the pixel-to-pixel differences are the main contribution to the uncertainty of the average threshold value. For this reason only the width of the threshold distribution is taken into account when estimating the threshold uncertainty for a full ALPIDE chip. Unlike temporal noise, which is of statistical nature, pixel-to-pixel differences

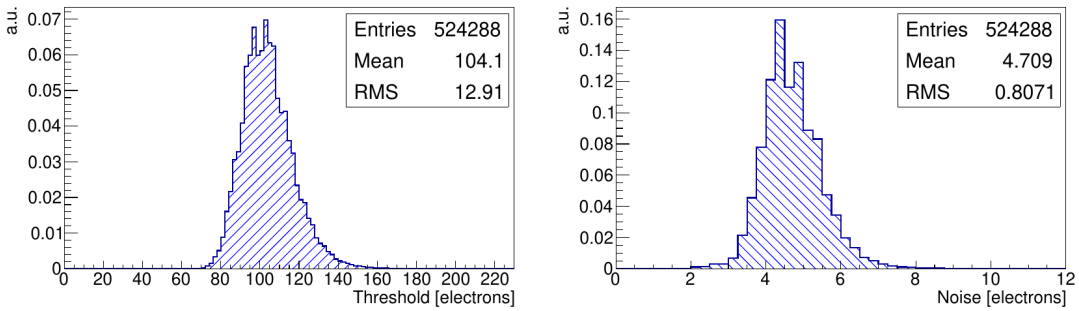

Figure 4.8 **(left)** Distribution of all single pixel threshold values for an entire ALPIDE chip. Consequently, there are as many entries as pixels on the chip. The mean value is used to characterise this specific chip in terms of an average threshold per pixel [5].
(right) Distribution of all single pixel temporal noise values for an entire ALPIDE chip. Consequently, there are as many entries as pixels on the chip. It can be seen that the mean value of the noise is smaller than the threshold RMS value [5].

result from transistor and biasing differences in the implemented in-pixel electronics. Therefore, the width and shape of the threshold distribution is mainly caused by *fixed pattern noise* (FPN), since pixel-to-pixel variations occur in a stable pattern throughout the pixel matrix in this case.

During beam tests the objective usually is to perform an in-beam characterisation of the DUT for a wide range of settings or working points. In the case of the testbeam campaigns done for this work this especially means testing the bent ALPIDE chips for different threshold settings by varying the parameters ITHR and VCASN. For both beam tests at DESY in June and August 2020 the tested parameter space is visualised in figure 4.9 on the left and on the right panel respectively. In both cases there was no back-bias voltage $V_{\mathrm{BB}} = 0\,\mathrm{V}$ applied to the DUTs, which also affects the measured threshold values of the sensors.

It is clearly visible that for the beam test in June 2020 the maximum sensible and possible parameter space is tested. This includes 8 different settings of ITHR and up to 10 different values for VCASN resulting in a threshold range of approximately $15e$ to $300e$. Furthermore, it can be seen that with increasing ITHR also the threshold increases as described in section 3.2. On the contrary, the threshold decreases for higher values of VCASN in a fashion that could be described with a second-order polynomial. However, the lines shown in the plots only serve as an eye guide and do not represent a fit.

The same behaviour of the measured threshold values can be observed for the beam test in August 2020 in the right panel of figure 4.9. However, it is obvious that the tested parameter space is much smaller as compared to the one for June. The tested settings include only three ITHR settings and up to 12 values for VCASN. The resulting thresholds are roughly in a range of $50e$ to $320e$. There are two major reasons for the smaller tested parameter space. First, the ITHR parameter not only has an impact on the threshold, but also on the pulse length of the in-pixel analog signal. Since the DUT in the August testbeam could only be connected and readout via the slow control interface it is decided to only test ITHR settings close to the nominal value of $\mathrm{ITHR} = 51\ \mathrm{DAC\ counts}$ [21]. Secondly, there was a tighter time schedule for this testbeam campaign than for the one in June, which required to cut down on the parameter space to be tested.

Additionally, it has to be mentioned that sensor settings leading to thresholds much below $50e$ have been tested, but are discarded for the analysis due to a significantly increased noise level for the DUT, which was already observed during data taking. Since this problem did not show up for the DUT in June, it is attributed to the different kind of connection for the chip as described section 4.2 and especially in section 4.2.2. Due to the resulting high sensor occupancy

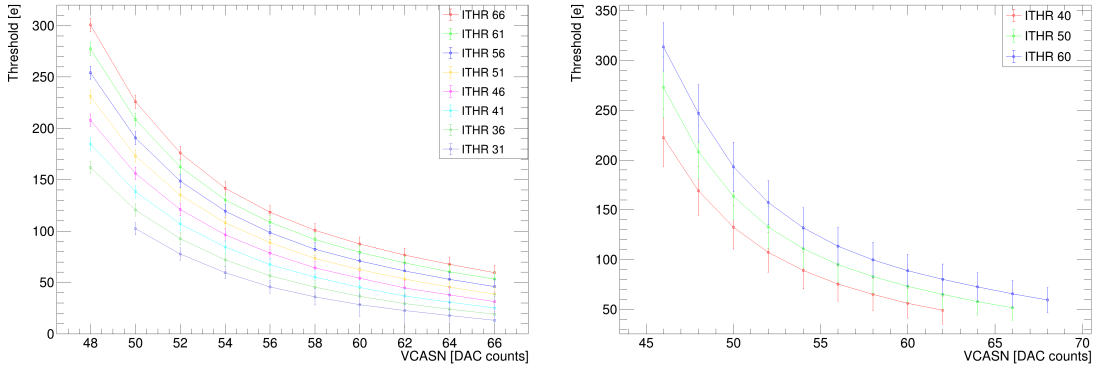

Figure 4.9 **(left)** Tested parameter space for the testbeam campaign at DESY in June 2020. Each set of parameters VCASN and ITHR corresponds to a certain average threshold and thus a working point of the DUT. No back-bias $V_{\mathrm{BB}} = 0\,\mathrm{V}$ is applied. The measured values for one ITHR setting (different colours) are connected by simple lines, which serve as an eye guide. **(right)** Tested parameter space for the testbeam campaign at DESY in August 2020. Each set of parameters VCASN and ITHR corresponds to a certain average threshold and thus a working point of the DUT. No back-bias $V_{\mathrm{BB}} = 0\,\mathrm{V}$ is applied. The measured values for one ITHR setting (different colours) are connected by simple lines, which serve as an eye guide.

this leads to a longer readout period and thus a much lower data taking rate. Furthermore, the size of the corresponding raw data files is increased such that the computing time for the subsequent analysis is tremendous. Hence, it is decided that these data sets are not worth the effort to be included for the analysis presented in this work. In particular the knowledge gain in terms of sensor performance is anyhow limited with respect to a very high noise count for the DUT.

A detailed discussion of the threshold measurement for bent ALPIDE chips and especially the comparison with a flat sensor is given in chapter 6 on the performance of the bent DUTs. There, also the impact of the threshold measurements and sensor settings on the sensor performance is explained.

4.5 Data aquisition

In order to take data in a testbeam experiment a *data aquisition framework* is required. It serves the main purpose of collecting the data from all involved detectors and writes it to disk in a certain format. Each detector, in particular the beam telescope planes and the DUT, is read out by dedicated electronics. In the scope of this work the readout is done with proprietary DAQ boards, which are described in section 4.2. The data stream produced by each of the sensors then needs to be joined, eventually converted to a different data format and written to a *raw data file* for further analysis. Moreover, a DAQ framework coordinates the different detectors connected to a testbeam setup. This especially involves starting and stopping the data taking process as well as controlling the data flow by monitoring readout and writing processes via log messages.

For all testbeam campaigns concerning this work the widely used DAQ framework *EUDAQ* is chosen. It is a modular and versatile framework, which has been developed since 2005 within a project funded by the European Union (EU) and also giving the framework its name. Written in modern C++ it supports a wide range of operating systems and platforms. As a DAQ framework especially designed for the use in testbeam campaigns, it provides support and easy integration of high-precision beam telescopes utilising pixel detectors. In order to perform the task of data taking EUDAQ consists of several modular instances each communicating with each other via the network using Transmission Control Protocols and Internet Protocols (TCP/IP) [49][50].

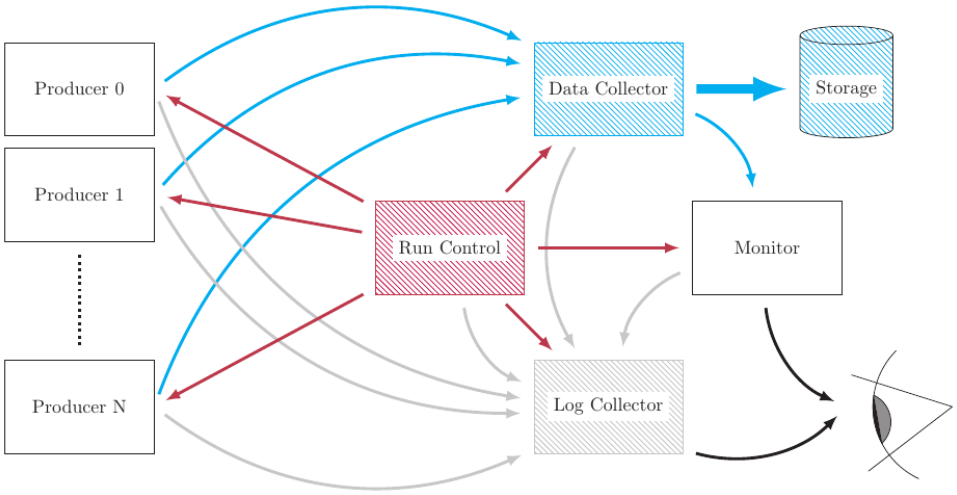

Figure 4.10 Schematic illustration of the main components and processes within the EUDAQ data aquisition framework. There are three major tasks highlighted with different colours. Controlling instances are red, everything linked to data taking and writing is denoted in blue and monitoring instances are grey [49].

The EUDAQ framework can be broken down into three basic process classes, which are illustrated in figure 4.10. First of all there is the *controlling* task shown in red. The responsible EUDAQ instance is a central *Run control*, which acts as the user interface of the DAQ system. A continuous data taking period, also referred to as *run*, can be started or stopped via the Run control. Furthermore, configuration and initialisation files in order to set the working points of the detectors are given to the Run control as user input. During the data taking process the Run control receives the status of each connected process and sends back according commands. As such, this instance centrally steers the entire DAQ system.

Secondly, there are the so-called *Producers* as the source of the *data taking and writing* channel of EUDAQ. Each data producing instance connected to the DAQ system, namely the (ALPIDE) sensors and DAQ boards, are controlled by a separate Producer as shown on the left in the sketch. Since these instances are the bridge between the user-specific hardware and the DAQ software, Producer modules need to be written for every type of detector involved. Due to the modular structure of the EUDAQ framework each Producer needs to provide a standardised output to the rest of the framework. It directly communicates with the hardware and thus is able to initialise the corresponding detector as well as start and stop the sending of data on demand from the Run control. In particular, one *event* should be send per *trigger* signal, whereas the synchronisation of the trigger for multiple devices needs to be dealt with on a hardware level as described in section 4.3. Hereby, each event consists of a set of status information, such as *run number*, *trigger number* and *timestamp* followed by the unprocessed binary output from the sensor [49, 50].

The status part of the data is referred to as *header* and provides the means to organise events sent from different Producers. All data sent by the Producers is then received by the *Data collector*. The information of each detector is then sorted and organised according to the header information. For example the position of the detector, which can be encoded as a plane number by setting jumpers on the corresponding DAQ board, plays a role. As such a *EUDAQ event* is built for each trigger, which in the end can be written to storage in a *raw data file*. Consequently, such a data file is nothing more than a serialised collection of detector raw data organised in (EUDAQ) events [49, 50].

Besides the data sent by the Producers also *log messages* are sent for monitoring purposes. Denoted in grey, the log messages are received and processed by the *Log collector*. As such it serves as a central instance for the user to monitor the status of the entire DAQ system as well as all its single components. If errors or any unexpected behaviour occurs it is displayed there and the user can take action accordingly.

Once written to file the data can be checked by the user in terms of certain quality aspects. For this task EUDAQ offers a *Monitor* module, which can be used in an online or offline fashion. In online mode it is also connected and controlled via the Run control and reads back the data from the file that is currently written. For the offline mode the raw data file has to be passed as an argument to the Monitor application. In both cases standard plots are produced from the data and for instance giving a first insight on detector alignment or hit positions. The monitoring of data is extensively described in section 4.6 using the example of both testbeam campaigns performed for this work.

For the development of the ALPIDE sensor several testbeam campaigns were performed already relying on EUDAQ for data taking. Consequently, the user-specific implementation of an ALPIDE Producer, as well as other required software to decode the ALPIDE binary data already existed for EUDAQ and was adapted for the investigation of bent chips. This is especially the case for the first testbeam campaign with a bent ALPIDE chip in June 2020. Here, EUDAQ linked with the required ALPIDE-specific software was used for data taking.

For the following testbeam campaign in August 2020 the firmware for the DAQ boards underwent an update, which also triggered the change of the DAQ system to the latest development stage of EUDAQ, which is generally referred to as *EUDAQ2*. While the basic architecture and working principle as described before stayed the same, EUDAQ2 was almost entirely rewritten and now adds more flexibility to the DAQ system as compared to its predecessor. Being an even more versatile DAQ framework, EUDAQ2 makes it easy to implement a multitude of different detector types. As such the framework is suitable and efficient to use with even more than one bent ALPIDE sensors as DUTs [51].

4.6 Data monitoring and quality check

Both versions of the used data aquisition framework *EUDAQ* as well as the testbeam data analysis framework *Corryvreckan*[4] offer tools to perform a first rudimentary analysis of the data taken during a testbeam experiment for monitoring purposes. These tools are of major importance during a testbeam campaign as they provide a data driven approach to manually align the involved detectors with respect to each other. Furthermore, the data quality can be checked by visualising and correlating the hit information of every involved detector. The monitoring tools can either be used online, i.e. reading back the data file that is currently written, or offline, where the raw data file is read after the DAQ system finished to write the file for one run.

The first step of a testbeam experiment is to place the setup, i.e. the beam telescope with the DUT, in the beam and align all involved detectors with respect to each other. Looking on the beam telescope in beam direction, the detectors should be aligned such that the beam hits them perpendicularly and that each detector is hit by the same particle at the same position. To have a first representation of the alignment a so-called *hitmap* can be produced for each detector. It illustrates the accumulated hit positions, i.e. column (x) and row (y) number, for a selected run.

A representative hitmap of the bent ALPIDE chip and one exemplary run from the testbeam campaign in June 2020 is shown in figure 4.11. Every registered pixel (px) hit on the DUT during

[4] See section 5.1 for a detailed description of the Corryvreckan framework.

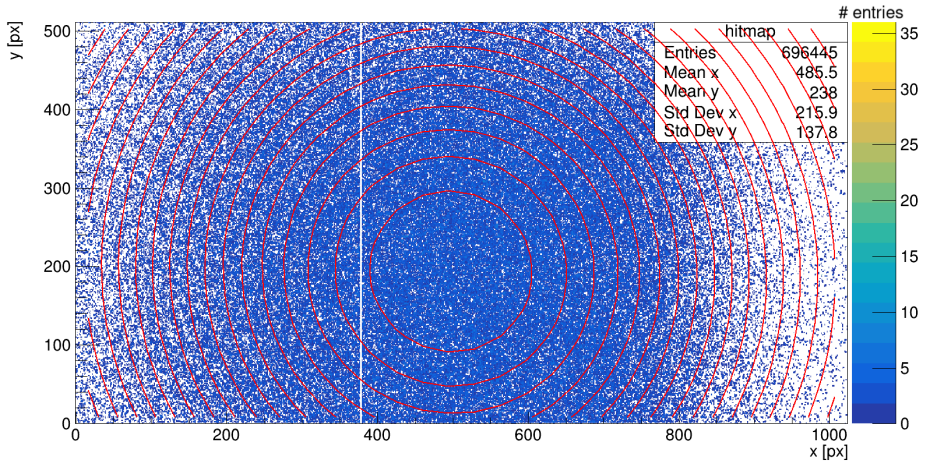

Figure 4.11 Two-dimensional accumulated hitmap for the bent DUT (ALPIDE_3) used in the June testbeam campaign in order to visualise the manual detector alignment with respect to the beam. The multiplicity of a pixel hit is denoted by the colour scale. Red lines represent a two-dimensional Gaussian fit in order to highlight the centre of the beam spot.

the selected run is shown as one entry in the two-dimensional coordinate matrix, which represents the full ALPIDE sensor active area. As such the *beam spot* can clearly be seen on the sensor area. Assuming the beam profile to be Gaussian a two-dimensional Gaussian fit is performed on the data in order to highlight the centre of the beam spot. In this case the represented ALPIDE chip is already sufficiently well aligned in the sense that the beam spot is roughly centred on the detector and hence almost the full sensor surface is illuminated. For a more precise information on the alignment the x- and y-projection histograms of the detector hitmaps can be used to achieve a more precise detector alignment with respect to the beam. If the beam spot is shifted according to the hitmaps, either a single detector or the full beam telescope position can be adjusted by mechanically moving or turning them in the right direction or around the indicated axis in order to counteract the misalignment. Moreover, it can be seen that one double column, namely double column 13 in chip region 11, is masked and therefore visible as vertical line showing no entries[5]. Such inoperative double columns or pixels are often referred to as *dead*.

After the alignment is done it is of major importance to perform quality checks on the data taken in order to ensure that it is readable and hence analysable. Furthermore, it can be directly observed whether the measured signals of the detectors are as expected or can be attributed to a malfunction or misalignment. For this purpose each monitoring tool produces so-called *correlation plots*. Their basic idea is to relate one measured coordinate of a particle hit on one detector plane to another. In order to exploit the available statistics this is done for all registered particle hits on an event-by-event basis for one entire run. In the case of an ideal alignment, where the same particle basically hits every detector in the beam telescope at the same position, this leads to a straight line through the origin, which is referred to as *correlation line* in the following.

Exemplary correlation plots for one representative run measured during the June testbeam campaign is shown in figure 4.12. The chosen run features a sensor threshold value of the DUT close to the nominal value of 100e. Moreover, the two panels show the correlation of both coordinate directions, i.e. column numbers (col) and row numbers (row) of the registered hits. As such both panels represent the full dimensions of the ALPIDE sensor, namely 1024 pixels (px) in column and 512 pixels (px) in row direction. In both cases the hit coordinates registered by

[5]See section 4.2.1 for further information on the DUT for the June testbeam campaign.

the first reference plane of the beam telescope, which is denoted by the subscript *ref*, are plotted against the corresponding ones of the bent DUT.

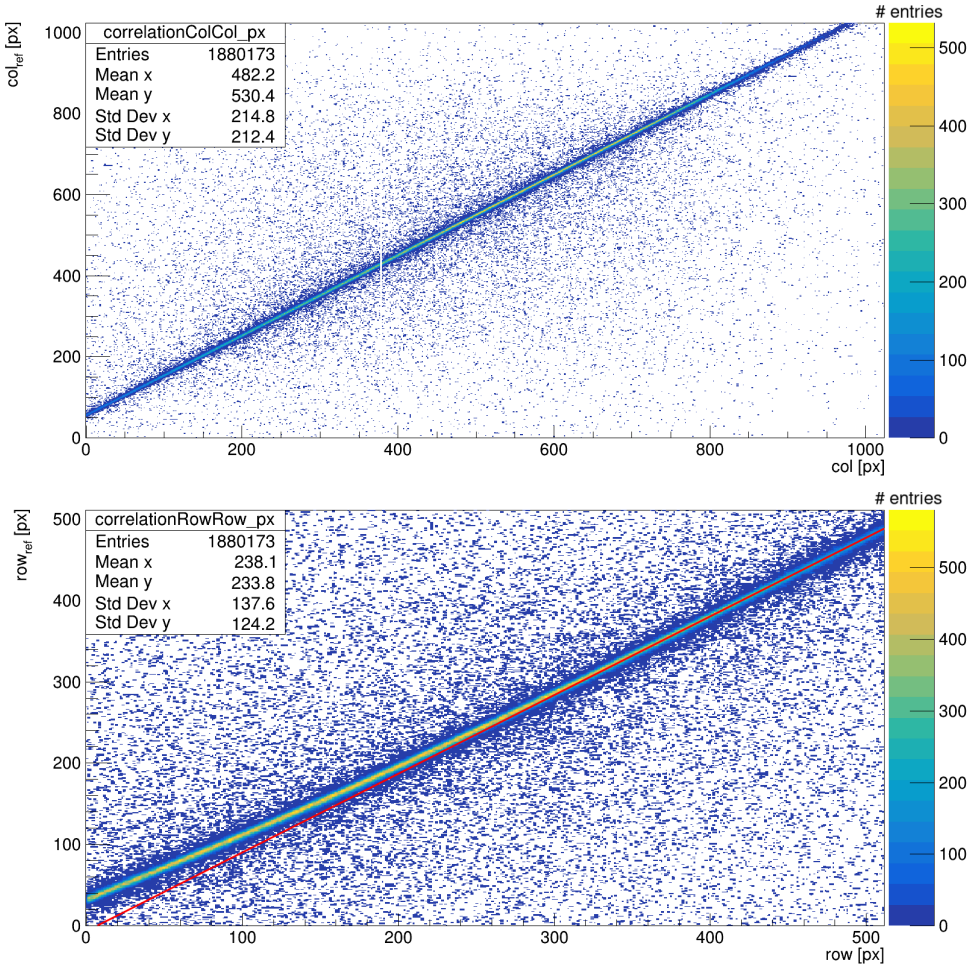

Figure 4.12 **(top)** Hit positions in column direction (non-bent chip axis) of the first reference plane (ALPIDE_0, ref) correlated with the corresponding position registered by the DUT (ALPIDE_3). Due to the alignment of both represented ALPIDE chips with respect to each other a clear line can be seen. The offset of the correlation line from the origin is caused by residual misalignment of the two detector planes. Furthermore, a not working double column is visible around column number 380. The number of entries per pixel column is represented by a colour scale.
(bottom) Hit positions in row direction (bent chip axis) of the first reference plane (ALPIDE_0, ref) correlated with the corresponding position registered by the DUT (ALPIDE_3). Due to bending of the DUT distances in row direction are contracted leading to a curvature in the correlation line. The red straight line highlights the curvature for the correlations, but does not represent a linear fit. The number of entries per pixel row is represented by a colour scale.

The top plot of figure 4.12 shows the column-column coordinate correlation of this kind. Since this is the non-bent direction of the intrinsic chip coordinates a standard behaviour of the resulting correlation line is expected. Assuming that a beam particle traverses the telescope perpendicularly and hits the first sensor at column number 200 it is expected that this particle also hits the DUT at around the same column position. Since the mechanical alignment of the telescope cannot be done with infinite precision, it is expected that the detectors are slightly shifted with respect to each other. For this is a systematic effect, it applies to the full range of coordinates and hence results in

a shifted correlation line. This effect can clearly be observed for the column-column correlation line in the corresponding plot. In this case, the offset of the straight line is approximately 50 pixels, which corresponds to a mechanical misalignment of the two involved detectors of the order of $50 \cdot 29.24\,\mu\mathrm{m} \approx 1.5\,\mathrm{mm}$ in column direction[6]. Again, the vertical line representing no entries around DUT column number 380 can be seen, which is attributed to the dead double column as described before.

Additionally, there are several entries, which are far off the correlation line. These data points can be caused by double or even multiple hits on the sensor. If two or more hits are registered within the same event all possible combinations of the hits on the two involved detectors are considered for the correlation plot. Consequently, multiple hits per event lead to a so-called *combinatorial background*. Besides the systematic shift of the entire correlation line caused by detector misalignment and this combinatorial background, also the scattering of the particle in between the two involved detectors can lead to a shift in the coordinate positions. Given the low material budget of the testbeam setup[7] and the high beam momentum, scattering cannot not cause very large shifts. However, being a statistical process the effect of scattering causes the broadening of the correlation line and is thus represented by its width.

All the above effects can also be observed for the correlation of the other coordinate direction, which is shown in the lower panel of figure 4.12. To be more precise, the row number of the hit registered by the flat reference plane is plotted against the row number of the same hit registered by the bent DUT. According to figure 4.3 a large row number corresponds to a particle hit in the chip area close to the region where the DUT is glued to the carrier card. Consequently, the beam hits the DUT roughly perpendicularly. The lower the row number of the hit, the bending of the chip leads to an increasing inclination of the beam with respect to the DUT sensor surface. As a result lower row numbers for the DUT correspond to a higher actual position as compared to a flat ALPIDE chip, i.e. the reference planes in the beam telescope. In the sense of the correlation of row numbers this leads to a curved correlation line as it can be seen in the plot. For better visualisation of the curvature a straight line is drawn in red as an eye guide. This result marks the first proof of a functional bent ALPIDE sensor registering particle hits from a testbeam. Additionally, similar plots for the other runs of the testbeam campaign in June revealed that the taken data is indeed analysable and already shows the expected behaviour of the involved ALPIDE chips, especially including the bent sensor.

Similar to the data checks described above for the testbeam campaign in June 2020 also the data taken in the subsequent testbeam campaign in August 2020 is also monitored using hitmaps and correlation plots. Due to the different bent axis and thus the alternative mounting of the DUT[8], the column direction for the reference planes is now equal to the row direction for the DUT, while the reference row direction is the same as the reverse DUT column direction. This corresponds to a rotation of $270°$ of the DUT with respect to the reference planes around the beam axis. In order to observe sensible coordinate correlations this has to be taken into account.

The top panel of figure 4.13 shows the correlation of the reference column number with the DUT row number of all hits during one exemplary run. Again a run featuring a DUT sensor threshold value close to the nominal value of $100e$ is chosen as example. Taking into account the rotation of the DUT the involved sensors do not overlap in their full active area, but show a squared region of overlap. Consequently, there are regions on the reference, where there is no corresponding hit registrable on the DUT and vice versa. Having this in mind, a clear correlation of the measured hit position can be seen in the form of a straight and sharp correlation line as

[6] The testbeam setup is sketched in figure 4.3 and coordinate systems are illustrated in figure 5.1
[7] Basically several layers of ALPIDE sensors with $0.05\,\%\,\mathrm{X}_0$ ($50\,\mu\mathrm{m}$ Silicon) each [19]
[8] As illustrated in figure 4.4 and figure 4.5

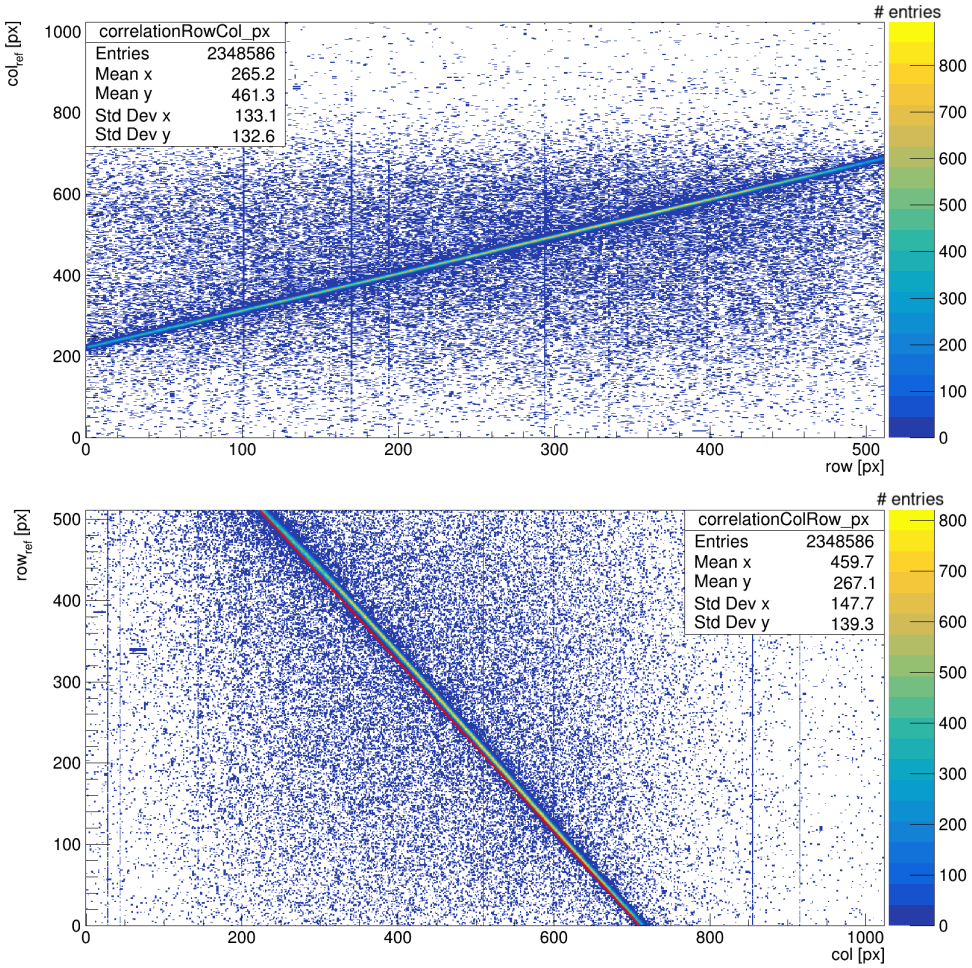

Figure 4.13 **(top)** Hit position correlation of column number for the first reference plane (ALPIDE_0, ref) with the row number registered by the DUT (ALPIDE_3). For the DUT is rotated by 270° with respect to the reference planes, the correlation line can only be seen for the overlapping region of the involved ALPIDE chips (reference column number 200 to 700). The number of entries per column and row is represented by the colour scale. **(bottom)** Hit position correlation of row number for the first reference plane (ALPIDE_0, ref) with the column number registered by the DUT (ALPIDE_3). For the DUT is rotated by 270° with respect to the reference planes, the correlation line can only be seen for the overlapping region of the involved ALPIDE chips (DUT column number 200 to 700). To make the slight curvature of the correlation line visible a straight red line is drawn as a eye guide and reference. The number of entries per column and row is represented by the colour scale.

expected. It can be seen that the full width of the DUT overlaps with the region on the reference chip roughly ranging from column numbers 200 to 700. As this coordinate direction represents the non-bent case, no deviation from a straight line is visible for the correlation line.

The case of the bent coordinate direction for the DUT is shown in the lower plot of figure 4.13. Here, row numbers of hits measured on the first reference plane are correlated to the corresponding column number on the DUT. Again a clear correlation can only be observed in the overlapping regions of the involved sensors. In this case the full width of the reference chip overlaps with the region on the DUT between column numbers 200 and 700. As described above the rotation of the DUT leads to a clearly visible sign flip in the slope of the correlation line. Furthermore, in comparison with the straight red helper line a slight effect of the chip curvature can be seen. However, it is not as pronounced as for the DUT used in the June testbeam campaign.

This can be attributed to the altered geometry of the testbeam setup. In June the DUT basically started parallel to the reference planes and was bent out of this plane towards lower row numbers. This leads to a maximum absolute inclination angle between beam direction and sensor surface normal. Consequently, the largest deviation from a straight correlation line can be seen for the lowest row numbers in this case. For the August testbeam campaign the bent DUT appears to be *flat* regarding the correlation plot at the column number, where the corresponding tangential plane is parallel to the reference planes. This is true for column numbers roughly corresponding to the middle of the overlap region with the reference planes. Going towards lower or higher column numbers results in a increasing total inclination angle between beam direction and sensor surface normal. Therefore, the maximum deviation from a flat sensor correlation is reached at the edges of the overlap region. Since the distance from the tangential point to these edges is roughly only half of the correlation range, the net curvature effect is significantly smaller than in the case of the June testbeam campaign.

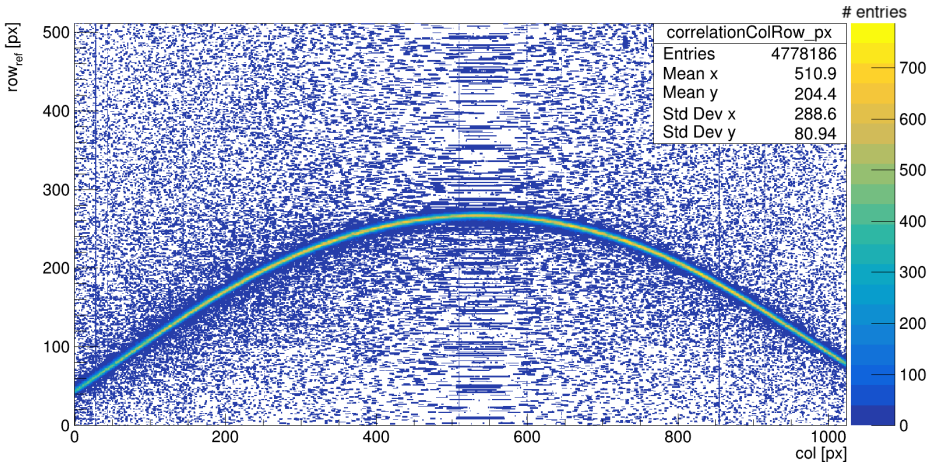

Figure 4.14 Hit position correlation of row number for the first reference plane (ALPIDE_0, ref) with the column number registered by the DUT (ALPIDE_3). In this case the bent DUT is mounted in double crossing configuration, such that the same testbeam particle can penetrate through the sensor twice. The testbeam enters the *sensor cylinder* at high column numbers and exits at low column numbers. Consequently, for each row hit on the flat reference two corresponding column hits on the DUT can be seen if the reference and DUT position overlap. This leads to a extremely curved correlation line. The number of entries per column and row is represented by the colour scale.

In both correlation plots of figure 4.13 vertical patterns in the combinatorial background can be identified. They are caused by single pixels that are likely to fire. It might be the case that pixels in this specific rows and columns have a significantly lower threshold than the sensor average and are thus more prone to fire due to noise. Despite this fact, the correlations plots of all runs from the August testbeam campaign indicate good data quality[9].

A very special case of a correlation plot is achieved with the double crossing configuration of the DUT during the August testbeam campaign. In this setup geometry the DUT is rotated such that the same beam particle can hit the sensor twice. This ultimately demonstrates the cylindrical shape of the DUT. The corresponding correlation plot of reference row numbers and DUT column numbers for one exemplary run is shown in figure 4.14. It is clearly visible that the curved correlation line resembles the bent sensor surface of the DUT. Particles of the testbeam first hit the DUT at high column numbers when *entering* the *detector cylinder*. A second hit is

[9]For completeness an exemplary hitmap is shown in figure A.3 in section A.3 at the end of this document to demonstrate sufficiently good mechanical alignment of the DUT with respect to the beam.

registered at low column numbers when the particle *exits* the cylinder. In the overlap region of the involved detectors there are two corresponding column hits for each hit row in the first reference plane of the beam telescope. The tangential point around column number 550 on the DUT plays a special role. Here, the beam traverses the sensor parallel to its surface, i.e. along the epitaxial layer. Thus, a particle leaves a long trace of charge behind, which leads to significantly elongated clusters of hit pixels. As such this configuration allows to probe the epitaxial layer by making use of these so-called *grazing particle events*. However, this is subject to further research and thus beyond the scope of this work.

5 Testbeam data analysis

In order to investigate the performance of a sensor, which was used as DUT in a testbeam campaign, the gathered data must be analysed. In general, the analysis strategy can be split into several stages, which are described in more detail in the following sections. First, so-called *noisy* or *hot* pixels must be masked. In this stage, badly behaving or broken pixels are identified and will be ignored for the subsequent analysis steps. As already indicated in section 1.5, the same particle can trigger more than one pixel to register a hit. These adjacent hit pixels are grouped in a *cluster*. The cluster position can be calculated as the (weighted[1]) mean position of the hit pixels. All further analysis is based on these cluster positions. The second analysis stage is the software-based alignment of the beam telescope. Here, particle tracks are reconstructed only using the information from the reference detectors. Based on these tracks the reference detectors are then virtually shifted and rotated to reach an optimal track quality. After this the DUT is separately aligned in the third stage with a different track-based approach. For this step it is crucial to keep the already aligned reference detectors fixed at their respective positions. With everything aligned the actual analysis can be done for the DUT as the final stage. Now the quantities of interest, such as sensor efficiency and position resolution can be calculated on the basis of built pixel clusters and reconstructed tracks.

5.1 The Corryvreckan analysis framework

For the scope of this thesis and the work in the associated research group the analysis framework *Corryvreckan* is used in order to analyse data from several testbeam campaigns performed at the DESY testbeam facility. The development of the Corryvreckan framework is a rather recent undertaking with the first official version having been released in 2019 [52]. It has been mainly developed and is maintained by M. Williams[†], J. Kröger[‡], L. Huth[§], P. Schütze[§] and S. Spannagel[§] with contributions from a multitude of authors from many different institutes.

Named after a whirlpool off the west coast of Scotland's mainland, the Corryvreckan framework is specifically designed to address the reconstruction and analysis of testbeam data. It is written in modern C++ and due to its modular structure it is highly versatile and easily extendable. Especially these qualities make Corryvreckan the natural choice for the data analysis task connected to this project, since here a new generation of bent pixilated detectors has to be introduced as described in section 5.8. The *standard* version of Corryvreckan, which served as basis for the implementation of a bent sensor geometry inside the framework, is available in the official Corryvreckan git repository[1] [53].

To perform its task Corryvreckan features the `corry` executable, which is called together with a configuration file that specifies which and in which order the different Corryvreckan modules

[1] If charge information or more details on the produced cluster shapes is available.

[†] University of Glasgow, CERN

[‡] Heidelberg University, CERN

[§] DESY

[1] Official Corryvreckan git repository:
`https://gitlab.cern.ch/corryvreckan/corryvreckan`

are executed. It is obvious that the first module needs to be of *event loader* type to read the raw data from its file into the framework. Based on the trigger and timestamp information events are built from the data stream. Here, Corryvreckan features a flexible and user configurable event building instance that directly allows to process triggered (and untriggered) and timestamped data from different data acquisition systems and different detector types if needed. The further processing of data in the following modules is then done on an event-by-event basis. For each analysis stage Corryvreckan has to be run with a separate configuration file as input. The several analysis stages performed for this project are detailed in the following sections.

5.2 Corryvreckan coordinate systems

In order to perform the analysis of testbeam data, the Corryvreckan framework relies on several coordinate systems, which are shown in figure 5.1. All of them are chosen as right-handed Cartesian coordinate systems, where the z-axis represents the beam direction. Primarily, these coordinate systems can be divided into two groups, namely *local* and *global*. There are two kinds of local coordinate systems, which describe points on the surface of a detector. Hence, two separate coordinate systems are attributed to each detector relevant for the data analysis. Additionally, one global system is used in order to relate the local coordinates for each relevant detector in the testbeam setup. This system is of major importance for the software based alignment procedure of different detectors with respect to each other as described in section 5.5 and 5.6. In the following a motivation and detailed explanation of the different coordinate systems is given.

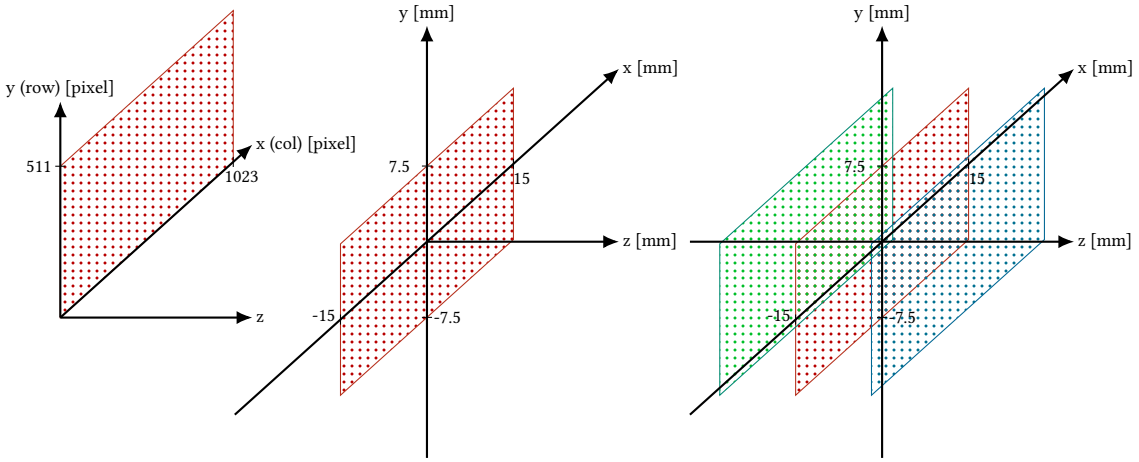

Figure 5.1 Sketch of the three right-handed coordinate systems used within the Corryvrechan framework. As a reference the dimensions of an ALPIDE chip are denoted in red for each of the cases. There are two local and one global system. Local chip coordinates are described with column (col) and row numbers (left). A conversion of these local coordinates to a chip-centered mm-based system leads to the second local system (middle). The global system, chosen to be centered at the DUT (red), correlates all the local systems (right). Two exemplary reference detectors are shown in green and blue.

From the raw data the position information of a hit pixel is only available as its address. Therefore, the first local coordinate system has its origin in the lower left corner of the chip. The *column* (col) number and the *row* number of the hit pixel are displayed on the x-axis and y-axis, respectively. Thus, the described detector surface always lies inside the x-y-plane, independent of the fact if the real detector surface is bent not. For this reason, the z-coordinate is conventionally set to the constant value of zero independent of the x-y-position of the hit as illustrated in figure 5.1 on the left.

Given the pixel pitch δ and the number of pixels N_{pix} on the detector in both directions, the column-row coordinates can be converted to a mm-scale according to the equations 5.1. Since column and row numbers start from 0 by design choice, the number of pixels has to be decreased by one to account for that. The factor $1/2$ ensures that the resulting local hit position represents the centre of the pixel. The derived second local coordinate system is therefore centred in the chip middle as it can be seen in figure 5.1 in the middle. Moreover, all z-coordinates are left at a value of zero hence the described sensor still lies inside the x-y-plane.

$$\begin{aligned} x_{\text{local}} &= \frac{\delta(x_{\text{col}} - N_{\text{pix,col}} - 1)}{2} \\ y_{\text{local}} &= \frac{\delta(y_{\text{row}} - N_{\text{pix,row}} - 1)}{2} \end{aligned} \tag{5.1}$$

Having converted the hit positions to physical units, i.e. millimetres, it now makes sense to also describe other positions on the sensor surface. For instance the position of a cluster of adjacent hit pixels is represented by the mean value of the single pixel coordinates. Consequently, this can result in positions in between pixels, which cannot be intuitively understood in the sense of integer column and row numbers. Furthermore, this local coordinate system serves as the basis for the implementation of bent sensor geometries as presented in section 5.8.

A global reference point is necessary in order to relate the local coordinate systems for different detectors to each other. It can be freely chosen and is passed to the Corryvreckan framework via a geometry configuration file. As a convention, the initial chip centre of the DUT is chosen as reference point, to which a z-coordinate value of zero is assigned. Here, initial refers to the initial mechanical alignment declared to the Corryvreckan framework via the geometry file. As illustrated on the right of figure 5.1, this point is well defined for flat sensors. However, for bent geometries, where the sensor also extends in z-direction, further clarification is needed. For this purpose the figures 4.3 and 4.5 show the global z-axis and the corresponding global x- and y-direction for the testbeam campaign in June and August, respectively. The distances between the remaining detectors needs to be measured by hand for example using a sliding calliper. With this information a global coordinate frame can be built in software.

In order to add a detector to the global coordinate system the measured z-coordinate is added to the respective local coordinates. On top of that, the corresponding local coordinate system can be translated in all three global directions and rotated around all three coordinate axes according to the geometry information given in the configuration file. In software this is realised by applying a transformation matrix to a coordinate vector. In order to convert from local coordinates to the global frame and vice versa the functions `localToGlobal` and `globalToLocal` are implemented in Corryvreckan and play a major role when treating non-standard detector surfaces for instance curved sensors.

5.3 Event building and event loaders

With DESY playing an important role not only in providing testbeams, but also driving software developments all around this topic, Corryvreckan naturally features modules to read and process data written by the EUDAQ and EUDAQ2 data aquisition frameworks, which are described in section 4.5. As described before, EUDAQ requires a user modification to internally convert the binary data sent by the detector to a so-called *Standard Event*. Thus, the binary data format written to the raw data file can be converted back to the standardised EUDAQ specific format and then be read into Corryvreckan using the `EventLoaderEUDAQ` or `EventLoaderEUDAQ2`

module, respectively. The raw data is firstly read plane-by-plane and secondly event-by-event. Hence, the timing information on the first processed detector plane defines the beginning, end and duration of the corresponding *Corryvreckan Event*. Now the information of each hit pixel, such as position, collected charge and time over threshold (no analoge information for ALPIDE), is copied to the so-called *Clipboard*, which is a temporary event storage allowing all modules of Corryvreckan to access this data for further processing. The transfer of data to the Clipboard is only made, if the timing information of the current plane matches the one of the Corryvreckan event.

By default, the event building process for the EUDAQ event loader modules is based on timestamp information, which worked flawlessly for the data of the testbeam campaign in June 2020. There, EUDAQ built together with ALPIDE specific software to decode the data from the sensors was used for data acquisition. However, with the switch to EUDAQ2 and new firmware for the FPGA on the DAQ boards it was not possible to read the data with the specific Corryvreckan module. A detailed investigation of this issue revealed a large shift of the timestamps between hits on different detector planes within the same Standard Event. Therefore, Corryvreckan fails to assign hit information from different detector planes to the correct Corryvreckan event. In fact, only the data of the first plane is transferred to the Clipboard and all the subsequent planes are ignored, because they do not match the time frame of the Corryvreckan Event.

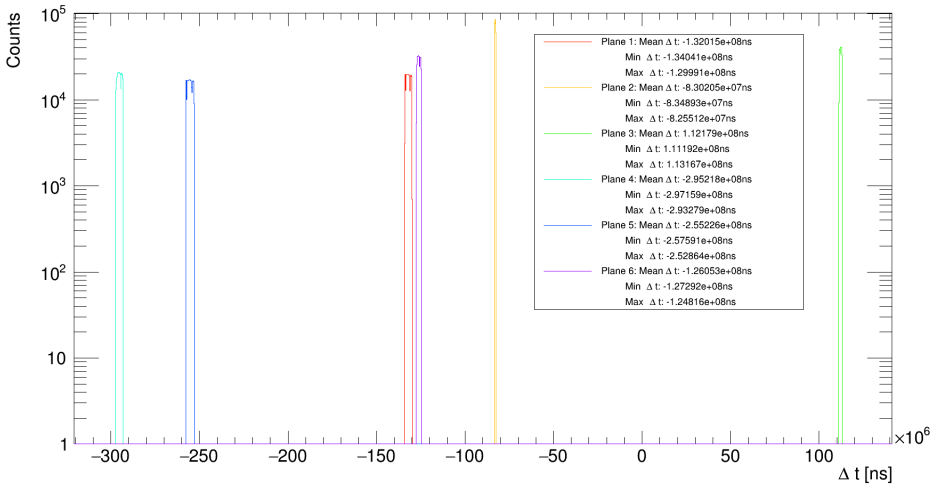

Figure 5.2 Relative timestamps (timestamp differences) with respect to detector plane 0 taken from EUDAQ2 for one exemplary run from the DESY testbeam campaign in August 2020. Different detector planes are shown in different colours. Additionally, the minimal, maximal and mean timestamp shift per plane is displayed.

Figure 5.2 shows timestamp information taken from EUDAQ2 for one exemplary run in the DESY testbeam campaign in August 2020. It is clearly visible that the timestamps show a large offset with respect to the first detector plane (plane 0) and also with respect to each other. In an ideal case the timestamp differences are expected to show a narrow peak very close to $0\,\mathrm{ns}$. An attempt to solve this issue by subtracting the measured mean time offset with respect to the reference plane from the corresponding timestamp proved not to be successful due to the width of the timestamp difference distributions. The precision of this correction is not sufficient to ensure the correct assignment of Standard Event hit information to the corresponding Corryvreckan event during one entire run. This is especially true considering multiple runs.

The width of the timestamp difference distributions is caused by a mismatch of the clock frequencies for different DAQ boards. Ideally, each DAQ board clock giving the timestamp

information should *tick* at a frequency of 80 MHz. However, due to hardware variations each clock has a slightly different frequency leading to a time offset between the planes for each clock cycle. As a consequence these differences accumulate with time resulting in the drifting timestamp differences shown in figure 5.2. Additionally, the DAQ board clocks start at different times as they are not synchronised by an external stimulus.

In order to overcome the event building problems for EUDAQ2 in this case Corryvreckan is forced to only consider the trigger number for the assignment of hit information from different detector planes to a Corryvreckan event. As described in section 4.3 the trigger identification number (ID) is common to all detector planes. Only relying on this kind of timing information for the event building process the data transfer from EUDAQ2 to Corryvreckan is successful for the August testbeam dataset. In the subsequent data analysis there is the limitation that no sensible timing information is accessible in order to reconstruct the particle trajectories. However, this has no impact on the analysis performed in the scope of this work.

5.4 Masking of noisy pixels

Due to material damage or defects introduced during the manufacturing process of the detector chip there might be single pixels or even full double columns showing a significantly lower in-pixel threshold. This in turn leads to an increased hit rate of the concerned pixels caused by electronic noise. Moreover, there might can be other effects rendering the pixel to falsely fire, i.e. detecting a hit without an external stimulus. Such *noisy pixels* affect the data analysis for instance in the track reconstruction process. Consequently, they can bias or at least negatively influence the results concerning the sensor performance. It is therefore of major importance that noisy pixels are identified in the first stage of the data analysis process. For all subsequent steps they need to be ignored.

In Corryvreckan this is taken care of by the `MaskCreator` module. For this work pixels are classified as noisy with the *frequency method*. During an entire representative reference run a global average pixel hit rate is calculated for each detector. In the next step the hit rate of each single pixel is compared to this sensor average. In case a pixel fired f_{cut} times more than the sensor average it is recognised as noisy and its address is written to a *mask file*. Here, f_{cut} is called the *frequency cut* parameter, which can be specified in the main configuration file to initialise Corryvreckan and its modules [52]. In the scope of this work a frequency cut of 1000 is chosen, which is a rather high value considering the fact that ALPIDE proved to be a sensor featuring very low noise levels as it can be seen in figure 3.4. Thus, only extremely noisy pixels, firing at least 1000 times more than an average pixel on the sensor, are excluded from the further analysis.

For each detector a separate mask file is produced. These files are read back by the event loader modules at the beginning of any further analysis stage. Therefore, they can also be edited by hand, if for instance a laboratory test reveals a noisy pixel or chip region. Moreover, pixels already listed as masked are maintained, i.e. the mask files are appended if they already exist during the *mask creation stage* of the full data analysis process.

5.5 Software-based prealignment of the beam telescope

As already mentioned in section 4.6 the mechanical alignment of the beam telescope and the DUT has its limitations. Even using data driven methods, for instance the described monitoring tools in order to identify misalignment, most probably there will still be a remaining misalignment. Due to limitations in the positioning methods for the detector planes this cannot further be accounted for

by mechanically shifting and rotating the affected detector planes[2]. For this reason *software-based* methods have to be applied in order to align the detectors to a precision that reasonable data analysis can be performed. This especially refers to a good quality of reconstructed particle trajectories, i.e. *tracks*, passing through the setup. As such the alignment task is very crucial, since already a misalignment of a single plane with respect to another by a fraction of a millimetre for instance can correspond to a shift of several pixel pitches. Consequently, the reconstructed particle tracks are significantly distorted, i.e. they will most probably not describe the actual particle trajectory very well. Thus, such *bad* tracks affect or bias the analysis results based on them.

Within the Corryvreckan framework the overall alignment task is split into two stages, namely *prealignment* and *alignment*. This section further describes the prealignment stage, while the alignment stage is presented in the following section. For either of these two cases a configuration file containing basic geometry properties of the setup is required. Especially the (x,y,z)-position of each detector plane, as well as their rotation angles with respect to each coordinate axis of the global coordinate frame are the important quantities for both alignment stages. While x- and y-coordinate can be set to initial values, usually $0\,\mathrm{mm}$, the z-coordinate has to be measured by hand. After each alignment stage or iteration an updated geometry file is produced by Corryvreckan. It contains the updated and improved geometry found during the alignment. This means that virtual shifts and rotations for each detector plane improving the overall alignment are calculated and written to this file. At the beginning of each (data analysis) stage with Corryvreckan, the geometry file is read in and each detector plane is shifted and rotated with respect to its initial position according to the values given in the file. This is done by applying a transformation matrix.

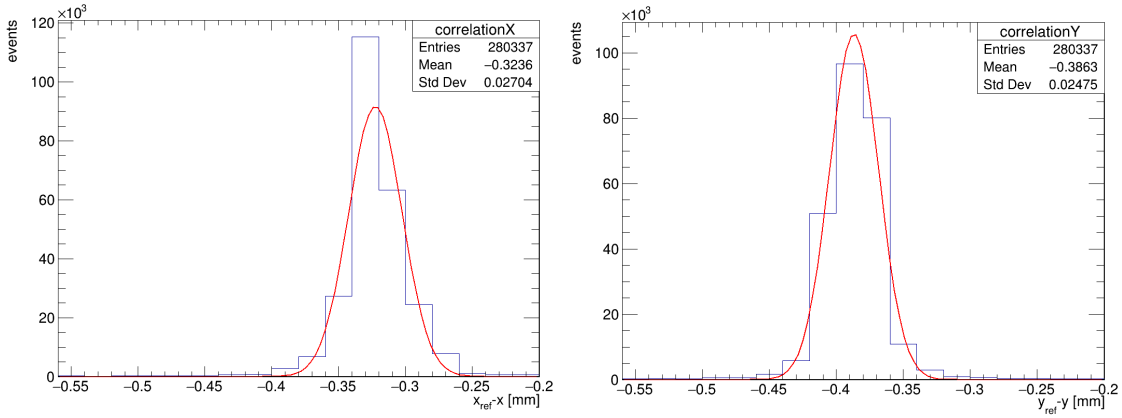

Figure 5.3 One-dimensional exemplary correlation of the hit coordinates on the reference detector plane (ALPIDE_0) and the second beam telescope plane (ALPIDE_1) in both coordinate directions. The respective distribution (blue) is fitted by a Gaussian (red). The data represented is for one representative run of the August testbeam featuring a sensor threshold of close to $100e$ for every detector plane.
(left) x-coordinate of the reference plane subtracted by the corresponding x-coordinate on the correlated detector plane.
(right) y-coordinate of the reference plane subtracted by the corresponding y-coordinate on the correlated detector plane.

The main objective of the prealignment stage is to provide a first solid, but not yet high-precision, software-based alignment of the testbeam setup, which serves as the basis of the subsequent higher precision alignment stage. As such, no tracking information is used during

[2]For this work this had to be done by hand.

the prealignment stage. Independent of its role, i.e. reference or DUT, the prealignment can be performed simultaneously for each detector plane. Furthermore, only shifts in the x- and y-coordinates are considered, while rotations are subject to the precision alignment. The global z-coordinate is kept fixed at the measured value given in the geometry file.

In order to quantify the misalignment of the detector planes with respect to each other, one plane is chosen as *reference*. For every case in this work the first plane of the beam telescope in beam direction, i.e. ALPIDE_0, acts as this reference. Now all the other detectors are virtually aligned in relation to this plane. For this reason the one-dimensional hit coordinate correlations are used in order to identify the values of the respective x- and y-shifts. Figure 5.3 exemplarily shows this hit coordinate correlations between the reference and the second plane of the beam telescope, ALPIDE_1. In order to determine the shift for the prealignment, a Gaussian is fitted to the distribution of the hit coordinate differences between the involved detector planes in both, x- (left) and y-direction (right). The shifts applied to the respective planes is then determined by the mean value of the fitted Gaussian. It can be seen that in the example given in figure 5.3 ALPIDE_1 is virtually shifted by $-0.32\,\mathrm{mm}$ in x- and $-0.39\,\mathrm{mm}$ in y-direction within the global coordinate frame. Calculating and applying these shifts to each of the corresponding detector planes of the testbeam setup results in an improved (virtual) detector alignment as compared to the purely mechanical alignment performed during the testbeam campaign.

In Corryvreckan the module used to perform this task is called `Prealignment`. This module also offers more methods for the calculation of the coordinate shifts [52].

5.6 Software-based alignment of the beam telescope

After *coarse* shifts of the detector planes have been identified and accounted for in the prealignment stage, a precision alignment is performed using this improved setup geometry as input. For this reason, not only translations, but also rotations, of the detector planes are considered in order to achieve an optimal alignment result. Here, an insufficient initial setup alignment might cause the algorithm implemented for calculating the virtual translations and rotations to not converge.

From corresponding hits in subsequent layers, the particle trajectory can be reconstructed by fitting these spatial points with a certain track model. Here, a straight line in three dimensions is the simplest example of such a track model. Since these tracks serve as a reference for the later analysis in order to evaluate the performance of the DUT as described in section 5.9, it has to be explicitly excluded from the track fitting process. If not only the hit information from the reference planes, but also the DUT hit information is used to build a track, the analysis results would be biased. As such the DUT has to be aligned separately, which is further discussed in section 5.7.

The alignment of the remaining beam telescope planes is realised by optimising the χ^2 distribution of the track fits taking into account a sufficiently large set of reconstructed tracks. Here, a large value of χ^2 indicates large deviations of the measured spatial points to the fitted track. If χ^2 is divided by the number of degrees of freedom (ndof), which is given as the number of fitted points (3 translational directions per point) subtracted by the fit parameters constrained by the model, it is referred to as reduced χ^2, i.e. χ^2_{red}. A value of $\chi^2_{\mathrm{red}} = 1$ indicates that the data points are perfectly described by the fitted model. Thus the χ^2_{red} distribution can be considered as a measure of the goodness of the setup alignment. A good alignment is characterised by a χ^2_{red} distribution peaking at low values, since the tracks are supposed to be optimally described by the track model when reaching a setup geometry corresponding to the actual detector positions during the testbeam experiment.

An example of the χ^2_{red} distribution before (left) and after an alignment step (right) is shown in figure 5.4. Before the alignment step, a large fraction of tracks is not well described by the track model which is visible by a broad distribution featuring large values of χ^2_{red}. It is clearly visible that the overall χ^2_{red} values shift to lower values due to an improved detector alignment. Here, the majority of tracks are well described by the track model.

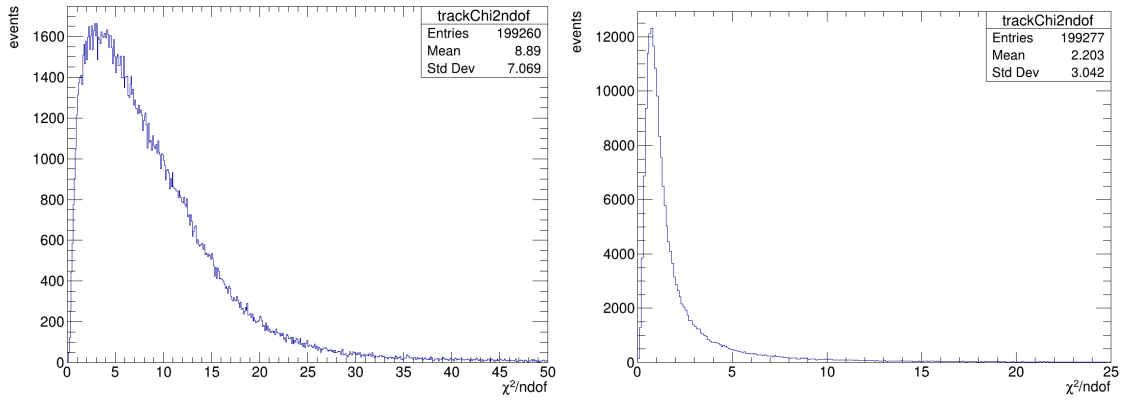

Figure 5.4 **(left)** Exemplary χ^2_{red} distribution before an alignment step for a representative run of the August testbeam. A large fraction of the tracks is not well described (large χ^2_{red} values) by the track model due to bad alignment of the reference planes with respect tot each other. **(right)** Exemplary χ^2_{red} distribution after an alignment step for a representative run of the August testbeam. It has to be noted that the horizontal axis features only half the value range as compared to the left distribution. As such it is an example of a good alignment of the reference planes with respect to each other. The majority of tracks is well described by the fitted track model.

For the scope of this work, the track-based alignment is performed by the `Alignement Millepede` module. As the name suggests, it features an implementation of the *Millepede* algorithm, which allows for the simultaneous fit of the track and the chosen alignment parameters [52]. Since the z-positions are kept fixed at the measured values given in the geometry file, each reference sensor of the beam telescope can be translated in x- and y-direction and rotated around the local x-, y- and z-coordinate axes. The algorithm stops if a specified convergence level is reached. The alignment parameters corresponding to this found optimised alignment of the beam telescope reference planes are updated in the geometry file and kept fixed for future reference.

5.7 Including the device under test

With the fixed optimised alignment of the beam telescope, also the DUT needs to be aligned with respect to the reference planes. Also for this case a track-based approach is followed. Having the track information from the beam telescope at hand[3], the distance between the track interception point with the DUT sensor surface x_{track} and the corresponding particle hit position on the DUT can be calculated. As further discussed in section 5.9, this is referred to as (track) residual. If the reconstructed track and the associated hit on the DUT originate from the same traversing particle, it is expected that the absolute value of the residual is minimal in the case of a good DUT alignment. A deviation from 0 is caused by the limited position resolution of both the DUT and the sensors contributing to tracking. Moreover, a larger residual value is measured if the considered particle is scattered by the detector material.

[3]Still the DUT is excluded from the track fitting.

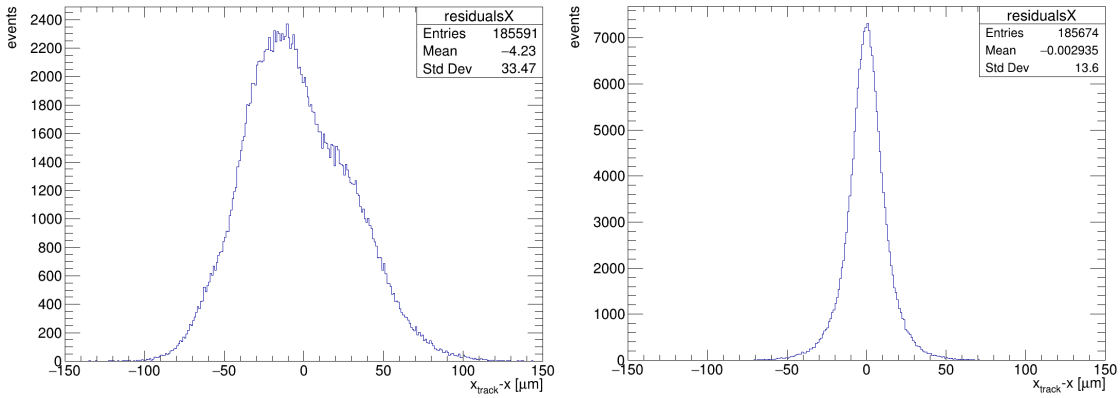

Figure 5.5 **(left)** Exemplary residual distribution for the DUT in x-direction before the software-based alignment is applied. It can be seen that the distribution is very asymmetric, which is a strong effect of the bent sensor surface in convolution with the fact, that the sensor is not yet aligned. The underlying data corresponds to a representative run of the August testbeam campaign.
(right) Exemplary residual distribution in x-direction after the software-based DUT alignment is performed. The resulting distribution is centred around 0, became narrower and resembles a Gaussian shape. The underlying data corresponds to a representative run of the August testbeam campaign.

Since the scattering of particles is a statistical process, the residual distribution for the DUT is expected to be Gaussian considering both x- and y-direction. Furthermore, it should be centred around 0 for a good DUT alignment. Figure 5.5 shows exemplary residual distributions in x-direction for the bent DUT and a representative run in the August testbeam. The left panel represents the situation before the *DUT alignment* stage, while the right panel shows the residual distribution after the DUT is aligned by optimising the unbiased residual distribution.

Regarding the case before the DUT alignment the residual distribution is very broad and extremely asymmetric. This is caused due to the bent sensor surface. Extending in all three spatial dimensions a misalignment of the DUT, especially if rotations are involved, has a large effect on the corresponding residuals. Furthermore, it can be seen from the mean value that the distribution is not centred at 0. However, after the alignment is performed by virtually shifting the DUT in x- and y-direction as well as allowing for rotational degrees of freedom around all three local coordinate axes, the residual distribution gets narrower, is centred around 0 and is of Gaussian shape. A similar effect is observed for the residuals in y-direction. In Corryvreckan this kind of alignment procedure is realised within the `AlignmentDUT` module [52].

5.8 Implementation of a curved sensor geometry

A priori, the state of the art official version[4] of the Corryvreckan testbeam data analysis framework does not support curved sensor geometries. Hence, in the framework of this research project cylindrical sensor geometries have to be implemented in Corryvreckan. This allows to perform data analysis for both bent ALPIDE chips described in section 4.2.

The information of the reconstructed particle trajectories has to be compared to the particle hit information on the DUT in order to evaluate its performance as it is further described in the following section. It is obvious that a track as a global object relies on the global coordinate system, while the measured signals on the DUT are a local quantity in the first place. For this

[4]Version v2.0 (May 2021)

reason especially the two functions transforming coordinates from the local coordinate frame to the global one and vice versa need to be modified. As described in section 5.2 these are `localToGlobal` and `globalToLocal`. In order to realise this, the new detector class `BentPixelDetector` is added to the standard Corryvreckan framework. It features the modified coordinate transformation functions, which can be selected by specifying the coordinate system to be *cartesian-bent* for the DUT. The general idea of implementing the bent sensor is to first transform from the flat local coordinate system, to a local-bent one. In a second step the usual translations and rotations according to the geometry configuration file are applied to the local-bent coordinates thus transforming them to the global frame.

For the bent DUT in the June testbeam the row coordinate corresponding to y_{local} describes the bent direction. Therefore the arc length a_{y} on the bent surface in row direction is given as

$$a_{\text{y}} = \frac{d_{\text{y}}}{2} - y_{\text{local}} \tag{5.2}$$

where d_{y} is the dimension of the active chip area in row direction. There initially was the idea to allow for a flat part y_0 in the bent geometry implementation accounting for the part of the bent DUT, where the chip is glued to the carrier board[5]. Consequently, if a_{y} is smaller than the specified value of y_0 the standard transformation from local to global coordinates is applied. In the other case a cylindrical geometry featuring the bending radius r is obtained by

$$\begin{aligned} x_{\text{bent}} &= x_{\text{local}} \\ y_{\text{bent}} &= -r \sin\left(\frac{(a_{\text{y}} - y_0)}{r}\right) + \frac{d_{\text{y}}}{2} - y_0 \\ z_{\text{bent}} &= r \cos\left(\frac{(a_{\text{y}} - y_0)}{r} - 1\right) + z_{\text{global}} \end{aligned} \tag{5.3}$$

The transformation from global back to the local frame is simply the inverse operation. For the August testbeam campaign featuring the bent DUT on a cylindrical jig[6], no flat part is needed in the implementation of the corresponding bent sensor geometry. With the bent axis representing the column direction and following the same nomenclature as above it follows

$$\begin{aligned} a_{\text{x}} &= x_{\text{local}} \\ x_{\text{bent}} &= r \sin\left(\frac{a_{\text{x}}}{r}\right) = r \sin\left(\frac{x_{\text{local}}}{r}\right) \\ y_{\text{bent}} &= y_{\text{local}} \\ z_{\text{bent}} &= z_{\text{global}} - r\left(1 - \cos\left(\frac{a_{\text{x}}}{r}\right)\right) = z_{\text{global}} - r\left(1 - \cos\left(\frac{x_{\text{local}}}{r}\right)\right) \end{aligned} \tag{5.4}$$

The second modification required in order to have a fully functional implementation of a bent sensor geometry within the Corryvreckan framework is the calculation of a track intersection point with a cylindrical sensor surface. For this purpose, the simplest case of a track, i.e. a straight line, is considered. In the three global spatial dimensions it is defined by a starting point called *state* and a *direction vector*. In order to calculate the global track intercept, a rotation matrix is applied to the global cylindrical coordinates such that the cylinder axis is parallel to one of the coordinate axes. Accordingly, the same rotation must be performed for the direction vector of the track. Now the coordinates can be projected to a plane perpendicular to the cylinder axis. As such, the incept problem has been transferred to a two-dimensional intersection of a circle

[5] See figure 4.2
[6] See figure 4.4

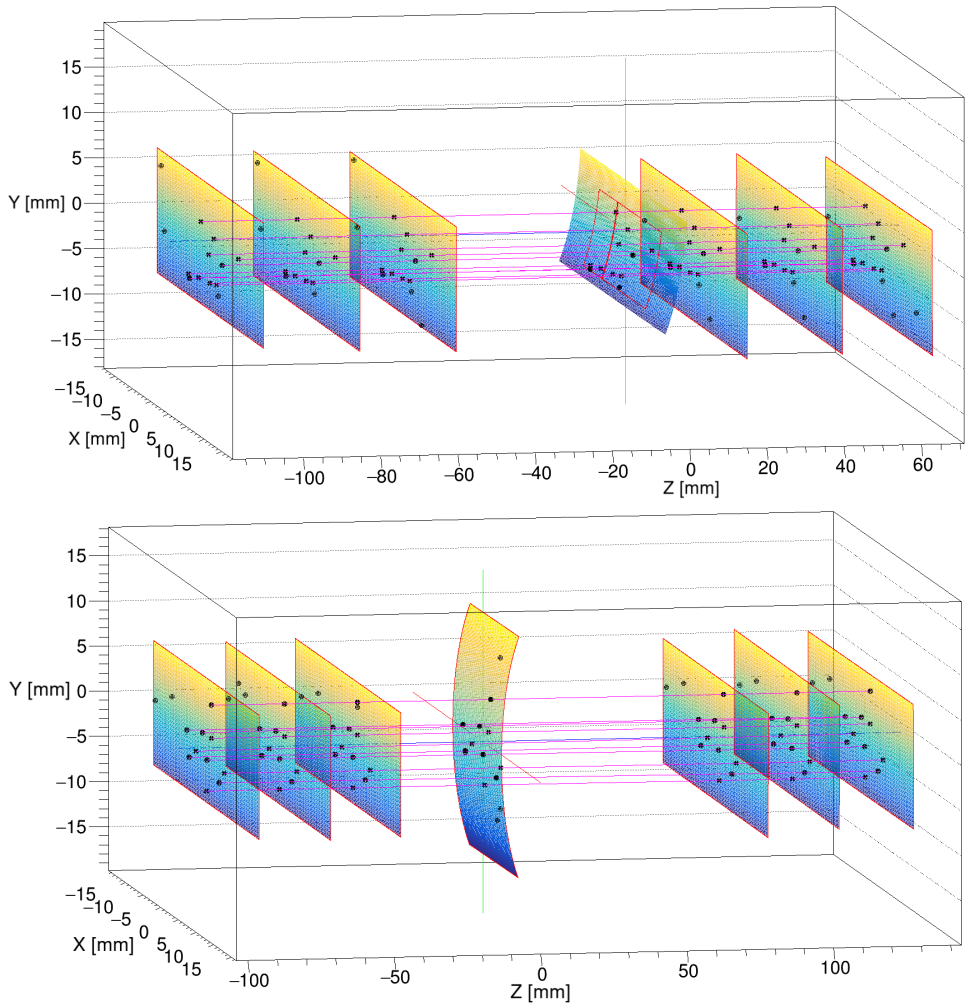

Figure 5.6 Event displays illustrating the aligned beam telescope and bent DUT for both testbeam campaigns. The coordinate axes represent the global Corryvreckan coordinate system. All ALPIDE sensors are represented by a grid of points, where the hight (y-coordinate) is colour-coded. The ROI is illustrated by a red frame. 10 events of a representative run of the respective testbeam campaign are overlaid. Open symbols represent raw cluster positions, while filled symbols represent associated cluster positions and track intercepts. The straight-line tracks are denoted by pink lines.
(top) The data represented is gathered during the testbeam campaign in June 2020.
(bottom) The data represented is gathered during the testbeam campaign in August 2020. It can be seen that the DUT is rotated by 270° with respect to all the other detector planes.

and a straight line, which can be solved by a quadratic equation. Since this might yield two real solutions, it has to be made sure that the right one, i.e. the one lying on the bent sensor surface, is selected. At this point, the full 3D solution for the track intercept can be obtained by going back to the original global geometry and propagating the track to the bent sensor surface using the 2D results.

Since this approach is general, it can be applied for both previously presented cases, namely the June and August testbeam campaigns. However, for June is has to be checked beforehand if the track intercept lies in the flat part of the bent sensor. In this case the track is simply propagated until it hits this flat sensor part. This is equivalent to the standard procedure performed within the imlementation of flat sensors.

In order to verify that the implemented bent geometry actually represents the physical, aligned testbeam setup an event display can be considered. For both testbeam campaigns, i.e. June and August, the corresponding sensor geometries are plotted in figure 5.6 at the top and at the bottom, respectively. The used coordinate system is the same as the global system used by Corryvreckan. Each of the displays feature ten events. The hit information is plotted as black symbols. Here, open symbols represent raw clusters and filled symbols either denote a track interception point or the position of an associated track cluster [7]. Furthermore, reconstructed straight-line tracks are denoted by a pink line. It can be seen that there are sets of raw clusters in both cases, for which no tracks are built. In these cases the reconstructed tracks did not pass the preselection criteria applied in order to ensure a high track quality and are therefore rejected. In general there are more raw clusters than tracks, since only one cluster is associated to one track per event. If there is a second hit due to another beam particle or noise, it is simply ignored for the further analysis. Also playing a role for the track selection as described in the following section, a region of interest (ROI) is defined and show as a red box for each detector plane. In general, it can be seen that the previously described implementation of a bent geometry indeed provides the functionality for Corryvreckan in order to analyse bent pixelated sensors. A more general implementation of curved sensors is subject of ongoing research.

5.9 Analysis quantities

After all involved detectors, i.e. the reference planes of the beam telescope and the DUT in between, are aligned with respect to each other, the actual *analysis* of the data can be performed in a run-by-run fashion. Since during a batch of runs featuring different working points of the DUT the setup is neither moved nor modified, it is legitimate to assume that the same alignment obtained from one representative run of the batch also applies for all the remaining runs. The precision of the alignment has a large impact on the analysis results. Therefore, the representative run is chosen such that that the DUT is at its nominal working point if known beforehand. In the case of the bent ALPIDE sensors, this corresponds to a run featuring a DUT threshold value of close to $100e$.

The basic idea of a testbeam data analysis is the evaluation of the DUT performance. First of all a track from a testbeam particle traversing the setup is reconstructed using the reference planes of the beam telescope only. The DUT hit information is explicitly excluded from the track fitting algorithm. In the case of this work only electrons with a an energy of $5.4\,\mathrm{GeV}$ were used in both testbeam campaigns. Given their large momentum and the low material budget of the testbeam setup, scattering of the beam particles is considered a small effect. For this reason a *straight-line track model* is reasonable and used for track fitting. In principle, Corryvreckan also supports a general-broken-line (GBL) track model, which accounts for scattering effects [54]. However, how a GBL track is described inside the analysis framework made it difficult to make it compatible with the first implementation of a bent sensor geometry [52].

Having the reconstructed track at hand, some preselection cuts can be applied to ensure that its quality is good. For this work, a found track requires a hit on all 6 reference planes in order to be accepted. Due to the trigger settings described in section 4.3 and the particle rate of the testbeam only one track per event is considered. To further improve the quality of tracks used for the analysis step, tracks can be excluded according to their χ^2_{red} value. Regarding the χ^2_{red} distribution of reconstructed tracks for one entire run, it has been found that requiring a value of $\chi^2_{\mathrm{red}} < 3$ is sufficient to ensure a good track description, i.e. track straightness, while not significantly

[7] In this scale the two symbols are so close that they cannot be distinguished.

decreasing the available statistics. In Corryvreckan, standard track fitting can be done with the `TrackingSpatial` or the `Tracking4D` module [52]. Another way of selecting a set of tracks for the analysis is to define a so-called *region of interest* (ROI) on the DUT. Only tracks featuring an intersection point within these (rectangular) regions are considered for further analysis. As such, they can be used to exclude dead regions of the detector chip.

For the set of high-quality tracks the analysis is then performed by dedicated analysis modules on a track-by-track basis. Within the framework of this work, especially the Corryvreckan modules `AnalysisDUT` and `AnalysisEfficiency` are used. As a starting point of the analysis the intersection point for each track with the DUT sensor surface is calculated. Next, clusters within an elliptic search window are associated to the track with the `DUTAssociation` module. The size of the search window can be chosen by the user and is $100\,\mu\mathrm{m} \times 100\,\mu\mathrm{m}$ for this work. If more than one cluster is found within the fiducial area, by choice only the closest cluster is associated to the track [52]. Based on the track intercept point and the associated cluster positions on the DUT a range of analysis quantities are calculated. The ones relevant for this work are listed and shortly described in the following, while the actual results obtained from the gathered testbeam data in June and August are presented and discussed in chapter 6.

Cluster properties The *size of the associated clusters*, i.e. the number of pixels making up the cluster, is investigated as a first simple quantity. It depends on how much signal charge is generated by the traversing particle. As such it is especially interesting for the case of bent sensors, since more or less charge is produced depending on the beam incident angle on the sensor surface and thus the traversed distance of the particle within the detector material. Furthermore, this quantity is sensitive to the charge collection properties (diffusion and drift) inside the pixels. A more detailed study on this can be done by investigating the respective *shapes of the clusters*. Cluster measurements like this do not necessarily require tracking information from a testbeam data set, but as it is presented in the dedicated section 6.1 they still can profit from it.

Detection efficiency The *detection efficiency* is a central quantity describing the performance of a detector. For each accepted track in the beam telescope a corresponding signal on the DUT is searched. In the case a cluster can be associated the track, it is counted as efficient or matched, if not it is counted as inefficient. The ratio of matched tracks over total accepted tracks represents the detection efficiency of the DUT. The efficiency uncertainty is calculated by applying a *Clopper-Pearson* confidence interval of one sigma. Taking into account the respective upper and lower limit of 1 and 0, this corresponds to the central $68.3\,\%$ of an assumed binomial distribution for a given efficiency [52, 55]. By definition, the detection efficiency strongly depends on the working point and the noise level of the sensor.

Residuals The distance between track intersection point and associated cluster position in each coordinate direction is referred to as the respective (track) *residual*. As such, this quantity is closely linked to the *position resolution* of the DUT. In fact, the standard deviation of the residual distribution $\sigma_{\mathrm{residual,x}}$ represents the convolution of the tracking uncertainty $\Delta x_{\mathrm{track}}$ and the position resolution Δx. As such the position resolution can be calculated according to

$$\Delta x = \sqrt{\sigma^2_{\mathrm{residual,x}} - \Delta x^2_{\mathrm{track}}} \tag{5.5}$$

The tracking uncertainty can be determined by a Monte Carlo simulation of the beam telescope. It follows that the position resolution is generally smaller than the standard deviation of the residual distribution, since for the reference also ALPIDE sensors are used.

Furthermore, the cluster size can be related to the position resolution. For a single pixel cluster featuring only digital information the position resolution is limited by the binary resolution given as $\delta/\sqrt{12}$, given a pixel pitch δ. This represents the worst case scenario. For larger clusters the mean value of the hit pixels and possibly information for a specific cluster shape can be used to reach an improved position resolution for the particle.

6 Performance of bent ALPIDE sensors

The first step in the evaluation of the performance of the bent ALPIDE chips, which were used as DUTs in the two testbeam campaigns described throughout this work, is the measurement of the electrical properties and functionality of the in-pixel and chip circuitry after bending. In this regard, the threshold scan is probably the most important laboratory measurement amongst the ones described in 4.4. Due to its nature, this test exercises the full readout chain, beginning with the analog and digital in-pixel circuity and continuing with the address propagation of a hit pixel to the digital chip periphery for readout. It is thus sensitive to any change or unexpected behaviour in the integrated electronic circuits on top of the ALPIDE chip, which is possibly caused by the bending stress.

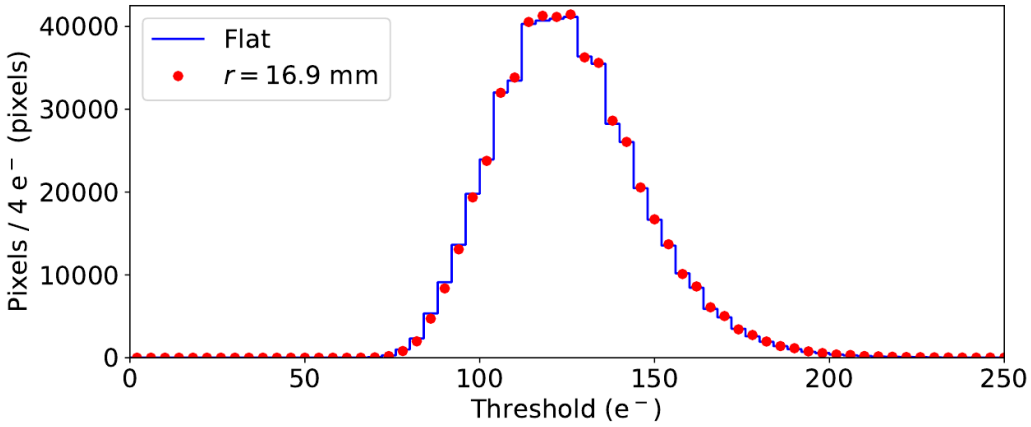

Figure 6.1 In-pixel threshold distribution representing all pixels of the ALPIDE chip used in the June beam test. The threshold measurement is performed before (blue) and after bending (red) the chip to a radius of $16.9\,\mathrm{mm}$. Pixels are grouped in threshold intervals of $4e$ width. For each of these bins either no, or a negligibly small threshold difference between the flat and the bent case can be seen [46].

The threshold of the first bent DUT is measured at INFN in Trieste before and after having it bent to a radius of $16.9\,\mathrm{mm}$[1]. The results of this measurement are shown in figure 6.1. For the flat chip, a typical in-pixel threshold distribution taking into account the entire active area of the sensor is visible as the blue histogram. Such a distribution is expected due to small pixel-to-pixel differences resulting from the manufacturing process. This is understood in the sense of fixed pattern noise as described in 4.4. The sensor threshold characterised by the mean value of this distribution is around $130e$, which is close to the DAC settings for the nominal working point of ALPIDE.

On top of this reference distribution, the measured threshold values for the bent chip are displayed by red points. Considering large threshold values no difference can be seen between the flat and the bent case. However, going towards low threshold values some very small deviation for a few threshold bins are visible. Given their small magnitude and considering the full chip, the changes in threshold before and after bending are indeed negligible. Moreover, this result is a

[1] This is even more than the target radius for the innermost layer of the ITS3 of $18\,\mathrm{mm}$.

strong indication that the functionality of the integrated electronic circuitry is unaffected by the bending.

The threshold is also measured for the bent DUT in the August testbeam, which is bent in the different direction. As such, the chip circuitry is decompressed instead of compressed as it is the case for the June DUT. Due to the different mounting of this DUT on the cylindrical jig, the threshold could not be measured before the bending. However, the plots in figure 4.9 show that similar chip settings (VCASN, ITHR) result in comparable threshold values. For this purpose, it can be assumed that there is also no significant effect on the threshold or the electrical chip functionality by bending the chip in the other direction.

Another important quantity, which influences the analysis results is the fake-hit rate obtained by a noise occupancy scan. In case of the June DUT, the same procedure as for the threshold is followed, i.e. a noise occupancy scan is performed before and after the bending. Again, only negligible differences were observed. Therefore, it can be safely assumed that the fake-hit rate of flat and bent ALPIDE chips is comparable [46]. This result is especially important for the analysis results concerning the detection efficiency as it is discussed in section 6.2.

Futhermore, noise occupancy tests were performed at random during the testbeam experiments. There, it has been discovered that the overall noise level of the August DUT is increased as compared to the one in June. Since this was not seen in laboratory measurements, this finding might be attributed to the connection of the DUT to the DAQ board in the August testbeam. As described in section 4.2.2, no standard carrier card, usually containing decoupling capacitors and resistors to filter electronic noise, could be used. It is therefore assumed that the increased noise is caused by these missing decoupling elements. Despite that fact, it is shown that the resulting increase of the noise level is moderate, i.e. not rendering the chip to be unusable. However, for low threshold values, the chip occupancy was so high that the readout rate and written data size is significantly increased. For that reason, runs featuring a DUT threshold of below $50e$ are not included in the presented data analysis as already discussed in section 4.4.

At the top of figure 3.4 it can be seen that the fake-hit rate for flat ALPIDE sensors basically reaches the sensitivity limit of the noise occupancy scan for high threshold values. Going towards lower thresholds, it is found that below a certain threshold value around $100e$ the noise level starts to increase. As the noise occupancy scans for the June DUT indicate that bending does not significantly affect the noise level, the same overall fake-hit rate trend can be also observed for the August DUT, but already starting to increase at a higher threshold value.

Having ensured that the bending of ALPIDE chips has no significant influence on their electrical functionality, it is legitimate to continue with the actual analysis of the testbeam data. The main analysis quantities, namely cluster sizes and shapes, as well as (in-pixel) detection efficiencies and track residuals giving an idea of the position resolution, are briefly described in section 5.9. A more detailed discussion of them on the basis of the analysis results for both testbeam campaigns is given in the following dedicated sections. There, the focus lies especially on how these analysis quantities depend on the threshold and noise level. It should be kept in mind that, even though performing well, not the highest-quality ALIPIDE chips were used for these first studies of bent CMOS MAPS. Consequently, they might feature a dead double-column like it is the case for the DUT used in June or occasionally firing smaller chip regions, such as only half a double column or even comprising smaller numbers of affected pixels.

6.1 Cluster sizes and shapes

A first observable to study in order to characterise a pixel sensor is the *cluster size* as already briefly introduced in section 5.9. As indicated in section 1.5, a fraction of the primary signal charge generated by a traversing particle can end up and be collected in adjacent pixels. This *charge sharing* is driven by diffusion of the signal charge. It is clear that the cluster size has to depend on the amount of primarily generated free charge carriers. As such, a highly ionising particle is expected to produce larger clusters as compared to a MIP.

The largest fraction of the signal charge is most probably collected in the primarily hit pixel, which is intuitively understandable. The shared charge to an adjacent pixel also has to overcome the in-pixel threshold in order to be registered as a hit. Consequently, the cluster size is expected to be strongly dependent on the sensor threshold. As such a decrease of the cluster size with increasing threshold value is anticipated.

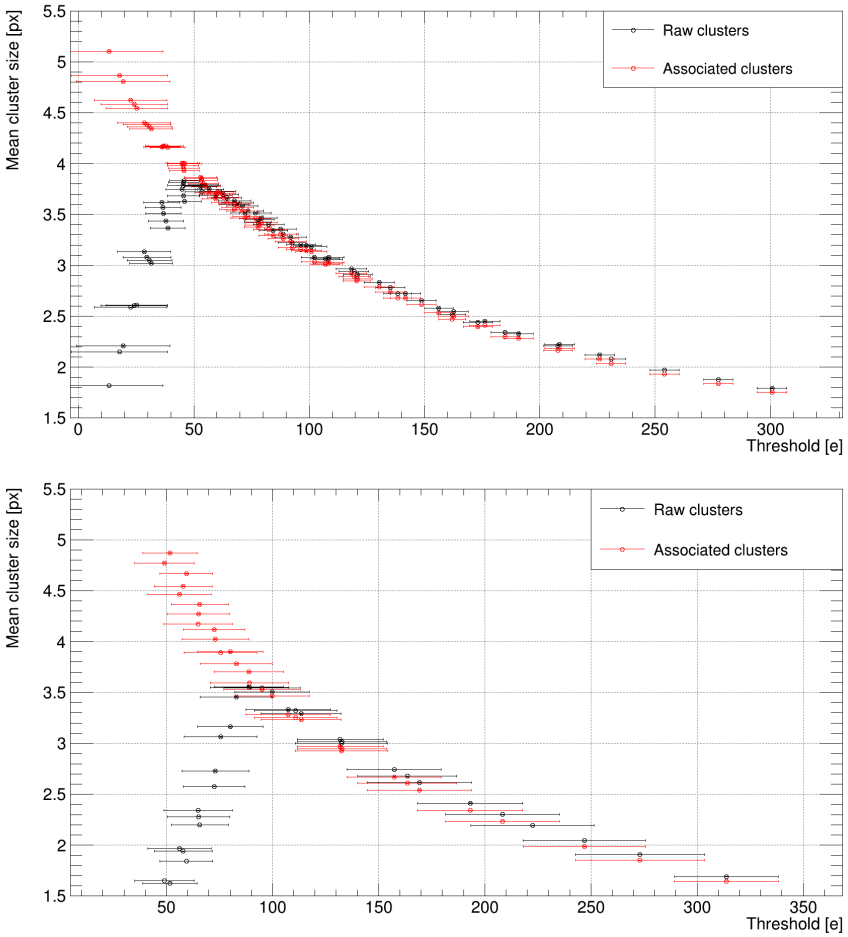

Figure 6.2 Dependence of the average cluster sizes on the DUT threshold. Two different types of cluster sizes are shown. Raw clusters (black) take any kind of cluster information for an entire run (no selection criteria applied) into account. Associated clusters (red) fulfil the criteria to get associated to a reconstructed particle track. Each data point represents one run with a minimum of 300k events.
(top) The represented runs are from the testbeam campaign in June 2020.
(bottom) The represented runs are from the testbeam campaign in August 2020.

This trend can be nicely seen in figure 6.2 for both testbeam campaigns. While runs from the June testbeam experiment are shown in the top panel, the lower one represents data taken during

the August testbeam campaign. Each point in the plots represents the average value of the cluster size distribution for all events of the corresponding run. There are two different average cluster sizes plotted for the respective bent DUTs. Shown in black, the *raw clusters* are the result of the rudimentary clustering algorithm, which simply groups adjacent hit pixels. As such, these kind of cluster sizes are unbiased, i.e. no (pre)selection is applied for them. Consequently, also noise, falsely firing double columns or smaller chip regions as well as cosmic radiation might be contained within the cluster size distributions for each run. This in the end contributes to the calculated mean value of the cluster size.

As such, the shown trend of the raw clusters in both plots can be understood in this picture. There is a range of thresholds, where the average cluster size decreases with an increasing sensor threshold. This case represents the expected behaviour and is a direct consequence of the concept of in-pixel discrimination for the primary and shared smaller signal charge, which might not be sufficiently large to trigger a hit in the pixel. For the June testbeam campaign this applies for threshold values larger than $50e$, while for the testbeam campaign in August this effect only sets in at thresholds of about $80e$ and higher.

If the threshold is decreased below these values, the raw average cluster size drops rather quickly and eventually reaches values in between 1 and 2 pixels. This behaviour is not compatible with what would have been expected for clusters produced by a traversing charged particle. For lower thresholds it is anticipated that even more adjacent pixels show a hit due to the shared charge. As such the average cluster size resulting from a charged particle should further increase. It is shown in figure 6.2 at the top, that the noise level in an ALPIDE starts increasing below a threshold of roughly $100e$. As such the sensor noise increases in the same threshold regime as the decrease in raw average cluster size.

This comparison between the noise levels of a flat and the bent ALPIDE chips can be made, since their electrical behaviour was tested to not be significantly affected by bending, as described in the first part of this chapter. One effect of the noise is that a sizable amount of single pixels start firing occasionally at low in-pixel threshold values. Therefore, a lot of single-pixel clusters (size 1) are found. Since they only contribute to the mean value of the cluster size distribution taking into account all kinds of clusters, it needs a certain amount of them and thus a certain increase in noise level in order to see this effect in the average raw cluster size. Therefore, the falling trend of average raw cluster size sets in at slightly lower threshold values than the significant fake-hit rate increase (above the sensitivity level of the noise occupancy scan) for the sensor. For this reasons the decreasing raw cluster sizes for low sensor thresholds is attributed to the increased fake-hit rate of the sensor due to noise.

Starting from low towards higher threshold values, the point of transition from increasing raw cluster size to a decreasing trend can be considered an indicator of the overall noise level of the sensor. Comparing now the bent DUTs from June and August in this aspect, the August DUT indicates a higher noise level. This is confirmed by dedicated noise occupancy scans. This increased noise level is already described in section 4.2.2 and the first part of this chapter.

In order to ensure that a cluster is indeed produced by a real particle and not by noise or any other effect, only a selected subset of the raw clusters can be considered. For this purpose tracking information can be used and only sizes of associated clusters can be considered. Having fulfilled the criterion of being in close proximity of the calculated intercept of a track with the bent sensor surface of the DUT, it is most probable that such a hit originates from a traversing charged particle. Thus, considering only the average size of associated clusters only a falling trend with increasing threshold values is anticipated as discussed before. The results shown as red data points in figure 6.2 exactly follow this bias of charge sharing properties and in-pixel signal discrimination.

For the data of the two differently bent DUTs the average (associated) cluster size is between 3 and 4 pixels, which is slightly higher than expected for flat ALPIDE sensors and MIPs or electrons in the energy regime of the used testbeam. Figure 3.4 at the bottom as well as the reference planes of the beam telescope used for the June and August testbeam campaigns confirm the expected mean cluster size at a nominal operating point to be between 2 and 3 pixels. This overall increased cluster size of both bent sensors in comparison with flat sensors can be attributed to their curved active area. As such, charged particles traverse the bent sensors at an incident angle $\alpha > 0$ with respect to the sensor surface normal. Consequently, they travel a longer distance in the detector material and thus generate more free charge by ionisation. It is clear that an overall increased amount of charge also leads to an increased total amount of shared charge in adjacent pixel, which eventually is sufficient to trigger a hit in this pixel. This explains the generally increased cluster size of the bent ALPIDE sensors as compared to flat ones.

The track incident angle is obviously dependent on the position on the bent DUT sensor surface given the testbeam setup geometries displayed in figure 4.3 and 4.5. Therefore, the cluster size can also be studied considering its dependence on the beam incident angle. It is expected that particles featuring a larger incident angle produce larger clusters, since they travel a longer distance inside the detector material and therefore generate more free charge carriers along their trajectories. This anticipated behaviour of the cluster size is confirmed using teastbeam data from June. Amongst the other results obtained from the June testbeam data, this is presented in the paper written by my colleagues and me [46].

Cluster shapes Clusters of the same size might occur in different *cluster shapes*. For example there is only one possible shape for a single pixel cluster, but two possibilities to realise a two-pixel cluster. In this case the cluster can be elongated in x- or y-direction. For three pixel clusters already a multitude of different shapes and orientations can be produced. However, from charge sharing properties it is clear that having three hit pixels in a row forming a cluster is more unlikely than a three-pixel cluster featuring an L-shape. These considerations apply only, if there is no bias on the cluster size, such as for example bending the sensor, where one direction (the bent one) is preferred over the other.

In order to study cluster shape generation, which is directly linked to the charge sharing properties of one pixel, tracking information can be used. Since the intercept of a track and the sensor surface of the DUT has sub-pixel resolution, the impinging point of the track can be correlated to the size and shape of its associated cluster. Combining this information for all pixels, an in-pixel hitmap can be produced for each cluster size. It represents the behaviour of an average pixel on the investigated sensor.

Figure 6.3 displays such in-pixel hitmaps for the major four occurring cluster sizes, i.e. for one-, two-, three- and four-pixel clusters. All of the shown in-pixel hitmaps were produced for a dedicated high statistics run of the June testbeam campaign. Since in-pixel studies require a larger amount of statistics a run featuring at least 3M recorded events is chosen. Furthermore, this run features a DUT threshold of close to $100e$ thus representing the bent sensor performance at the nominal working point of an ALPIDE sensor.

For single pixel clusters, represented by the top left panel of figure 6.3, it can be seen that a particle has to hit a pixel centrally to have a high probability of producing only a single-pixel cluster. In order to produce a single-pixel cluster the signal charge has to be generated in the vicinity of the collection diode, since otherwise enough charge is shared to adjacent pixels leading to larger clusters. Consequently, only a small fraction of charge diffuses and possibly enters a neighbouring pixel. This effect can even be enhanced by applying a back-bias voltage and thus

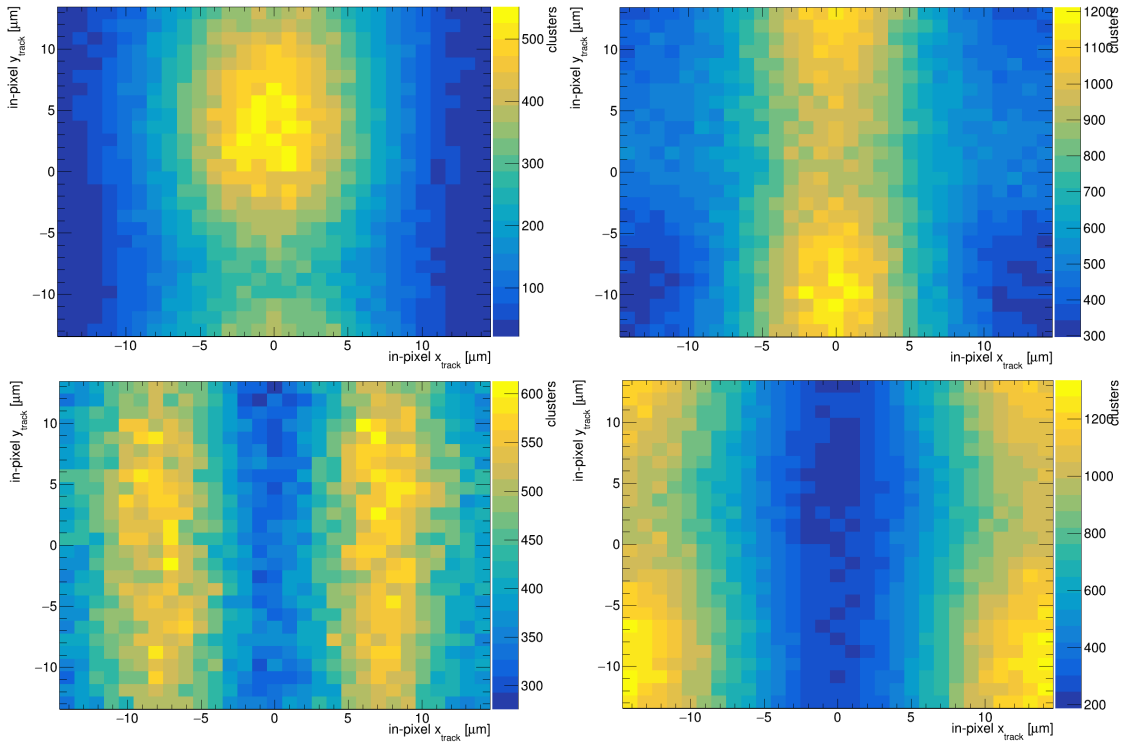

Figure 6.3 **(top left)** In-pixel hitmap showing the intercept points of tracks featuring an associated cluster of size 1.
(top right) In-pixel hitmap showing the intercept points of tracks featuring an associated cluster of size 2.
(bottom left) In-pixel hitmap showing the intercept points of tracks featuring an associated cluster of size 3.
(bottom right) In-pixel hitmap showing the intercept points of tracks featuring an associated cluster of size 4.
The data shown for all four panels represents a dedicated high-statistics run with at least 3M events featuring a DUT sensor threshold value close to the nominal working point of 100e. The in-pixel bin size is 1 µm. The number of associated clusters for tracks in a specific spatial region (bins) is colour-coded.

further increasing the depletion region[2]. In this picture, the shown in-pixel hitmap for one-pixel clusters can be understood.

Same consideration can be made considering the in-pixel hitmaps of larger clusters, such as two-pixel clusters represented at the top right of figure 6.3. In this case it is shown that particles have to hit the pixel in the centre of its edges. As such, a sizeable amount of charge is shared to the neighbouring pixel resulting in a two-pixel cluster. In general, this is valid for any of the pixel edges. However, in the presented case the two-pixel clusters occurring are almost exclusively elongated in y- rather than x-direction. This is a direct consequence of the bending of the chip. Since the y-direction is bent, particles traverse the sensor at an incident angle thus leaving behind a trace of charge extending in this direction. For this reason the signal charge is more likely to reach adjacent pixels along the bending direction of the chip.

For three- and four- pixels clusters the mechanisms are exactly the same as the previously described ones. In order to produce an L-shaped three-pixel cluster, charge from the primarily hit pixel has to be shared to two neighbouring pixel across two perpendicular edges of the pixel. As such the particle would have to hit the pixel in an corresponding intermediate position as shown

[2]Not in the scope and therefore not applied for this work

in figure 6.3 at the bottom left. For four-pixel clusters, a pixel needs to be hit by the particle in the very corners in order to ensure that a sizeable amount of charge is also shared to the diagonally adjacent pixel, where it still needs to overcome the threshold. This is clearly visible in the bottom right panel of figure 6.3.

This sub-pixel information of in-pixel hitmaps in correlation with the cluster size can be and is used to improve the position resolution. With the ALPIDE chip only featuring a binary output, the simplest approach of calculating the cluster position is simply taking the mean value of the pixel centre position. However, taking into account cluster shape information as presented above the position of the cluster centre can be determined with a higher precision.

6.2 Detection efficiency of the sensor

A central quantity in order to describe the performance of a sensor is its *detection efficiency*. As already described in section 5.9, it is measured as the number ratio of tracks featuring an associated cluster on the DUT over total accepted tracks. Here, accepted tracks refers to a selection of tracks according to several parameters to ensure a good track quality. As such the efficiency is dependent on the quality of the DUT alignment with respect to the reference planes giving the track. Especially for a bent detector surface rotational degrees of freedom in the alignment procedure are of major importance as compared to flat sensors, where the rotation of the sensors is highly constrained by their mechanical mounting.

Testbeam campaign June 2020 Relying on the implementation of the bent sensor geometry in Corryvreckan, which is described in section 5.8, the standard alignment procedure with this testbeam analysis framework is followed as described in chapter 5 and especially in section 5.7. Unfortunately, the way of introducing the bent sensor geometry to Corryvreckan, does not allow to take the bending radius into account for the alignment of the DUT. Especially for the DUT used in June, where position measurements on the bent sensor surface revealed a relaxation of the bent chip, this is a problem. It is obvious that the bending radius plays a major role for the sensor geometry and thus is a first order contribution to the track residuals and the alignment. Having no control on the bending radius in this case, a first approach is to repeat the alignment procedure for different radii by manually inserting them into the geometry configuration file. As such, the effects on the resulting DUT alignment and the other analysis quantities, such as the detection efficiency and the track residuals as described in section 6.4, can be studied.

In this approach it was found that the bent geometry is best described around a bending radius of $22\,\mathrm{mm}$. Furthermore, the flat part, where the chip is glued to the carrier board, is neglected for this study ($y_0 = 0\,\mathrm{mm}$). Given the measured bending radii directly after bending $r_{\mathrm{before}} = 16.9\,\mathrm{mm}$ and after the testbeam experiment when the sensor relaxed to a radius of $r_{\mathrm{after}} = 24.4\,\mathrm{mm}$, this value is reasonable.

For the subsequent analysis only the necessary track selection is done. In this first approach no constraints on the track's χ^2_{red} value are set. Nevertheless, a reasonable χ^2_{red} is ensured by the track fitting algorithm in order to exclude track fitting for non-correlated points on the reference planes. Furthermore, a track is only accepted if it features an associated hit on each reference plane of the beam telescope. In order to exclude the dead double and regions at the edges of the chip a region of interest (ROI) is defined, as it can be seen in the top panel of figure 5.6. Tracks featuring an intersection point with the DUT outside of this region are not considered in the further analysis. It has to be taken into account that the actually excluded chip region is slightly larger than the defined ROI due to the dimensions of the search window applied for

cluster association. In the case of this first alignment approach the search window dimensions where chosen to be $100\,\mu\mathrm{m} \times 100\,\mu\mathrm{m}$. As such, clusters on the DUT featuring a position inside this window around the track intercept are associated to this track. Only the closest found cluster within this window is associated. Moreover, the ROI is chosen such that the hit occupancy of the pixels within is comparable, i.e. focussing on the central region of the beam spot on the sensor. Furthermore, the ROI is such that increased scattering angles resulting from material overlapping with the border regions of the DUT active area upstream of it, e.g. PCB material from the carrier cards, do not disturb the efficiency measurement.

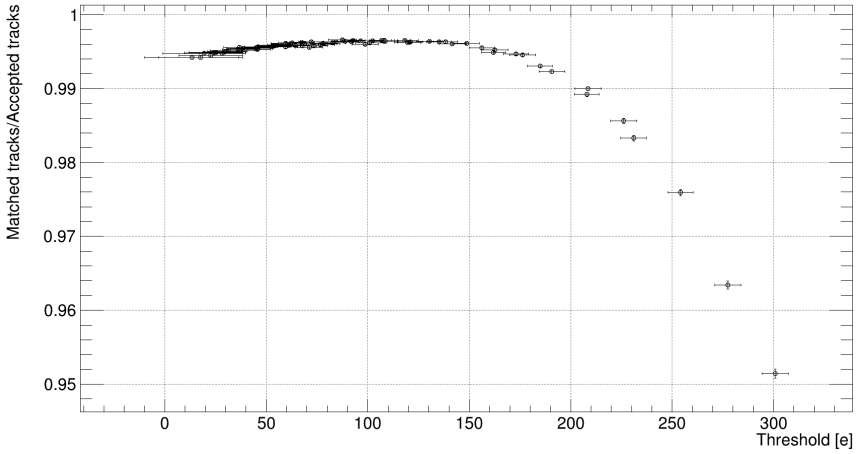

Figure 6.4 Sensor efficiency for different runs in the June testbeam campaign featuring different DUT threshold values. The efficiency is calculated as a ratio of the number of matched tracks divided by the total number of accepted tracks. The plateau region around $100e$ threshold corresponds to a sensor efficiency of $99.6\,\%$. For this analysis no strict track quality cuts are applied.

The detection efficiency obtained with these settings is shown in figure 6.4. Moreover, its dependency on the working point of the DUT is plotted. It can be clearly seen that around the nominal sensor threshold of $100e$, there is a plateau region featuring a sensor efficiency of about $99.6\,\%$. Going towards higher threshold values the efficiency starts to significantly decrease when going beyond $150e$ in threshold. This behaviour is expected and can be explained as follows. For higher in-pixel thresholds the probability that the generated charge of a traversing particle is not sufficient to trigger the pixel to *fire*, i.e. registering a hit, is increased. This is especially true at the very x-edges of the pixels and extends towards its middle. Consequently, it might occur that even though a particle passed through the DUT no hits are registered and no cluster can be associated to the corresponding accepted track. Per definition this decreases the efficiency. It is clear that the effect gets even larger with further increased threshold values, thus explaining the trend visible in figure 6.4.

The slight decrease in efficiency towards lower thresholds is however not understood. In contrast to what is visible in the plot, it is expected that the efficiency converges to a value of $100\,\%$. This would be explained by the fact that the noise level and therefore the fake-hit rate is increased for very low threshold values. Consequently, the hit occupancy of the sensor is increased such that almost always a cluster is found within the search window and is therefore associated to the track. There is the suspicion that this unexpected efficiency decrease might be caused due to the fact that the DUT alignment is not stable throughout the different runs, i.e. it fails to describe the bent DUT sensor geometry equally well. However, there is no strong evidence for this suspicion. Also the efficiency for the nominal working point is expected to

be much higher, i.e. above $99.9\,\%$, when assuming a similar performance of the bent and flat ALPIDE sensors. This can be seen in the top panel of figure 3.4. In lack of any other reasonable explanation for these two observations, the possibility that the bent detector geometry of the DUT is not well enough described or aligned is explored by trying a second alignment approach. It is the one being followed by [46].

While for this the ROI and the general bent sensor implementation within the Corryvreckan framework is kept the same, other analysis parameters were optimised. As such the preprocessed data from Corryvreckan is exported to a json-file. Offline of Corryvreckan, the DUT is aligned with respect to the reference planes also including the bending radius as a free parameter. This least-square optimisation for the cylindrical sensor model yields a bending radius of $22.57\,\mathrm{mm}$, which is used for the further analysis. The stability of this alignment was confirmed by also aligning on the basis of other runs, which yielded comparable values for the bending radius. Additionally, also a possible z-shift of the DUT is considered by this alignment. In order to ensure a good straightness of the tracks, a $\chi^2_{\mathrm{red}} < 3$ selection is applied. Furthermore, the search window size is chosen such that it is as large as possible, while not significantly impacting the statistics due to the border exclusion regions. For this purpose a window size of $250\,\mu\mathrm{m} \times 250\,\mu\mathrm{m}$ is chosen [46]. Moreover, two batches of runs with different physical alignment of the DUT were combined in order to gain more statistics for the efficiency calculation over the full DUT sensor surface. In one DUT position the beam spot is centred on the sensor surface, while for the second alignment the DUT is shifted in y-direction such that the beam spot is more focussed on the bent part of the chip. The ROI for this second case is adjusted accordingly.

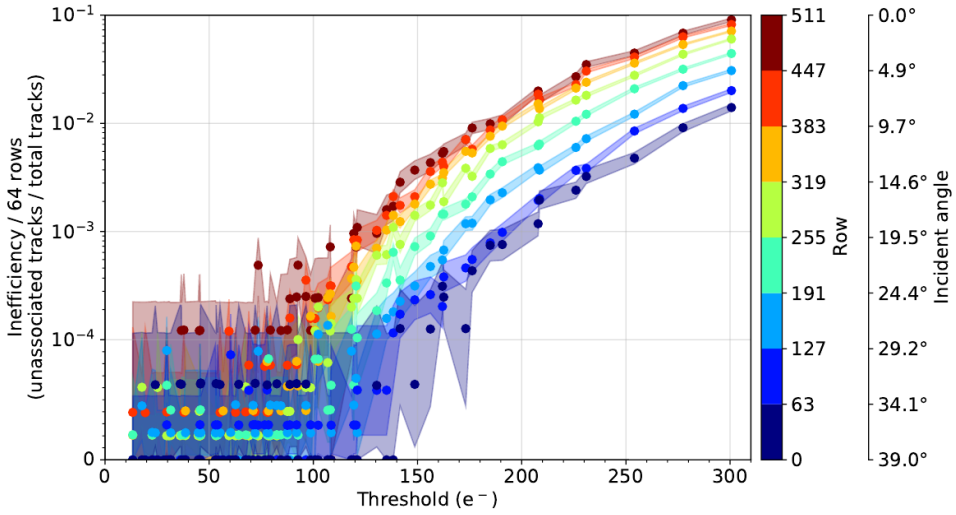

Figure 6.5 Inefficiency versus DUT threshold based on data from the June testbeam campaign. It has to be noted that the vertical axis is semi-logarithmic. For the presented range of thresholds, the inefficiency is calculated in bins comprising 64 rows. The respective position bin in row direction is colour coded and corresponds to a track incident angle with respect to the sensor surface normal shown on a separate axis [46][3].

The detection efficiency results for this second (corrected) approach are shown in figure 6.5. Here, the *inefficiency*, i.e. the number ratio of accepted tracks without an associated cluster over total tracks, is plotted versus the sensor threshold. Furthermore, the inefficiency is not calculated over the full sensor surface, but considering horizontal regions each comprising 64 rows. As such, they represent a corresponding range of the beam incident angle with respect to the surface

[3] I was not the one ultimately producing this plot, but I certainly did contribute to the results presented there and in the corresponding paper.

normal of the curved sensor. In the plot, different regions are denoted with a different colour and the corresponding beam incident angle range is shown on a separate axis. As expected, it can be seen that a large row number corresponding to the lower sensor edge leads to a large beam incident angle and thus a larger amount of charge generated by a traversing particle as already explained for the cluster size analysis. This fact explains why the inefficiency is systematically higher for track incident angles close to $0°$. This is the case comparable to a flat ALPIDE sensor. Going towards higher track incident angles, i.e. lower row numbers, the inefficiency decreases over the full threshold range. This means the sensor shows a higher efficiency at its lower edge as compared to regions closer to its upper edge. This effect can be only disentangled for sufficiently high threshold values, when the efficiency starts to decrease, i.e. the inefficiency starts to increase, for the aforementioned reasons. As before, it is shown that the efficiency significantly starts to decrease above a threshold value of about $150e$.

In the range of the nominal working point of $100e$, the efficiency is generally better than $99.9\,\%$. As previously discussed, it is therefore shown that the bent sensor features a similar efficiency as compared to a nominal flat ALPIDE chip [46]. As expected the inefficiency drops to values close to and even directly to $0\,\%$ in the very low threshold regime. As already mentioned and explained this is attributed to noise clusters being randomly associated to a track and therefore artificially increasing the calculated detection efficiency. Due to the generally low fake-hit rate, the trigger settings[4] and masking of noisy pixel in a dedicated analysis stage, this effect of falsely associated clusters to a track is considered negligible around the nominal working point and especially for high threshold values.

Testbeam campaign August 2020 In comparison with the June case, the bending radius of the bent DUT is much more constrained and under control for the testbeam campaign in August 2020. As described in section 4.2.2, the DUT is directly glued to a 3D-printed cylindrical jig with a well defined radius of $18\,\mathrm{mm}$. Given the negligible sensor thickness of only $50\,\mu\mathrm{m}$, it is legitimate to perform the DUT alignment and the subsequent analysis with this value of the bending radius as an input for the bent sensor geometry implementation within the Corryvreckan framework. Therefore, the DUT alignment is entirely performed using the Corryvreckan framework.

For a first analysis approach of the August testbeam data, no track selection on the basis of χ^2_{red} is applied. Furthermore, no ROI is defined in order to see effects of all regions. However, due to the rotation of the DUT with respect to the reference planes by $270°$, as it can be seen in the lower part of figure 5.6, there is a *natural ROI* given by the limits of the overlapping region. The search window is chosen to be $100\,\mu\mathrm{m} \times 100\,\mu\mathrm{m}$ to be sensitive to effects resulting from local deviations of the actual curved sensor surface to the cylindrical model used in the data analysis.

The resulting detection efficiency for several runs featuring different working points, is shown in figure 6.6 The expected trend of the efficiency is clearly visible there. For the already discussed reasons the detection efficiency starts to decrease for sufficiently high threshold values. As also shown for the June testbeam campaign and in the top panel of figure 3.4, for flat ALPIDE sensors this effect becomes sizable above a threshold of about $150e$. Around the nominal working point of $100e$ and extending to lower thresholds the obtained efficiency is generally above $99.9\,\%$. This is considered another strong indication that the detection efficiency of bent ALPIDE chips as an example for curved CMOS MAPS is retained as compared to flat sensors.

For the further analysis of this data it remains to define a suitable ROI and ensure a high track quality by selecting them according to a χ^2_{red}-criterion. With these improvements and taking into account large enough statistics a similar plot as shown in figure 6.5 is to be produced to display

[4] Presented in section 4.3

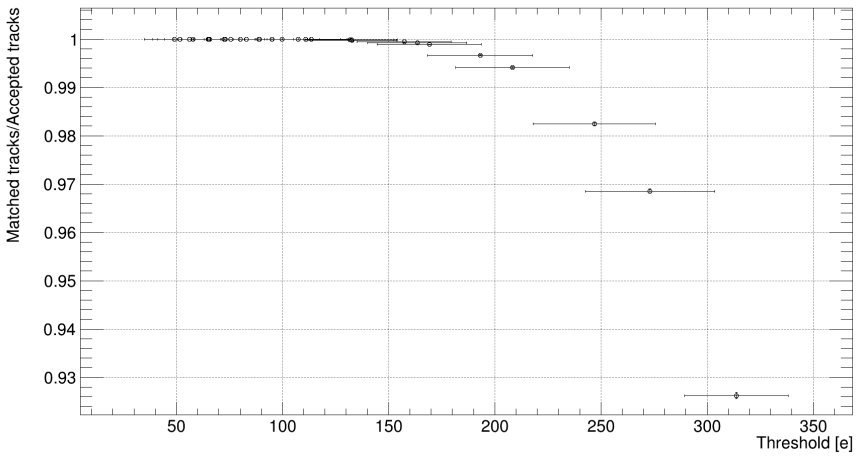

Figure 6.6 Sensor efficiency for different runs in the the August testbeam campaign featuring different DUT threshold values. The efficiency is calculated as a ratio of the number of matched tracks divided by the total number of accepted tracks. The plateau region around $100e$ threshold corresponds to a sensor efficiency of above $99.9\,\%$. For this analysis neither strict track quality cuts nor a ROI are applied.

and summarise the final results for the August testbeam campaign. However, already having the presented preliminary result of the detection efficiency, it is legitimate to assume that there will not be significant changes or unexpected findings.

6.3 In-pixel efficiency

In order to gain a deeper understanding of the charge collection efficiency inside of one pixel, the information if a reconstructed track is counted as efficient or not can be correlated with the position of its intersection point with the sensor surface of the DUT. Since the track intercept position is determined with sub-pixel-pitch resolution, it can be converted to an in-pixel coordinate frame, where the position is given relative to the pixel dimensions. Doing this for every available reconstructed track yields enough statistics in order to calculate a position resolved *in-pixel efficiency*. As it is the case for the sensor efficiency, the in-pixel efficiency is calculated as the ratio of the numbers of matched tracks over total accepted tracks. This is done for discrete pixel regions, i.e. position bins, in order to produce an efficiency map for an average pixel on the sensor.

Such in-pixel efficiency maps are shown in figure 6.7. Each of the maps shown in the two panels represents the data of a dedicated high-statistics run from the June testbeam campaign featuring at least 3M events in order to ensure the required statistics for the analysis of such in-pixel quantities. While the upper panel represents a run featuring a DUT sensor threshold close the nominal ALPIDE working point, namely $97e$, the lower panel corresponds to a run with DUT settings leading to a *high* threshold of $277e$. In both cases the considered position bins are of the size of $2.5\,\mu\mathrm{m} \times 2.5\,\mu\mathrm{m}$.

For the case of the nominal working point it can be seen that generally high efficiency values are uniformly distributed over the entire pixel area. As comparable to the sensor efficiency for bent sensors presented in the previous section, the mean in-pixel efficiency for this case is above $99.9\,\%$. Pixel regions showing efficiencies below this average value are randomly distributed across the pixel area. As such, no specific inefficient pixel regions can be identified, which is expected given the very high overall sensor efficiency measured with the same alignment settings.

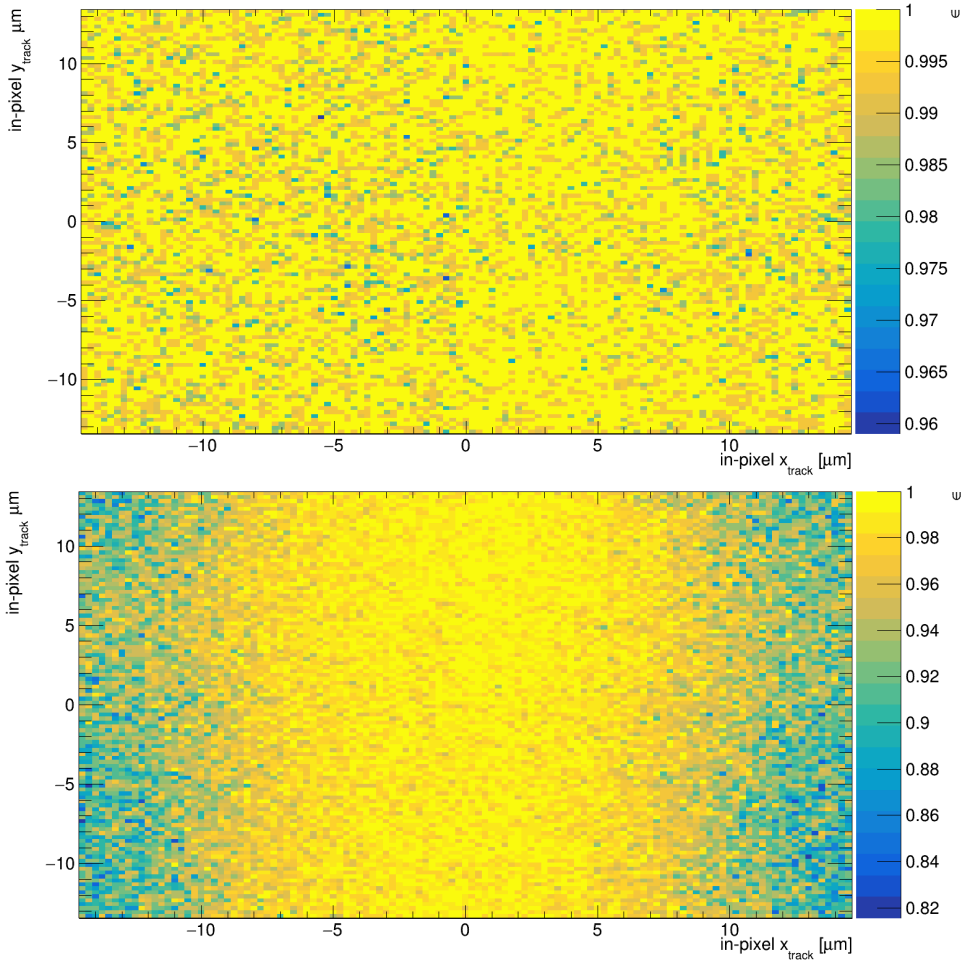

Figure 6.7 **(top)** In-pixel efficiency map for a nominal DUT threshold of about $97e$.
(bottom) In-pixel efficiency map for a high DUT threshold of about $277e$.
The efficiency of a sensor region is colour-coded for both plots. Efficient or inefficient tracks are assigned to a position region (bin) according to their intercept position with the bent sensor surface. The position bins are $2.5\,\mu\text{m} \times 2.5\,\mu\text{m}$. To guarantee sufficiently high statistics in each position bin both hitmaps are based on dedicated high-statistics runs from the June testbeam campaign featuring at least 3M total events.

Now the high-threshold configuration is considered, where it has already been shown that the overall sensor efficiency is significantly decreased. First of all, it has to be noted that in this case the colour scale representing the calculated detection efficiencies for every position bin extends over a larger range as compared to the nominal-threshold situation. While for nominal DUT settings generally high in-pixel efficiencies above $96\,\%$ are found, a sizeable amount of pixel regions show efficiencies of $94\,\%$ and lower for the high-threshold configuration. It is clearly visible that there is a highly efficient pixel region centred in x-direction. On the contrary, the in-pixel efficiencies decrease with increasing distance to the centre in x-direction. This leads to relatively clear *inefficient* regions at the x-edges of a pixel.

As already discussed in the framework of the cluster size analysis, the reason for these differences are the charge collection properties and the in-pixel signal discrimination. For the nominal working point the in-pixel threshold is sufficiently low that independent of the hit position of the traversing particle, the collected amount of signal charge is enough to trigger a pixel hit. If for instance a particle hits the pixel in the very corner, a large fraction of the signal charge is shared to the neighbouring pixels due to diffusion. As shown in figure 6.3 this eventually causes a

four-pixel cluster. Nevertheless, the charge remaining and being collected in the primary hit pixel is still enough to overcome the in-pixel threshold. As such, a hit is registered in this case. Now considering the same situation, but for a very high in-pixel threshold. The remaining amount of signal charge collected inside the primary hit pixel might not be sufficient anymore in order to overcome the charge threshold. As such, no hit is registered in this pixel and consequently also not in the adjacent pixels since the same argumentation is true for the shared signal charge. As an overall consequence no cluster can be associated to this track, which causes it to be counted as inefficient.

Also considering the other cases of one-, two- and three-pixel clusters as presented in figure 6.3 and following the same argumentation presented in the example above, the difference in the two in-pixel efficiency maps can be understood and explained. In summary, if the particle hits the pixel in a position such that a fraction of the signal charge is shared to neighbouring pixels, it depends on the set threshold if they and especially the primary hit pixel register a hit. For nominal threshold settings this is almost always the case independent of the particle hit position and thus the shared amount of charge to other pixels. In this case, there is always at least a one-pixel cluster that can be associated to the track in order to be counted as efficient. Going towards higher thresholds, the average pixel starts to show inefficiencies. First, this effect is visible in the pixel corners, since in this case the charge is shared to the highest number of pixels. As such the amount of collected charge per pixel is the lowest, eventually rendering all of these pixels not registering a hit. Further increasing the threshold, also more central regions start to be affected. According to the same argumentation as for the cluster shapes presented in section 6.1, also the extension of the efficient region in y-direction can be understood as a direct consequence of the chip curvature. In this direction the particle traverses the sensor with an incident angle, thus generating more charge along its trajectory.

The argumentation presented above not only explains the in-pixel efficiency maps, but also gives the microscopic reason why the overall sensor efficiency decreases with increasing threshold. Especially the trend that higher the efficiency is larger for larger track incident angles is covered by this microscopic picture.

6.4 Spatial resolution

Another central quantity to characterise the performance of a tracking detector is its *position resolution*. As described in section 5.9, it is not directly measurable from the testbeam data. However, it is accessible via the standard deviation of the track residual distribution $\sigma_{\mathrm{residual}}$ in the respective coordinate direction as given by equation 5.5. Having the tracking resolution of the beam telescope used in the June and August testbeam not yet at hand, the *standard deviation of the residual distribution* is presented in the following as a measure for position resolution.

It is shown in figure 5.5 that the track residual distribution for a bent DUT in x- and y-direction is Gaussian given a good alignment. However, this requires that the curved sensor geometry is well described by the cylindrical model implemented within the Corryvreckan framework. In this case, a Gaussian function can be fitted to the residual distributions taking into account the data for a full run. As such, for both coordinate directions of interest (x,y) the standard deviation σ_{res} and its uncertainty can be extracted from the fit. Doing this for several runs featuring different working points of the DUT, the qualitative dependency of the position resolution on the sensor threshold setting can be evaluated.

For the June testbeam campaign this is illustrated in figure 6.8 in the top panel, while the bottom panel shows the same quantities obtained from August testbeam data. Qualitatively, both panels

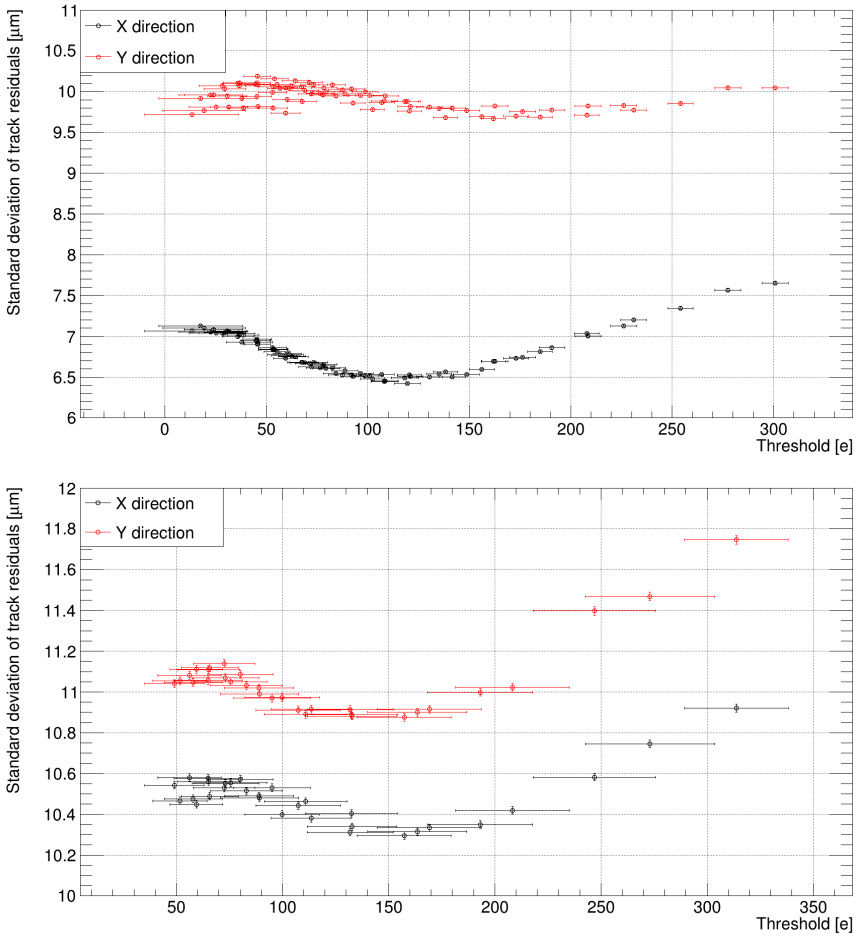

Figure 6.8 Dependence of the width of the residual distribution on the sensor threshold for runs from both testbeam campaigns. The residual distribution width for the x-direction is denoted in black, while the one in y-direction is represented by the red symbols. Each data point is obtained from one run with at least 300k events.
(top) The shown data corresponds to runs from the testbeam campaign in June 2020.
(bottom) The shown data corresponds to runs from the testbeam campaign in June 2020.

show the same trends for σ_{res} in both coordinate directions. For all four cases there is a visible minimum in the standard deviation of the residual distributions indicating the working point with the optimal position resolution. It can be seen that this working point is a different one for the two testbeam cases. While in June an optimal position resolution is reached at a threshold value of slightly above $100e$ (at least in x-direction), this point is around $150e$ for the August testbeam data. From the raw cluster size analysis presented in section 6.1 and illustrated in figure 6.2 it can be seen that the threshold value, below which the noise level of the DUT increases significantly, is also shifted by about $50e$ when comparing June and August testbeam data. Therefore, it can be concluded that the optimum in position resolution is directly related to the noise level of the respective DUT.

It is intuitively understandable, that the position resolution and thus σ_{res} worsens or increases with an increased noise level. A higher noise level increases the probability of a pixel to fire.

Consequently, the probability that a cluster resulting from noise is associated to the track is higher. Since the noise is not correlated with the track intercept, the residual tends to be larger. Over the full pixel matrix and a full run, this leads to a broader residual distribution and therefore a worse position resolution. This explains the increasing trend of σ_{res} towards lower threshold values due to an increased noise level. However, it can be seen that for all four presented cases, there is the indication that σ_{res} decreases again or at least saturates for even lower thresholds. This effect is not yet understood and subject to further research.

On the other hand, the increase of σ_{res} towards higher threshold values can be understood looking at the the average cluster sizes. As the cluster size generally decreases with increasing in-pixel threshold as presented in section 6.1 and figure 6.2, the precision of the cluster position also decreases. This in turn leads to a broader residual distribution and can therefore be identified with the increasing trend of σ_{res} towards larger threshold values as shown in figure 6.8.

In the case of the June testbeam campaign it can be seen that the points of optimal position resolution in x- and y-direction, i.e. the minimum in σ_{res}, are shifted with respect to each other. Also this behaviour is not yet understood and needs to be further investigated. One possibility of doing this is a cluster shape sensitive analysis as described later.

Given the fact that the x-direction represents the non-bent direction for both beam tests considering the global frame, it is expected that this case resembles the behaviour of a flat ALPIDE chip. This assumption is only valid, if the x- and y-coordinate are not or only weakly correlated. It has been verified that this is indeed the case for both presented testbeam campaigns. Looking at the x-residuals for the June testbeam data, it is visible that the residual distribution width is of the order of $6.5\,\mu\mathrm{m}$ around the nominal working point of the ALPIDE sensor. Taking into account that the position resolution for this case is even lower than this value as discussed in section 5.9, this is comparable with the nominal ALPIDE spatial resolution of about $5\,\mu\mathrm{m}$ [6]. Looking at the August testbeam data, the situation is different. There, the optimum x-residual distribution width is around $10.3\,\mu\mathrm{m}$. Given the higher overall noise level of the DUT used in August as compared to the DUT for the June testbeam campaign, the overall increase of σ_{res} when comparing these two cases can be understood.

A further important observation that can be made in figure 6.8 is the difference between x- and y- residuals. In both cases the width of the x-residual distribution is generally larger than the one for the corresponding y-residual distribution. Furthermore, it can be noted that the average distances between $\sigma_{\mathrm{res,x}}$ and $\sigma_{\mathrm{res,y}}$ are of different magnitude. While the effect is rather large for the June testbeam case, it is significantly smaller for the August testbeam data. The average distance $\sigma_{\mathrm{res,y}} - \sigma_{\mathrm{res,x}}$ is of the order of $3\,\mu\mathrm{m}$ and $0.5\,\mu\mathrm{m}$ for June and August, respectively.

From first principles it is expected that the position resolution in y-direction is better than in x-direction, since cluster sizes are increased in the bending direction due to the resulting track incident angle. However, from the width of the corresponding residual distributions it seems to be the other way round in both presented cases. In the corresponding plots, it is visible that $\sigma_{\mathrm{res,x}}$ is clearly smaller than $\sigma_{\mathrm{res,y}}$ for the entire considered sensor threshold range. Furthermore, the pixel pitch can be considered. For the x-direction it is slightly larger than in y-direction, namely $29.44\,\mu\mathrm{m} \times 26.88\,\mu\mathrm{m}$. From this, it would be expected that the position resolution in x-direction is slightly worse as compared to the one in y-direction. Due to the rotation of the DUT used in the August testbeam campaign with respect to the reference planes, this is only true for the June case. Considering the pixel pitch difference for the August case, the position resolution in x-direction is expected to be better than the one in y-direction as it is the case in figure 6.8.

Explaining the feature of the difference between $\sigma_{\mathrm{res,y}}$ and $\sigma_{\mathrm{res,x}}$, there are two competing factors that need to be considered. For one, there is the difference of the pixel pitch in x- and y-direction. On the other hand, there has to be an effect resulting from the bending of the chip. A

strong indication of the latter is the different magnitude of the visible difference between x- and y-direction. Due to the different kinds of bending and mounting of the two presented DUTs, the associated range of possible beam incident angles is different. As such the June DUT features a large range of incident angles up to 39°, while the August DUT can be considered almost flat in the overlapping region with the beam telescope reference planes. As such the effect caused by the bending is supposed to be larger for the June case as compared to the August case as it is visible in figure 6.8. The argumentation of the bending effect would be as follows. Due to the bending in y-direction different cluster sizes and therefore different cluster shapes are predominant at different positions in y-direction. Related to the different cluster shapes there comes a shift in the mean position of the associated clusters. As such the residual distribution over all y-directions would be broader. Consequently, $\sigma_{\mathrm{res,y}}$ is increased as compared to $\sigma_{\mathrm{res,x}}$, where the cluster shape is not biased. In order to test this hypothesis, a dedicated analysis especially accounting for cluster shapes would be needed. In fact, the full residual analysis described above could be repeated but only selecting tracks featuring one specific shape of its associated cluster. As such the bias by the bending should be removed and the effect of the two competing parameters, namely bending and pixel pitch difference, can be disentangled. However, selecting only one cluster shape would require a large amount of statistics for the results to be meaningful.

Position resolved residual distribution In order to test how well the bent sensor geometry is described by the implemented cylindrical model, the residual value can be correlated with the corresponding hit position. Doing so, there should be no dependence of the residuals in the non-bent direction. For both of the testbeam campaigns, this is the x-direction. In the bent direction, there should also be no correlation of the y-residual distribution and the corresponding y-coordinate of the associated hit. However, if there are local deviation of the physical sensor from the modelled perfectly cylindrical shape, this would lead to an increased residual value. Thus, such deviations could be identified as a shift of the mean value of the residual distribution for a corresponding hit coordinate range in this direction.

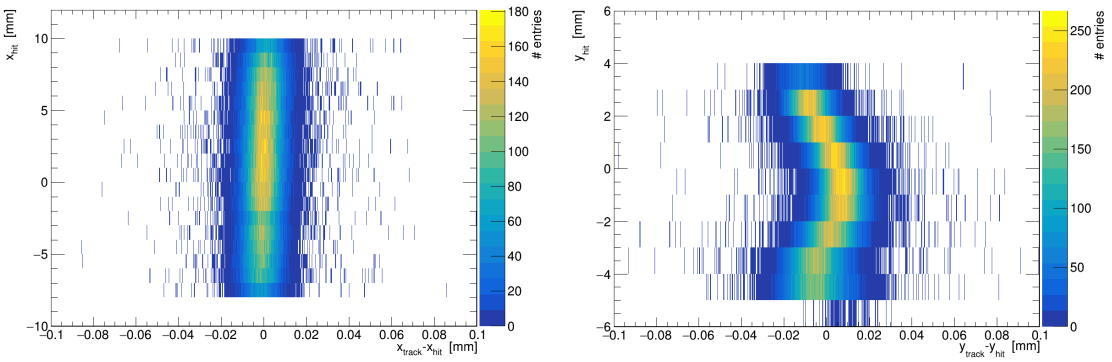

Figure 6.9 Track residuals correlated with the respective position of the hit in both coordinate directions. The plots are based on data from the June testbeam campaign. Furthermore, they represent the case of a first alignment for the DUT with no strict track selection cuts applied. The number of entries per residual-hit-position bin is colour-coded.
(left) Two-dimensional correlation of residual and corresponding hit position in x-direction. This direction represents the non-bent case.
(right) Two-dimensional correlation of residual and corresponding hit position in y-direction. This direction represents the bent case.

For the June testbeam data, these position resolved residual distributions are shown in figure 6.9. While the left panel shows the x-residual distributions correlated with the corresponding

hit coordinate in x-direction, the right panel shows the same plot for the y-residuals versus the corresponding y-hit-position. It can be clearly seen that the x-direction, i.e. the non-bent case, behaves as expected. The residual distributions for a certain x-hit-position-range are all centred at $0\,\mathrm{mm}$ and feature comparable widths.

For the y-direction, the situation is different. There, the mean values of the y-residual distributions considering the centre of the chip deviate from $0\,\mathrm{mm}$ and are shifted to larger values. This means that the sensor geometry is not well described in the chip centre by the cylindrical model. One effect possibly causing these deviations, is the *sagging* of the bent chip due to its mounting. Especially for the lower edge of the chip corresponding to small y-hit-positions, this effect should be sizeable. Showing up in the middle of the chip, it is believed that this deviation at the lower edge of the chip is mitigated by rotation during the alignment of the DUT. This is due to the fact, that the alignment procedure only takes into account and optimises the residual distributions over the full chip and especially does not account for local variations. Summing up the shown residual distributions for the different y-hit-position ranges, a zero-centred Gaussian distribution is achieved.

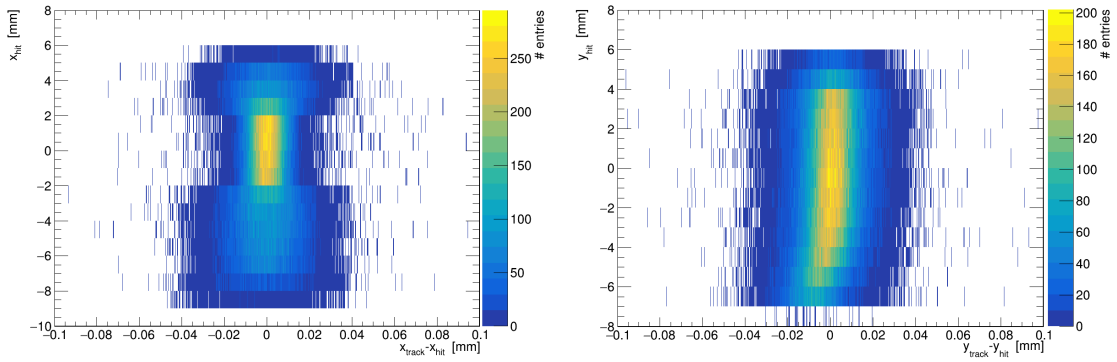

Figure 6.10 Track residuals correlated with the respective position of the hit in both coordinate directions. The plots are based on data from the August testbeam campaign. Furthermore, they represent the case of an alignment for the DUT with no strict track selection cuts applied. The number of entries per residual-hit-position bin is colour-coded.
(left) Two-dimensional correlation of residual and corresponding hit position in x-direction. This direction represents the non-bent case.
(right) Two-dimensional correlation of residual and corresponding hit position in y-direction. This direction represents the bent case.

The same considerations can be done for the August testbeam data as shown in figure 6.10. As previously discussed in this case the radius of the bent DUT in this case is more under control. Since the DUT is glued directly on a cylindrical jig, the sensor surface should perfectly resemble the modelled cylindrical shape. As it can be seen in the right panel of the figure this is nicely shown for the y-residuals correlated to the corresponding y-hit-position. For a large range of y-positions the bent DUT is well described by the cylindrical model. This means the corresponding residual distributions are all centred at $0\,\mathrm{mm}$. At the highest and lowest y-positions, which represent the limits of the DUT overlap with the reference planes a decrease in statistics can be observed. Furthermore, a slight shift of the mean value for residual distributions corresponding to low y-hit-positions towards lower values can be observed. Having a closer look at the DUT used in the August testbeam campaign, it can be seen that the sensor slightly detaches from the cylindrical jig at the very edges of the short sensor side. The possibility that the residual shift can be attributed to this fact needs to be explored. For example it could be accounted for by introducing a second, larger bending radius in order to model this.

The case of the x-direction is shown in figure 6.10 on the left panel. Being the non-bent direction, the residual distributions are expected to be centred around $0\,\mathrm{mm}$ and should feature a comparable width independent of the corresponding x-hit-position. It can be seen that all shown residual distributions are indeed centred at the expected value. However, there are clear regions with broader residual distributions for low and high x-hit-positions, while around the centre of the chip in x-direction the residual distributions show the expected widths. It can be seen that the x-range of the *well-behaved* residuals is of the order of $4\,\mathrm{mm}$ to $5\,\mathrm{mm}$ given the precision of the bin size in the position direction. This corresponds to the width of the cutout in the cylindrical jig behind the bent DUT as presented in section 4.2.2. The broadening of the residual distributions not corresponding to this cutout region can be explained as a result of scattering of the beam particles in the jig material. This scattering distorts the reference tracks by impacting the measured positions on the beam telescope reference planes downstream of the bent DUT. Consequently, the absolute distance of the associated cluster position to the distorted reference track increases and thus leads to a broader residual distribution as it can be seen in the plot.

In order to account for this in a further analysis of the August testbeam data only the the chip region of the bent DUT overlapping with the jig window should be selected by defining a respective ROI. Additionally, also the low statistics boarder regions should be excluded accordingly. As such, the further analysis strategy for the August testbeam data is clear.

7 Summary, conclusion and outlook

In the scope of this work, an introduction to the basic working principles of MAPS and the related electrical components is given in the first chapter of this document. For this purpose, the ALPIDE chip, which was developed for the upgrade of the ALICE Inner Tracking System (ITS), is used as an example. This ITS2 upgrade project makes ALICE one of the first experiments to implement a full-scale tracking detector based on MAPS technology. Furthermore, future applications of truly cylindrical, i.e. curved, CMOS MAPS are discussed in chapter 2. As a first step towards this direction, the research and development phase for bent MAPS has already been started in view of the upgrade plans for a third generation ALICE ITS.

A detailed description of the ALPIDE chip is given in chapter 3. This especially includes the functionality of the in-pixel circuitry and the sensor performance of a standard, flat ALPIDE chip. However, the main scope of this work is the investigation and characterisation of bent MAPS. For this purpose, $50\,\mu\mathrm{m}$ thin standard ALPIDE chips are bent in two different ways. In a first approach the chip is laterally bent in the row direction, thus compressing the integrated in-pixel circuitry. The second approach is to longitudinally bent the chip in column direction such that the integrated electronics is decompressed. Bending radii of $18\,\mathrm{mm}$ and even less are achieved. Both of these devices are thoroughly described in section 4.2 and are proven to be still electrically functional. Moreover, there is a strong indication that the functionality of the in-pixel and chip circuitry is, if at all, only negligibly affected by the chip bending. This is clearly shown in figure 6.1, where the results of a threshold scan for an ALPIDE chip in bent and flat configuration are compared to each other. Here, a threshold scan is a very useful and central standard test for an ALPIDE chip, since it involves the full readout chain beginning with the analog and digital in-pixel front-end electronics.

Testbeam campaigns for characterisation of bent MAPS After ensuring their proper electrical functionality by laboratory tests, the two bent ALPIDE chips were subject to an electron beam of $5.4\,\mathrm{GeV}$ at the DESY testbeam facility. There, the goal was to investigate their performance. The first of these testbeam campaigns, performed in June 2020, marked the first ever in-beam characterisation of a bent MAPS. Chapter 4 describes both testbeam setups including the bent devices under test (DUT), as well as the used trigger logic. Moreover, the experimental program, the data acquisition process and especially the tested parameter space in the sense of the set in-pixel threshold values, for both the testbeam campaigns in June and August 2020, are presented.

Data quality Looking at the two-dimensional position correlation plots, shown in section 4.6, the data quality is monitored for representative runs of both testbeam campaigns. As clear correlation lines are shown for the corresponding coordinates of different sensor planes and especially the DUT, a good data quality is verified. Already at this stage, the effect of the bent sensor surface can be seen and qualitatively evaluated. It is shown that the bending effect is stronger for the June DUT as compared to the August DUT. This is due to the different mounting of the DUTs, since in principle both of them feature comparable bending radii. The way the June DUT is mounted inside the beam telescope results in larger incident angles between the particle

tracks and the bent sensor surface normal. For the August testbeam only relatively small incident angles occur. This difference in mounting, and the resulting different range of occurring track incident angles, is the basis of the differences found in all considered analysis quantities when comparing results of both testbeam campaigns with each other.

Alignment and analysis strategy The alignment of the beam telescope planes with respect to each other and especially the subsequent alignment of the bent DUT with respect to them is of major importance for the success of the testbeam data analysis. For this work, the Corryvreckan testbeam data analysis framework is utilised to perform all these tasks. For this reason a typical data analysis process within this framework is outlined in chapter 5, especially focussing on the setup alignment. It is shown and ensured that a good alignment is achieved for both testbeam campaigns.

This work especially contributed to the implementation of bent sensor geometries within the Corryvreckan framework. As a first approach a purely cylindrical sensor surface is modelled. The radius and the bending axis can be specified in the geometry configuration file, which is read by Corryvreckan. This current implementation has three major limitations that need to be worked on in the future. For one, it only supports straight-line tracks. In the scope of this work, where only high energetic electrons are used in the testbeam campaigns, this is a good approximation. However, since Corryvreckan in principle also allows for general-broken-line tracks, it would be a helpful feature to make the implementation of the bent sensor geometry also compatible with this track model. Secondly, it is clear that the bending radius has a major impact on the bent DUT alignment. For this reason, the bending radius should be introduced to Corryvreckan as an alignment parameter. Last but not least, deviations of the physical shape of the bent DUT from a perfect cylinder section should be accounted for. This can be for example done introducing a local corrections map or a second bending radius for a different direction.

Electronic properties In order to ensure the principal functionality of the bent chips, their electronic properties are tested and compared to the case of a flat ALPIDE chip. It has been found that the differences in the in-pixel threshold are negligible in direct comparison. Also, similar fake-hit rates, which are related to the overall noise level of the sensor, are found especially for the DUT used in the June testbeam campaign. For the August DUT, an increased noise level is found and attributed to the nature of the electrical connection of the DUT to the readout system, which lacks decoupling capacitors that are usually present on the carrier card. Apart from this, both DUTs are proven to be fully functional.

Cluster sizes and shapes As a first quantity to characterise the performance of bent sensors, the cluster size is evaluated. For both DUTs, the expectation that the average cluster size decreases with increasing in-pixel thresholds is verified for clusters associated to a reference track. This trend is linked to and explained by charge sharing properties, as well as the feature of in-pixel discrimination of the induced signal. An overall increased average cluster size, as compared to the one of a flat ALPIDE chip, is found for both bent DUTs. It is discussed that this is a direct consequence of the bent sensor surface. For the nominal working point of the ALPIDE chip, the average cluster size is in between three and four pixels for both bent DUTs.

Furthermore, the charge sharing properties and thus the generation of different cluster shapes has been explored on the pixel level. For this reason pixel regions have been identified, which feature a high probability of respectively resulting in a one-, two-, three- or four pixel cluster, if the pixel is hit at these positions. This analysis is carried out by making use of dedicated

high-statistics runs in order to access sub-pixel-pitch quantities. Furthermore, the results obtained in the form of in-pixel hitmaps are linked to the later discussed in-pixel detection efficiencies. As such, macroscopic quantities like average cluster sizes and sensor detection efficiencies can be understood on a microscopic (sub-) pixel level.

Sensor and in-pixel detection efficiencies One of the most important testbeam analysis results is the detection efficiency of the bent DUTs. In general, it is found that the very high detection efficiency of the ALPIDE chip at its nominal working point is retained after bending. In fact, both bent DUTs feature a detection efficiency of even better than $99.9\,\%$ in the region of the nominal working point. An expected decrease of the efficiency for large sensor thresholds is confirmed. This trend is attributed to the charge sharing and collection properties inside a pixel.

In order to better understand this process on a pixel level, the in-pixel efficiency is investigated for a nominal and a very high threshold setting. The direct comparison of these two cases shows that for a high threshold certain regions of the pixel become inefficient. These regions are at the very edges in x-direction and are therefore linked to the charge sharing properties already explored in the cluster shape analysis. The impact of the depletion region at the collection diode is clearly visible in the case of high threshold values. Especially at this point, but also general for all the other analysis quantities, it would be enlightening to study the effect of the depletion region by applying a back-bias voltage to the bent sensors. For both testbeam campaigns such datasets exist and wait to be analysed. Furthermore, it is shown that there are no significantly inefficient regions in a representative pixel on the investigated bent sensor at the nominal operating point. In fact, an efficiency value of over $99\,\%$ is uniformly distributed over the full pixel area.

Position resolution and residuals Since the position resolution of the bent DUTs is not directly accessible by the testbeam analysis, the related width of the track residual distributions is explored in order to give at least a qualitative behaviour of this central quantity. First of all the dependency of the residual distribution width on the sensor threshold is investigated. The general trend can be explained by noise and cluster size dependencies. As such, it is shown that the position resolution in both coordinate directions, i.e. the width of the corresponding residual distributions, increases towards higher thresholds due to smaller clusters being associated to the reference tracks. Featuring a minimum roughly around the nominal working point, the increase towards lower thresholds is understood by an increased amount of noise in this regime. For very low thresholds, an unexpected decrease is indicated, which is not yet understood and needs to be further investigated.

For both testbeam datasets, a systematically deviating difference in the width of the residual distribution in x- and y-direction is noticed. Two competing parameters, namely the difference in the pixel pitch in both coordinate directions and the impact of the bent sensor surface, are identified to possibly explain this effect. In order to disentangle these two contributions, a further analysis strategy based on cluster shape information is proposed. However, also one limit of such a measurement is discussed. Selecting only one specific cluster size for the residual analysis requires a large amount of statistics in order for the results to be meaningful.

Finally, the goodness of the bent sensor surface description by a purely cylindrical model is investigated by means of correlating the residual distributions for every coordinate direction to the corresponding hit position. In the non-bent direction no correlation has been found as expected. However, for both bent DUTs there are deviations attributed to a different local sensor geometry. For the June DUT, this finding is mainly attributed to the sagging of the chip at the lower edge. In the case of the August DUT, the possibility is explored to link the found deviations to the detaching of the chip at its short edges from the cylindrical mounting jig. In order to

certainly validate these possibilities, a further dedicated analysis is required. As such, this topic is closely linked to the further development of the implementation for curved sensor geometries inside the Corryvreckan data analysis framework.

Outlook: micro-ITS3 Very recently another testbeam campaign has been performed at DESY in April 2021. The objective of this testbeam was the simultaneous in-beam characterisation of several concentrically arranged bent ALPIDE chips, thus modelling the tracking layers of the future ITS3. For this reason, this project is referred to as micro-ITS3. By the time of the testbeam unfortunately only four of the intended six layers were operational. Being bent like the DUT used in the August testbeam campaign, the target bending radii were the same ones as for the future ITS3, namely $30\,\mathrm{mm}$ for the outermost, $24\,\mathrm{mm}$ for the middle and $18\,\mathrm{mm}$ for the innermost layer. In beam direction, the first four traversed layers were the ones being operational. Thus, it was possible to successfully take data with chips bent to all three different target radii.

For future measurements the possibility of introducing a target in the centre of the detector barrel of the micro-ITS3 is explored in order to really mimic particles emerging from a particle collision.

General conclusion All presented results first of all prove the feasibility of bent MAPS, thus paving the way for a dedicated further research towards their application in future particle and nuclear physics experiments. Moreover, the performance of both differently bent ALPIDE chips are comparable to the performance of a flat chip. It indicates that the bending of the chip has no, or only a negligible, impact on the functionality of the integrated in-pixel and chip circuitry. This is a very promising result especially concerning the plans to move to a smaller technology node, namely MAPS based on the $65\,\mathrm{nm}$ CMOS imaging process. A new generation of truly cylindrical, large-scale and ultra-thin silicon pixel MAPS is about to come.

Appendices

A.1 List of abbreviations (in alphabetical order)

A

ACORDE	**A**LICE **CO**smic **R**ay **DE**tector
ADC	**A**nalog-to-**D**igital **C**onverter
AERD	**A**ddress-**E**ncoder **R**eset-**D**ecoder
ALICE	**A** **L**arge **I**on **C**ollider **E**xperiment
ALICE 3	Follow-up experiment after **A** **L**arge **I**on **C**ollider **E**xperiment
ALPIDE	**AL**ICE **PI**xel **DE**tector
ATLAS	**A** **T**oroidal **L**HC **A**pparatu**S**

C

CERN	**C**onseil **E**uropéen pour la **R**echerche **N**ucléaire (European Council for Nuclear Research)
CMM	**C**oordinate **M**easuring **M**achine
CMOS	**C**omplementary **M**etal **O**xide **S**emiconductor
CMS	**C**ompact **M**uon **S**olenoid
CFRP	**C**arbon **F**iber **R**einforced **P**lastic

D

DAC	**D**igital-to-**A**nalogue **C**onverter
DAQ	**D**ata **AQ**uisition
DESY	**D**eutsches **E**lektronen-**SY**nchrotron (German Electron Synchrotron)
DUT	**D**evice **U**nder **T**est

E

EMCal	**E**lectro**M**agnetic **Cal**orimeter
EUDAQ	**E**uropean **U**nion **D**ata **AQ**uisition

F

FIFO	**F**irst **I**n **F**irst **O**ut
FPC	**F**lex**P**rint **C**able
FPGA	**F**ield-**P**rogrammable **G**ate **A**rray
FPN	**F**ixed **P**attern **N**oise

G

GSI	**G**esellschaft für **S**chwer**I**onenforschung mbH (Helmholtz Center for Heavy Ion Research)

H

HEP	**H**igh-**E**nergy **P**hysics
HMPID	**H**igh-**M**omentum **P**article **ID**entification
HV	**H**igh **V**oltage
HVPS	**H**igh-**V**oltage **P**ower **S**upply

I

IB	**I**nner **B**arrel
IC	**I**ntegrated **C**ircuit
ID	**ID**entifiaction (number)
IP	**I**nternet **P**rotocol
IT	**I**nner **T**racker

ITS	**I**nner **T**racking **S**ystem
ITS2	Upgraded Version 2 of **I**nner **T**racking **S**ystem
ITS3	Upgraded Version 3 of **I**nner **T**racking **S**ystem

L

LGAD	**L**ow-**G**ain **A**valanche **D**etector
LHC	**L**arge **H**adron **C**ollider
LHCb	**L**arge **H**adron **C**ollider – beauty
LS2	**L**ong **S**hutdown 2
LS3	**L**ong **S**hutdown 3
LVPS	**L**ow-**V**oltage **P**ower **S**upply

M

MAPS	**M**onolithic **A**ctive **P**ixel **S**ensor
MEB	**M**ulti **E**vent **B**uffer
MIP	**M**inimum **I**onising **P**article
MOS	**M**etal **O**xide **S**emiconductor
MOSFET	**M**etal **O**xide **S**emiconductor **F**ield-**E**ffect **T**ransistor
MPV	**M**ost **P**robable **V**alue

N

NIEL	**N**on-**I**onising **E**nergy **L**oss
NIM	**N**uclear **I**nstrumentation **M**odule
NMOS	**N**-type **M**etal **O**xide **S**emiconductor

O

OB	**O**uter **B**arrel
OT	**O**uter **T**racker

P

pALPIDE	**p**rototype **ALICE** **PI**xel **DE**tector
PCB	**P**rinted **C**ircuit **B**oard
PDF	**P**robability **D**ensity **F**unction
PHOS	**PHO**ton **S**pectrometer
PID	**P**article **ID**entification
PMD	**P**hoton **M**ultiplicity **D**etector
PMOS	**P**-type **M**etal **O**xide **S**emiconductor

Q

QCD	**Q**uantum **C**hromo **D**ynamics
QFT	**Q**uantum **F**ield **T**heory
QGP	**Q**uark-**G**luon **P**lasma

R

RMS	**R**oot **M**ean **S**quare
ROI	**R**egion **O**f **I**nterest
RTN	**R**andom **T**elegraph **N**oise

S

SCF	**SC**intillator **F**ront
SCR	**SC**intillator **R**ear
SDD	**S**ilicon **D**rift **D**etector
SNR	**S**ignal to **N**oise **R**atio
SPD	**S**ilicon **P**ixel **D**etector
SPD	**S**hower **P**ixel **D**etector
SSD	**S**ilicon micro-**S**trip **D**etector

T

TB . . . . . **T**est **B**eam
TCP . . . . . **T**ransmission **C**ontrol **P**rotocol
TID . . . . . **T**otal **I**onising **D**ose
TLU . . . . . **T**rigger **L**ogic **U**nit
TOF . . . . . **T**ime **O**f **F**light
TOT . . . . . **T**ime **O**ver **T**hreshold
TPC . . . . . **T**ime **P**rojection **C**hamber
TRD . . . . . **T**ransition **R**adiation **D**etector
TTL . . . . . **T**ransistor-**T**ransistor **L**ogic

U

USB . . . . . **U**niversal **S**erial **B**us

A.2 List of figures

A.3 Additional figures

This section provides additional figures, which do not necessarily belong in the main section of this work. They are presented here for completeness and further information. Each figure is described in the corresponding caption. The figures are sorted accoding to their association to the main chapters.

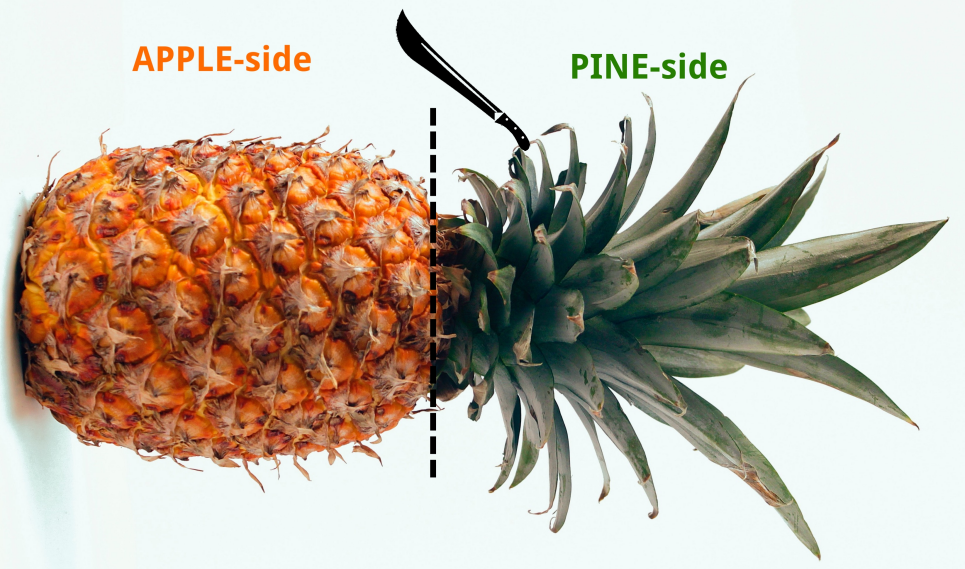

Figure A.1 Illustration of a typical pineapple junction. The juicy, edible part on the left side is commonly referred to as the APPLE-side, while the green, bushy part is denoted as the PINE-side. Joining these two parts a complete, functioning pineapple fruit is produced featuring a junction at the interface of the PINE- and the APPLE-side. In the nominal working point, the pineapple should be cut at the precise location of the junction using a machete. While the APPLE-part will usually not survive this separation process due to hungry people, the PINE-part makes quite a nice piece of decoration.

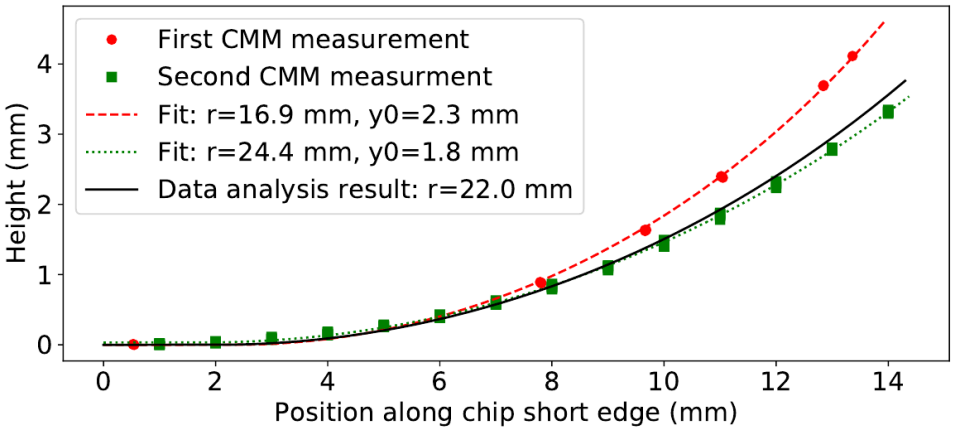

Figure A.2 Results of the coordinate measurement on the surface of the bent DUT tested in the testbeam campaign in June 2020. Two measurements where performed, one before and one after the testbeam campaign. Each set of data points in row direction of the chip is fitted with a circle plus a flat part y_0, where the chip is glued to the carrier card. The average value for all sets of points is taken as the final measured bending radius. The difference in radius before and after the beam test is attributed to a relaxation of the structure holding the bent chip in place. The result from the data analysis (black line) is compared to both measurements [46].

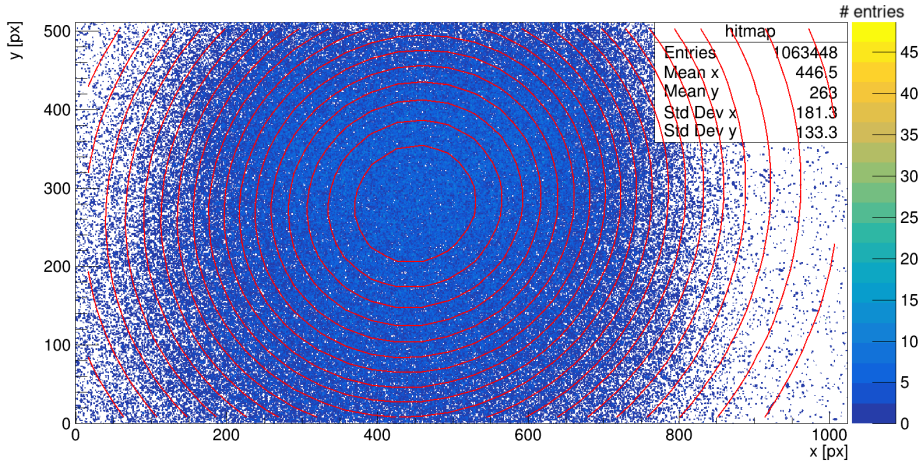

Figure A.3 Two-dimensional accumulated hitmap for the bent DUT (ALPIDE_3) used in the August testbeam campaign in order to visualise the manual detector alignment with respect to the beam. In this case the DUT is mounted in single crossing configuration meaning that each particle of the testbeam only penetrates through the sensor once. The multiplicity of a pixel hit is denoted by the colour scale. Red lines represent a two-dimensional Gaussian fit in order to highlight the centre of the beam spot.

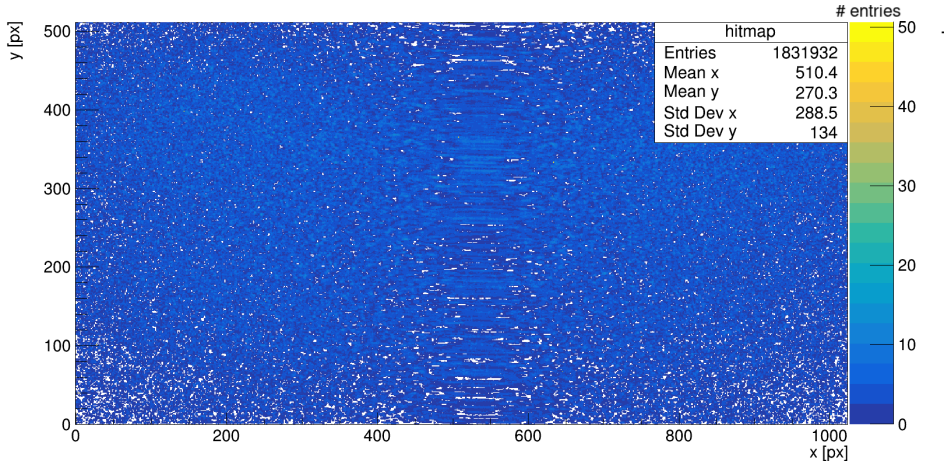

Figure A.4 Two-dimensional accumulated hitmap for the bent DUT (ALPIDE_3) used in the August testbeam campaign in order to visualise the manual detector alignment with respect to the beam. In this case the DUT is mounted in double crossing configuration meaning that a particle of the testbeam can penetrate through the sensor twice. As such the entry points of the beam particles are shown on the right side (large column numbers), while the exit points correspond to the coordinates shown on the right (low column numbers). The middle region of the chip clearly shows elongated clusters from so-called *grazing events*. Here, a beam particle traverses the bent sensor along the epitaxial layer and thus leaving a long trace of charge behind. The multiplicity of a pixel hit is denoted by the colour scale.

References

[1] N. Wermes. Trends in pixel detectors: tracking and imaging. *IEEE Transactions on Nuclear Science*, 51(3):1006–1015, 2004.

[2] R. Turchetta. CMOS Monolithic Active Pixel Sensors (MAPS) for scientific applications: Some notes about radiation hardness. *Nucl. Instrum. Meth. A*, 583:131–133, 2007.

[3] Johannes Schemmel and Andreas Hartl. Elektronik für Physiker - Vorlesungs-Skript. Sommersemester Ruprecht-Karls Universität Heidelberg, 2016.

[4] Ulrich Husemann. A New Pixel Detector fot the CMS Experiment. Particle physics colloquium, Heidelberg University. http://www-ekp.physik.uni-karlsruhe.de/~husemann/talks/husemann_cms_pixel_heidelberg_20120508.pdf. 8 May 2012, May 2012.

[5] Miljenko Suljic. *Study of Monolithic Active Pixel Sensors for the Upgrade of the ALICE Inner Tracking System.* PhD thesis, University of Trieste, November 2017. Presented 02 Feb 2018.

[6] B. Abelev et al. Technical design report for the upgrade of the ALICE inner tracking system. *Journal of Physics G: Nuclear and Particle Physics*, 41(8):087002, jul 2014.

[7] Simon M. Sze and Kwok K. Ng. *Physics of Semiconductor Devices.* John Wiley & Sons, New York, 2006.

[8] William R. Leo. *Techniques for Nuclear and Particle Physics Experiments - A How-to Approach.* Springer Science & Business Media, Berlin Heidelberg, 2012.

[9] Electronics Tutorails. The MOSFET. Officail website, 2021. Accessed 19 Mai 2021.

[10] Chao Zhao and Jinjuan Xian. Atomic Layer Deposition (ALD) of Metal Gates for CMOS. *Applied Sciences*, 9:2388, 06 2019.

[11] Bart van Zeghbroeck. *Principles of Semiconductor Devices.* http://ece-www.colorado.edu/ bart/book/, 2011. Accessed 19 Mai 2021.

[12] H. Bethe. Zur Theorie des Durchgangs schneller Korpuskularstrahlen durch Materie. *Annalen der Physik*, 397(3):325–400, 1930.

[13] B. Nilsson and A. Brahme. 9.01 - Interaction of Ionizing Radiation with Matter. In Anders Brahme, editor, *Comprehensive Biomedical Physics*, pages 1–36. Elsevier, Oxford, 2014.

[14] Silvia Masciocchi. The Physics of Particle Detectors - Interaction of particles with matter. Heidelberg University lecture notes, summer term, 2017.

[15] Particle Data Group. Experimental methods and colliders (in "Review of Particle Physics"). *Physics Letters B*, 592(1):235–274, 2004. Review of Particle Physics.

[16] W. W. M. Allison and J. H. Cobb. Relativistic Charged Particle Identification by Energy Loss. *Ann. Rev. Nucl. Part. Sci.*, 30:253–298, 1980.

[17] Hans Bichsel. Straggling in Thin Silicon Detectors. *Rev. Mod. Phys.*, 60:663–699, 1988.

[18] M. J. Berger, M. Inokuti, H. H. Anderson, H. Bichsel, J. A. Dennis, D. Powers, S. M. Seltzer, and J. E. Turner. Report 37. *Journal of the International Commission on Radiation Units and Measurements*, os19(2):NP–NP, 04 2016.

[19] Particle Data Group (PDG). Atomic and nuclear properties of silicon (Si). Official website, 2020. Accessed 12 Mai 2021.

[20] Felix Reidt. *Studies for the ALICE Inner Tracking System Upgrade.* PhD thesis, Heidelberg University, April 2016. Presented 28 Apr 2016.

[21] The ALICE ITS ALPIDE development team. ALPIDE Operations Manual. Version 0.3 (25 July 2016), July 2016.

[22] M. Deveaux. Progress on the radiation tolerance of CMOS Monolithic Active Pixel Sensors. *Journal of Instrumentation*, 14(11):R11001–R11001, nov 2019.

[23] R. K. Ellis, W. J. Stirling, and B. R. Webber. *QCD and Collider Physics.* Cambridge Monographs on Particle Physics, Nuclear Physics and Cosmology. Cambridge University Press, 1996.

[24] Ying Chen. Confinement and the Global $SU(3)$ Color Symmetry. *Chin. Phys. C*, 45(4):041001, 2021.

[25] N. Cabibbo and G. Parisi. Exponential hadronic spectrum and quark liberation. *Physics Letters B*, 59(1):67–69, 1975.

[26] John W. Harris and Berndt Müller. THE SEARCH FOR THE QUARK-GLUON PLASMA. *Annual Review of Nuclear and Particle Science*, 46(1):71–107, Dec 1996.

[27] Anton Andronic. An overview of the experimental study of quark-gluon matter in high-energy nucleus-nucleus collisions. *Int. J. Mod. Phys. A*, 29:1430047, 2014.

[28] The STAR collaboration. Studying the Phase Diagram of QCD MAtter at RHIC. Technical report, Brookhaven National Laboratory, https://drupal.star.bnl.gov/STAR/files/BES_WPII_ver6.9_Cover.pdf, June 2014.

[29] Michael Strickland. Anisotropic Hydrodynamics: Three lectures. *Acta Phys. Polon. B*, 45(12):2355–2394, 2014.

[30] Johann Rafelski and Berndt Müller. Strangeness Production in the Quark-Gluon Plasma. *Phys. Rev. Lett.*, 48:1066–1069, Apr 1982.

[31] Yuuka Kanakubo, Michito Okai, Yasuki Tachibana, and Tetsufumi Hirano. Enhancement of strange baryons in high-multiplicity proton–proton and proton–nucleus collisions. *Progress of Theoretical and Experimental Physics*, 2018(12), 12 2018. 121D01.

[32] P. Braun-Munzinger and J. Stachel. Charmonium from Statistical Hadronization of Heavy Quarks – a Probe for Deconfinement in the Quark-Gluon Plasma. *Landolt-Bornstein*, 23:424, 2010.

[33] J. D. Bjorken. Energy Loss of Energetic Partons in Quark - Gluon Plasma: Possible Extinction of High p(t) Jets in Hadron - Hadron Collisions. 8 1982.

[34] Raimond Snellings. Elliptic flow: a brief review. *New Journal of Physics*, 13(5):055008, May 2011.

[35] M. Šuljić. ALPIDE: the monolithic active pixel sensor for the ALICE ITS upgrade. *Journal of Instrumentation*, 11(11):C11025–C11025, November 2016.

[36] K. Aamodt et al. The ALICE experiment at the CERN LHC. *JINST*, 3:S08002, 2008.

[37] The ALICE Collaboration. CERN Document Server.

[38] Felix Reidt. Upgrading the Inner Tracking System and the Time Projection Chamber of ALICE. *Nucl. Phys. A*, 1005:121793, 2021.

[39] Tower Semiconductor. https://towersemi.com/. Official website of Tower semiconductor. Accessed April 2021.

[40] Luciano Musa. Letter of Intent for an ALICE ITS Upgrade in LS3. Technical report, CERN, Geneva, Dec 2019.

[41] D. Adamová et al. A next-generation LHC heavy-ion experiment. *arXiv:1902.01211 [physics.ins-det]*, May 2019.

[42] Gianluca Aglieri Rinella. Overview of the ALPIDE Pixel Sensor Chip with focus on Readout Features. FoCal Design Meeting. https://indico.cern.ch/event/666016/. 14 September 2017, September 2017.

[43] M. Mager. Alpide, the monolithic active pixel sensor for the alice its upgrade. *Nuclear Instruments and Methods in Physics Research Section A: Accelerators, Spectrometers, Detectors and Associated Equipment*, 824:434–438, 2016. Frontier Detectors for Frontier Physics: Proceedings of the 13th Pisa Meeting on Advanced Detectors.

[44] Gianluca Aglieri Rinella. The alpide pixel sensor chip for the upgrade of the alice inner tracking system. *Nuclear Instruments and Methods in Physics Research Section A: Accelerators, Spectrometers, Detectors and Associated Equipment*, 845:583–587, 2017. Proceedings of the Vienna Conference on Instrumentation 2016.

[45] R. Diener, J. Dreyling-Eschweiler, H. Ehrlichmann, I.M. Gregor, U. Kötz, U. Krämer, N. Meyners, N. Potylitsina-Kube, A. Schütz, P. Schütze, and M. Stanitzki. The DESY II test beam facility. *Nuclear Instruments and Methods in Physics Research Section A: Accelerators, Spectrometers, Detectors and Associated Equipment*, 922:265–286, 2019.

[46] ALICE ITS project: G. Aglieri Rinella, M. Agnello, B. Alessandro, J. Alme, F. Agnese, E. Anderssen, D. Andreou, F. Antinori, N. Apadula, P. Atkinson, R. Baccomi, A. Badalà, A. Balbino, C. Bartels, R. Barthel, F. Baruffaldi, I. Belikov, S. Beole, P. Becht, A. Bhatti, M. Bhopal, N. Bianchi, M. B. Blidaru, G. Boca, J. Bok, G. Bonomi, M. Bonora, M. Borri, V. Borshchov, E. Botta, G. E. Bruno, S. Bufalino, M. Cai, P. Camerini, F. Catalano, C. Ceballos Sanchez, I. Chakaberia, M. Chartier, F. Colamaria, D. Colella, A. Collu, M. Concas, G. Contin, S. Costanza, P. Cui, A. Dainese, J. B. Dainton, L. De Cilladi, C. De Martin, G. De Robertis, W. Deng, A. Di Mauro, Y. Ding, M. Durkac, D. Elia, M. R. Ersdal, M. Faggin, F. Fan, A. Fantoni, P. Fecchio, A. Feliciello, G. Feofilov, A. Ferk, J. Ferencei, G. Fiorenza, A. N. Flores,

E. Fragiacomo, D. Gajanana, A. Gal, C. Gao, C. Gargiulo, P. Gianotti, P. Giubilato, A. Grant, L. Greiner, A. Grelli, O. S. Groettvik, F. Grosa, C. Guo Hu, R. Hannigan, J. A. Hasenbichler, H. Helstrup, H. Hillemanns, C. Hills, P. Hindley, B. Hippolyte, B. Hofman, G. H. Hong, G. Huang, J. P. Iddon, H. Ilyas, A. Isakov, A. Jadlovska, S. Jadlovska, J. Jadlovsky, S. Jaelani, T. Johnson, A. Junique, P. Kalinak, A. Kalweit, M. Keil, Z. Khabanova, H. Khan, B. Kim, C. Kim, J. Kim, J. Kim, T. Kim, J. Klein, A. Kluge, C. Kobdaj, A. Kotliarov, I. Králik, F. Krizek, T. Kugathasan, C. Kuhn, P. G. Kuijer, S. Kushpil, M. J. Kweon, J. Y. Kwon, Y. Kwon, P. La Rocca, A. Lakrathok, R. Langoy, P. Larionov, E. Laudi, T. Lazareva, R. Lea, R. C. Lemmon, X. L. Li, J. Lien, B. Lim, S. H. Lim, S. Lindsay, A. Liu, J. Liu, J. Liu, M. Lunardon, G. Luparello, M. Lupi, M. Mager, A. Maire, Q. W. Malik, G. Mandaglio, V. Manzari, Y. Mao, G. V. Margagliotti, C. Markert, P. Martinengo, S. Masciocchi, M. Masera, A. Masoni, A. Mastroserio, P. F. T. Matuoka, G. Mazza, F. Mazzaschi, M. A. Mazzoni, F Morel, V. Muccifora, A. Mulliri, L. Musa, S. V. Nesbo, D. Nesterov, J. Norman, J. Park, H. Pei, X. Peng, S. Piano, C. Pinto, S. Pisano, S. Politano, E. Prakasa, F. Prino, M. Protsenko, M. Puccio, A. Rachevski, L. Ramello, F. Rami, I. Ravasenga, A. Rehman, F. Reidt, F. Riggi, K. Røed, D. Röhrich, F. Ronchetti, A. Rosano, M. J. Rossewij, A. Rossi, R. Rui, R. Russo, R. Sadikin, V. Sarritzu, J. Schambach, S. Senyukov, J. J. Seo, R. Shahoyan, S. Shaukat, S. Siddhanta, M. Sitta, R. J. M. Snellings, W. Snoeys, A. Songmoolnak, J. Sonneveld, F. Soramel, M. Suljic, R. Sultanov, S. Sumowidagdo, D. Sun, X. Sun, R. A. Syed, G. J. Tambave, S. Tang, G. Tersimonov, M. Tkacik, M. Toppi, A. Trifiró, S. Trogolo, V. Trubnikov, R. Turrisi, T. S. Tveter, I. Tymchuck, K. Ullaland, M. Urioni, G. L. Usai, N. Valle, L. V. R. van Doremalen, T. Vanat, J. W. Van Hoorne, M. Varga-Kofarago, A. Velure, D. Wang, Y. Wang, J. Wikne, J. R. Wright, R. Xu, P. Yang, Z. Yin, I. K. Yoo, J. H. Yoon, S. Yuan, V. Zaccolo, B. Zhang, E. Zhang, X. Zhang, V. Zherebchevskii, D. Zhou, J. Zhu, Y. Zhu, G. Zinovjev, and N. Zurlo. First demonstration of in-beam performance of bent Monolithic Active Pixel Sensors. https://arxiv.org/abs/2105.13000, May 2021.

[47] Markus Keil and Felix Reidt. ALPIDE Software - User manual. rev. 3 (20 June 2018), June 2018.

[48] T. Nagumo, K. Takeuchi, S. Yokogawa, K. Imai, and Y. Hayashi. New analysis methods for comprehensive understanding of Random Telegraph Noise. In *2009 IEEE International Electron Devices Meeting (IEDM)*, 2009.

[49] P. Ahlburg et al. EUDAQ-a data acquisition software framework for common beam telescopes. *JINST*, 15(01):P01038, 2020.

[50] Yi Liu. EUDAQ2 User Manual. Technical report, CERN, Geneva, Sep 2017.

[51] Y. Liu, M.S. Amjad, P. Baesso, D. Cussans, J. Dreyling-Eschweiler, R. Ete, I. Gregor, L. Huth, A. Irles, H. Jansen, K. Krueger, J. Kvasnicka, R. Peschke, E. Rossi, A. Rummler, F. Sefkow, M. Stanitzki, M. Wing, and M. Wu. EUDAQ2—a flexible data acquisition software framework for common test beams. *Journal of Instrumentation*, 14(10):P10033–P10033, oct 2019.

[52] Jens Kröger, Simon Spannagel, and Morag Williams. User Manual for the Corryvreckan Test Beam Data Reconstruction Framework, Version 1.0. *arXiv:1912.00856*, December 2019.

[53] D. Dannheim, K. Dort, L. Huth, D. Hynds, I. Kremastiotis, J. Kröger, M. Munker, F. Pitters, P. Schütze, S. Spannagel, T. Vanat, and M. Williams. Corryvreckan: a modular 4D track reconstruction and analysis software for test beam data. *Journal of Instrumentation*, 16(03):P03008, March 2021.

[54] Claus Kleinwort. General broken lines as advanced track fitting method. *Nuclear Instruments and Methods in Physics Research Section A: Accelerators, Spectrometers, Detectors and Associated Equipment*, 673:107–110, May 2012.

[55] ROOT development team. TEfficiency Class Reference. Official website, ROOT class references, 2020. Accessed 27 Mai 2021.

Acknowledgement

During the course of this Master project there have been the usual ups and downs, but also very special and extraordinary moments that will never be forgotten. Not only have I gained a lot of usable knowledge during this time, but also I have grown as a person. It has to be noted that his is not my personal achievement, but is due to all the wonderful people surrounding me: family, friends and colleagues. Already at this point I would like to say *THANK YOU* to all the people supporting me in every possible and impossible way. You are the reason why I can be the person I want to be on a daily basis. I apologise for not being able to mention all of you by name, but be assured you are equally acknowledged.

Having said this, I would like to especially thank Silvia Masciocchi for giving me the opportunity to study cut of the edge technology within the frame of the ALICE groups at GSI and Heidelberg University. Always having an open ear for all of her students, despite her seemingly 25-hour schedule per day, makes her invaluable as a supervisor and colleague. Also her personal interest in the project and the almost unconditional support in all thinkable aspects enriches the many discussions with new ideas and makes all of my research possible at all. Furthermore, I would like to express my gratitude to Prof. Dr. Norbert Herrmann for immediately agreeing to be the second examiner of this work.

To the entire ITS team, but especially to Magnus Mager, Miljenko Suljic, Felix Reidt, Giacomo Contin and Alexander Ferk, I would also like to say a big thank you. Without your help and your support none of the presented results would have been possible. Particularly, entrusting me and my colleague Bogdan with executing the first and second testbeam featuring the bent DUTs on our own with only the possibility of remote help due to the omnipresent Covid-19 restrictions during this time was a big step. This experience was priceless in all aspects and is well appreciated.

In this and many more facets, I owe my colleague Bogdan Blidaru a big dept of gratitude. He is the second part of the hardware nucleus in our research group and is always prepared to to defend it against clumsy analysis people. Joking aside, he is a very reliable person and a great discussion partner. Being thrown in the cold water of silicon detectors we figured out a lot of stuff together and more is coming on a daily basis. Especially, for proofreading I am endlessly grateful and hope I can return the favour for his PhD thesis. I am also extremely thankful for all the other colleagues making our research group such a warm and welcoming place, even though we mostly had to interact via our computer screens. I really enjoy the initiative and liveliness of all those people.

Looking around GSI, there especially is one person without whom probably none of the presented testbeam campaigns would have been possible. Thank you Oleg for always lending us equipment and offering your helping hand, not only concerning testbeam related, but also more general topics. Regarding the recently formed interest group, I am looking forward to a strong MAPS knowledge cluster at GSI.

Basically all my friends, which are like a second extremely large and diverse family to me, helped me with this work in all different kind of ways. Sometimes it is just listening to me blabbering about my problems with the analysis code, while another time it is training with me to clear away the cobwebs. If it is providing me a scanner, or simply having a beer with me, every

of these gestures are very valuable to me. Occasionally, all it takes is a nice cooking session and night shift afterwards to get me going. No matter if it has to be an hour long phone call or a spontaneous visit, every kind of interaction with you all makes my live better. Some people know that a home-made cookie can change the world, while for others it is a dram. Running out of different phrases to make all of this sound interesting, here are just some of the persons that most probably can relate to what I have just written: Clemens, Tim, Laila, Kenny, Larissa, Alissa, Denise, Paddy, Annika, Maggie and many more ...

I am especially grateful for my flatmates Ash and Sarah for enduring me in my best and worst times. It is a great support living with people whom I can rely on. Sometimes, a short chat in the kitchen saves my day.

Ond wia's halt so isch: 's Lädschde als lädschdes. O'gfanga hots mit "Dr Bua isch ausm Haus". Weit gschafft han I 's abr net. Isch ja zom Glick bloß Heidelberg worda. Stindle noh Stindle z'rig so hot mr mir oinige Sächle nachtraga. Wenn dr Kopf net o'gwagsa wär ... Isch er abr! Grad nommol Schwein kett, sonscht wär ja des ganze Pauka ond Maloche umsonscht gwä. Oms Rumgugge (naja, net so ganz) hab I nämlich mei lässigs Schdudendaleba mit derra Arbeit hidr mir g'lassa. Mol gugge ob I uff eigene Fiaß steha koh odr ob I mi liebr nommol noleg. Oins isch sicher: egal wia's kommt, I komm emmr wiedr gern hoim. I woiß net wia I mi fir des elles bedange soll, abr I versuchs im schwäbischen Sinne: Dange halt emmol! Griaßle an de Reschd der Bagasch.

Declaration

I declare that this thesis has been composed solely by myself and that it has not been submitted, in whole or in part, in any previous application for a degree. Except where states otherwise by reference or acknowledgment, the work presented is entirely my own.

Erklärung

Ich versichere, dass ich diese Arbeit selbstständig verfasst und keine anderen als die angegebenen Quellen und Hilfsmittel benutzt habe.

Heidelberg, May 31, 2021

Pascal Becht